



Theses and Dissertations

2010-03-10

Particle Image Velocimetry Analysis on the Effects of Stator Loading on Transonic Blade-Row Interactions

Scott B. Reynolds
Brigham Young University - Provo

Follow this and additional works at: <https://scholarsarchive.byu.edu/etd>



Part of the [Mechanical Engineering Commons](#)

BYU ScholarsArchive Citation

Reynolds, Scott B., "Particle Image Velocimetry Analysis on the Effects of Stator Loading on Transonic Blade-Row Interactions" (2010). *Theses and Dissertations*. 2087.

<https://scholarsarchive.byu.edu/etd/2087>

This Thesis is brought to you for free and open access by BYU ScholarsArchive. It has been accepted for inclusion in Theses and Dissertations by an authorized administrator of BYU ScholarsArchive. For more information, please contact scholarsarchive@byu.edu, ellen_amatangelo@byu.edu.

Particle Image Velocimetry Analysis on the Effect of Stator Loading on
Transonic Blade-Row Interactions

Scott B. Reynolds

A thesis submitted to the faculty of
Brigham Young University
in partial fulfillment of the requirements for the degree of
Master of Science

Steven E. Gorrell, Chair
Scott L. Thomson
Julie Vanderhoff

Department of Mechanical Engineering
Brigham Young University
April 2010

Copyright © 2010 Scott B. Reynolds
All Rights Reserved

ABSTRACT

Particle Image Velocimetry Analysis on the Effect of Stator Loading on Transonic Blade-Row Interactions

Scott B. Reynolds

Department of Mechanical Engineering

Master of Science

Experiments have been performed using the Air Force Research Laboratory (AFRL) Blade-Row Interaction (BRI) rig to investigate interactions between a loaded stator and transonic rotor. The BRI rig is a high-speed, highly loaded compressor consisting of a swirler/deswirler, a transonic rotor and a stator. The swirler/deswirler of the BRI rig is used to simulate an embedded transonic fan stage with realistic geometry which produces a wake through diffusion. Details of the unsteady flow field between the stator and rotor were obtained using Particle Image Velocimetry (PIV). Flow visualization images and PIV data that facilitate analysis of vortex shedding, wake motion, and wake-shock-interactions in the blade row are analyzed for three stator/rotor axial spacings and two stator loadings. The data analysis focuses on measuring and comparing, for the different spacings and loading, the vortex size, strength, and location as it forms on the stator trailing edge and propagates downstream into the rotor passage. It was observed that more than one vortex was shed with the passing of a rotor bow shock. These vortices were categorized as small and large vortices with a $\sim 20\%$ decrease in strength. The large vortices were compared at similar location and results show that vortex strength increased as spacing between stator and rotor decreased due to the increased strength of the rotor bow shock impacting the stator trailing edge. Changes in stator loading also affected shed vortex strength. A decrease in stator loading resulted in a decrease in the strength of the vortex shed. The smaller vortices were not affected by a change in spacing but strength was directly related to the loading.

Keywords: blade row interactions, particle image velocimetry, stator loading, vortex shedding

ACKNOWLEDGMENTS

The author would like to thank his thesis advisor, Dr. Steve Gorrell, for his encouragement, guidance and support. The author would also like to thank committee members, Dr. Scott Thomson and Dr. Julie Vanderhoff, for their input and aid. The author acknowledges the technical assistance of the CARL group at Wright-Patterson AFB and ISSI personnel during the experiments. A special thanks goes out to the Air Force Research Laboratory for providing the experimental data and allowing the work to be published. A debt of gratitude is owed to the author's wife, Leah, for the sacrifices she has made and support given over the years.

TABLE OF CONTENTS

| | |
|---|-------------|
| LIST OF TABLES | vi |
| LIST OF FIGURES | viii |
| NOMENCLATURE | xii |
| Chapter 1 Introduction | 1 |
| 1.1 Motivation | 1 |
| 1.2 Experimental Compressors | 2 |
| 1.3 Objective | 4 |
| Chapter 2 Literature Review and Background | 7 |
| 2.1 Stage Matching Investigation Rig | 9 |
| 2.2 Blade Row Interaction Rig | 15 |
| Chapter 3 Particle Image Velocimetry | 27 |
| 3.1 PIV Setup | 28 |
| 3.2 Cross-Correlation and Vector Calculation | 29 |
| Chapter 4 Results | 39 |
| 4.1 Qualitative Observations | 39 |
| 4.1.1 Far Spacing | 45 |
| 4.1.2 Mid and Close Spacing. | 49 |
| 4.2 Vortex Characteristics | 53 |
| 4.2.1 Vortex Radius | 53 |
| 4.2.2 Vortex Strength | 56 |
| 4.3 Design Implications | 63 |
| Chapter 5 Conclusion | 65 |
| REFERENCES | 69 |
| Appendix A Running PPIV on Marylou4 | 73 |
| A.1 Introduction | 73 |
| A.1.1 PIV | 73 |
| A.1.2 PPIV | 73 |
| A.1.3 Marylou4 | 74 |
| A.2 BYU's Supercomputer Marylou4 | 74 |
| A.2.1 Accessing Marylou4 | 74 |
| A.2.2 Secure Shell Client | 75 |
| A.2.3 Learning and Using Linux | 76 |
| A.2.4 Submitting a Job | 78 |

| | | |
|---|--|------------|
| A.3 | Shell Script | 79 |
| A.4 | Parallel PIV Setup | 81 |
| | A.4.1 Parameters | 81 |
| | A.4.2 Images | 81 |
| A.5 | Transferring Files | 85 |
| A.6 | Running PPIV Executable | 86 |
| Appendix B Flow Visualization Images | | 89 |
| B.1 | Close Spacing, Nominal Loading | 89 |
| B.2 | Mid Spacing, Nominal Loading | 92 |
| B.3 | Mid Spacing, Decreased Loading | 96 |
| B.4 | Far Spacing, Nominal Loading | 99 |
| B.5 | Far Spacing, Decreased Loading | 102 |
| Appendix C Speed Contours | | 107 |
| C.1 | Close Spacing, Nominal Loading | 107 |
| C.2 | Mid Spacing, Nominal Loading | 110 |
| C.3 | Mid Spacing, Decreased Loading | 114 |
| C.4 | Far Spacing, Nominal Loading | 117 |
| C.5 | Far Spacing, Decreased Loading | 121 |
| Appendix D Vorticity Contours | | 125 |
| D.1 | Close Spacing, Nominal Loading | 125 |
| D.2 | Mid Spacing, Nominal Loading | 128 |
| D.3 | Mid Spacing, Decreased Loading | 132 |
| D.4 | Far Spacing, Nominal Loading | 135 |
| D.5 | Far Spacing, Decreased Loading | 139 |

LIST OF TABLES

| | | |
|-----|--|----|
| 2.1 | Wake generator axial spacing (normalized by local wake generator chord) | 9 |
| 2.2 | SMI aerodynamic design parameters (from Gorrell et al. [1]) | 10 |
| 2.3 | BRI aerodynamic design parameters | 20 |
| 4.1 | Radius of vortices located 20% chord length downstream of deswirler | 56 |
| 4.2 | Circulation of vortices located 20% chord length downstream of deswirler trailing edge | 59 |

LIST OF FIGURES

| | | |
|------|---|----|
| 1.1 | Jet engine with axial compressor showing stator and rotor blade rows. | 1 |
| 1.2 | Flow field in SMI rig showing trailing edge of wake generator, unsteady flow, and rotor bow shock. | 3 |
| | | |
| 2.1 | Cross-sectional view of the SMI compressor rig (from Gorrell, et al. [1] | 10 |
| 2.2 | SMI performance (from Gorrell, et al. [2]) | 12 |
| 2.3 | Entropy flux contours at close spacing (from Gorrell, et al. [3]). | 13 |
| 2.4 | Entropy flux contours at far spacing (from Gorrell, et al. [3]). | 14 |
| 2.5 | Vortex size comparison for Close and Far spacing (from Gorrell, et al. [3]). | 15 |
| 2.6 | Shock turning normal to wake generator at close spacing (from Gorrell, et al. [4]). | 16 |
| 2.7 | Blade-row-interaction (BRI) rig cross section in its general configuration. | 17 |
| 2.8 | Swirler and Deswirler shapes at 50% span. | 18 |
| 2.9 | Photograph of vane of interest in BRI rig. | 19 |
| 2.10 | BRI performance at nominal loading. | 21 |
| 2.11 | BRI performance at decreased loading. | 22 |
| 2.12 | Instantaneous streamlines for steady flow and three different shock strengths, with corresponding effective blockage (from Langford, et al. [5]). | 24 |
| | | |
| 3.1 | Projected laser sheet with squared region of study. | 28 |
| 3.2 | Cross correlation over two windows at same location. | 30 |
| 3.3 | Calculations performed in cross correlation. | 31 |
| 3.4 | Original correlation map, sub-map and centroid area. | 32 |
| 3.5 | Particle has moved outside of reduced interrogation window. | 33 |
| 3.6 | Window has been shifted based on results from previous pass. | 34 |
| 3.7 | Flow visualization of seven blade delay for mid spacing at nominal loading. | 38 |
| | | |
| 4.1 | Deswirler wake flow visualization for far spacing, decreased loading, BLDL0. | 41 |
| 4.2 | Average velocity vectors obtained from PIV for far spacing, decreased loading and BLDL0 with average speed contour showing decreased velocity of the wake and abrupt change of velocity and direction across the shock. | 42 |
| 4.3 | Streamlines of average velocity field of Fig. 4.1; Top image: no convective velocity subtracted, Middle image: near-field convective velocity subtracted, Bottom image: far-field convective velocity subtracted. | 43 |
| 4.4 | Close up of streamlines used to show the saddle between two vortices when convective velocity has been subtracted. | 44 |
| 4.5 | Vorticity contours of average velocity field of Fig. 4.1. | 45 |
| 4.6 | Far spacing, 50% span, at nominal loading. Median velocity with vorticity contours for one blade period (0, 20, 40, 60, 80, 100, 120 μ sec blade delay from top to bottom). | 47 |
| 4.7 | Far spacing, 50% span, at decreased loading. Median velocity with vorticity contours for one blade period (0, 20, 40, 60, 80, 100, 120 μ sec blade delay from top to bottom). | 48 |

| | | |
|------|--|----|
| 4.8 | Mid spacing, 50% span, nominal loading. Median velocity with vorticity contours for one blade period (0, 20, 40, 60, 80, 100, 120 μ sec blade delay from top to bottom). | 50 |
| 4.9 | Mid spacing, 50% span, decreased loading. Median velocity with vorticity contours for one blade period (0, 20, 40, 60, 80, 100, 120 μ sec blade delay from top to bottom). | 51 |
| 4.10 | Close spacing, 50% span, nominal loading. Median velocity with vorticity contours for one blade period (0, 40, 60, 80, 100, 120 μ sec blade delay from top to bottom). | 52 |
| 4.11 | Grid used to find vortex radius | 54 |
| 4.12 | Image showing chordwise (parallel to flow) and pitchwise (perpendicular to flow) radius. | 55 |
| 4.13 | Integration paths for calculation of circulation. | 57 |
| 4.14 | Tangential velocity of a Rankine Vortex. | 59 |
| 4.15 | Vortices at 20% meridional chord length for close, mid, and far spacings at nominal loading. | 61 |
| 4.16 | Vortices at 20% meridional chord length for mid, and far spacings (top to bottom) at decreased loading. | 62 |
| 4.17 | Circulation of weaker vortices at mid and far spacings (top and bottom) for nominal and decreased loadings. | 63 |
| A.1 | Marylou4's command prompt | 76 |
| A.2 | Description of Parameters file for running PPIV. | 82 |
| A.3 | Description of Image list file for running PPIV. | 83 |
| A.4 | PSFTP command prompt with commands on how to transfer files. | 86 |
| B.1 | Close spacing, Nominal loading, Blade Delay 0 | 89 |
| B.2 | Close spacing, Nominal loading, Blade Delay 40 | 90 |
| B.3 | Close spacing, Nominal loading, Blade Delay 60 | 90 |
| B.4 | Close spacing, Nominal loading, Blade Delay 80 | 91 |
| B.5 | Close spacing, Nominal loading, Blade Delay 100 | 91 |
| B.6 | Close spacing, Nominal loading, Blade Delay 120 | 92 |
| B.7 | Mid spacing, Nominal loading, Blade Delay 0 | 92 |
| B.8 | Mid spacing, Nominal loading, Blade Delay 20 | 93 |
| B.9 | Mid spacing, Nominal loading, Blade Delay 40 | 93 |
| B.10 | Mid spacing, Nominal loading, Blade Delay 60 | 94 |
| B.11 | Mid spacing, Nominal loading, Blade Delay 80 | 94 |
| B.12 | Mid spacing, Nominal loading, Blade Delay 100 | 95 |
| B.13 | Mid spacing, Nominal loading, Blade Delay 120 | 95 |
| B.14 | Mid spacing, Decreased loading, Blade Delay 0 | 96 |
| B.15 | Mid spacing, Decreased loading, Blade Delay 20 | 96 |
| B.16 | Mid spacing, Decreased loading, Blade Delay 40 | 97 |
| B.17 | Mid spacing, Decreased loading, Blade Delay 60 | 97 |
| B.18 | Mid spacing, Decreased loading, Blade Delay 80 | 98 |
| B.19 | Mid spacing, Decreased loading, Blade Delay 100 | 98 |

| | | |
|------|---|-----|
| B.20 | Mid spacing, Decreased loading, Blade Delay 120 | 99 |
| B.21 | Far spacing, Nominal loading, Blade Delay 20 | 99 |
| B.22 | Far spacing, Nominal loading, Blade Delay 40 | 100 |
| B.23 | Far spacing, Nominal loading, Blade Delay 60 | 100 |
| B.24 | Far spacing, Nominal loading, Blade Delay 80 | 101 |
| B.25 | Far spacing, Nominal loading, Blade Delay 100 | 101 |
| B.26 | Far spacing, Nominal loading, Blade Delay 120 | 102 |
| B.27 | Far spacing, Decreased loading, Blade Delay 0 | 102 |
| B.28 | Far spacing, Decreased loading, Blade Delay 20 | 103 |
| B.29 | Far spacing, Decreased loading, Blade Delay 40 | 103 |
| B.30 | Far spacing, Decreased loading, Blade Delay 60 | 104 |
| B.31 | Far spacing, Decreased loading, Blade Delay 80 | 104 |
| B.32 | Far spacing, Decreased loading, Blade Delay 100 | 105 |
| B.33 | Far spacing, Decreased loading, Blade Delay 120 | 105 |
| | | |
| C.1 | Close spacing, Nominal loading, Blade Delay 0 | 107 |
| C.2 | Close spacing, Nominal loading, Blade Delay 20 | 108 |
| C.3 | Close spacing, Nominal loading, Blade Delay 60 | 108 |
| C.4 | Close spacing, Nominal loading, Blade Delay 80 | 109 |
| C.5 | Close spacing, Nominal loading, Blade Delay 100 | 109 |
| C.6 | Close spacing, Nominal loading, Blade Delay 120 | 110 |
| C.7 | Mid spacing, Nominal loading, Blade Delay 0 | 110 |
| C.8 | Mid spacing, Nominal loading, Blade Delay 20 | 111 |
| C.9 | Mid spacing, Nominal loading, Blade Delay 40 | 111 |
| C.10 | Mid spacing, Nominal loading, Blade Delay 60 | 112 |
| C.11 | Mid spacing, Nominal loading, Blade Delay 80 | 112 |
| C.12 | Mid spacing, Nominal loading, Blade Delay 100 | 113 |
| C.13 | Mid spacing, Nominal loading, Blade Delay 120 | 113 |
| C.14 | Mid spacing, Decreased loading, Blade Delay 0 | 114 |
| C.15 | Mid spacing, Decreased loading, Blade Delay 20 | 114 |
| C.16 | Mid spacing, Decreased loading, Blade Delay 40 | 115 |
| C.17 | Mid spacing, Decreased loading, Blade Delay 60 | 115 |
| C.18 | Mid spacing, Decreased loading, Blade Delay 80 | 116 |
| C.19 | Mid spacing, Decreased loading, Blade Delay 100 | 116 |
| C.20 | Mid spacing, Decreased loading, Blade Delay 120 | 117 |
| C.21 | Far spacing, Nominal loading, Blade Delay 0 | 117 |
| C.22 | Far spacing, Nominal loading, Blade Delay 20 | 118 |
| C.23 | Far spacing, Nominal loading, Blade Delay 40 | 118 |
| C.24 | Far spacing, Nominal loading, Blade Delay 60 | 119 |
| C.25 | Far spacing, Nominal loading, Blade Delay 80 | 119 |
| C.26 | Far spacing, Nominal loading, Blade Delay 100 | 120 |
| C.27 | Far spacing, Nominal loading, Blade Delay 120 | 120 |
| C.28 | Far spacing, Decreased loading, Blade Delay 0 | 121 |
| C.29 | Far spacing, Decreased loading, Blade Delay 20 | 121 |
| C.30 | Far spacing, Decreased loading, Blade Delay 40 | 122 |

| | | |
|------|---|-----|
| C.31 | Far spacing, Decreased loading, Blade Delay 60 | 122 |
| C.32 | Far spacing, Decreased loading, Blade Delay 80 | 123 |
| C.33 | Far spacing, Decreased loading, Blade Delay 100 | 123 |
| C.34 | Far spacing, Decreased loading, Blade Delay 120 | 124 |
| | | |
| D.1 | Close spacing, Nominal loading, Blade Delay 0 | 125 |
| D.2 | Close spacing, Nominal loading, Blade Delay 40 | 126 |
| D.3 | Close spacing, Nominal loading, Blade Delay 60 | 126 |
| D.4 | Close spacing, Nominal loading, Blade Delay 80 | 127 |
| D.5 | Close spacing, Nominal loading, Blade Delay 100 | 127 |
| D.6 | Close spacing, Nominal loading, Blade Delay 120 | 128 |
| D.7 | Mid spacing, Nominal loading, Blade Delay 0 | 128 |
| D.8 | Mid spacing, Nominal loading, Blade Delay 20 | 129 |
| D.9 | Mid spacing, Nominal loading, Blade Delay 40 | 129 |
| D.10 | Mid spacing, Nominal loading, Blade Delay 60 | 130 |
| D.11 | Mid spacing, Nominal loading, Blade Delay 80 | 130 |
| D.12 | Mid spacing, Nominal loading, Blade Delay 100 | 131 |
| D.13 | Mid spacing, Nominal loading, Blade Delay 120 | 131 |
| D.14 | Mid spacing, Decreased loading, Blade Delay 0 | 132 |
| D.15 | Mid spacing, Decreased loading, Blade Delay 20 | 132 |
| D.16 | Mid spacing, Decreased loading, Blade Delay 40 | 133 |
| D.17 | Mid spacing, Decreased loading, Blade Delay 60 | 133 |
| D.18 | Mid spacing, Decreased loading, Blade Delay 80 | 134 |
| D.19 | Mid spacing, Decreased loading, Blade Delay 100 | 134 |
| D.20 | Mid spacing, Decreased loading, Blade Delay 120 | 135 |
| D.21 | Far spacing, Nominal loading, Blade Delay 0 | 135 |
| D.22 | Far spacing, Nominal loading, Blade Delay 20 | 136 |
| D.23 | Far spacing, Nominal loading, Blade Delay 40 | 136 |
| D.24 | Far spacing, Nominal loading, Blade Delay 60 | 137 |
| D.25 | Far spacing, Nominal loading, Blade Delay 80 | 137 |
| D.26 | Far spacing, Nominal loading, Blade Delay 100 | 138 |
| D.27 | Far spacing, Nominal loading, Blade Delay 120 | 138 |
| D.28 | Far spacing, Decreased loading, Blade Delay 0 | 139 |
| D.29 | Far spacing, Decreased loading, Blade Delay 20 | 139 |
| D.30 | Far spacing, Decreased loading, Blade Delay 40 | 140 |
| D.31 | Far spacing, Decreased loading, Blade Delay 60 | 140 |
| D.32 | Far spacing, Decreased loading, Blade Delay 80 | 141 |
| D.33 | Far spacing, Decreased loading, Blade Delay 100 | 141 |
| D.34 | Far spacing, Decreased loading, Blade Delay 120 | 142 |

NOMENCLATURE

| | |
|-----------------|---------------------------------------|
| AFRL | Air Force Research Laboratory |
| SMI | Stage Matching Investigation |
| WG | Wake Generator |
| BRI | Blade Row Interaction |
| TE | Trailing Edge |
| PIV | Particle Image Velocimetry |
| c | Wake generator chord |
| M_{rel} | Relative mach number |
| $\bar{\omega}$ | Loss coefficient |
| P_{rake} | Total pressure measured by rakes |
| P_{inlet} | Total pressure at inlet |
| p_{inlet} | Static pressure at inlet |
| X | Horizontal direction in PIV window |
| Y | Vertical direction in PIV window |
| C_{ij} | Pixel value at index (i,j) |
| Bg | Average pixel value of background |
| U | Horizontal velocity vector |
| V | Vertical velocity vector |
| N | Number of rows or columns in a cell |
| ω_z, w_z | Vorticity |
| Γ | Circulation |
| \mathbf{n} | Normal vector |
| U_θ | Tangential velocity of rankine vortex |
| \mathbf{u} | Tangential velocity |
| r | Radius |
| r_c | Radius of rankine vortex core |
| Ω | Rankine vortex constant |

CHAPTER 1. INTRODUCTION

1.1 Motivation

The axial compressor is one of the most common turbomachines in use today. The compressor is made up of two major assemblies: the rotating rotor blades and the stationary stator blades (see Fig. 1.1). Each set of rotor and stator blades make up a stage. Each stage of an axial compressor produces an increase in pressure. Multiple stages are used in order to obtain higher overall pressure ratios. Designers are tasked with the design of progressively more efficient turbomachinery components with reduced weight and size. Increases in pressure ratio per stage allow for higher overall pressure ratios using less stages resulting in smaller and lighter engines with fewer parts. Higher stage pressure ratio has been achieved by including highly loaded stages with a transonic rotor. With a relative velocity above Mach one, a rotor bow shock forms on the leading edge of the rotor. As the flow crosses the shock, the static pressure is increased allowing

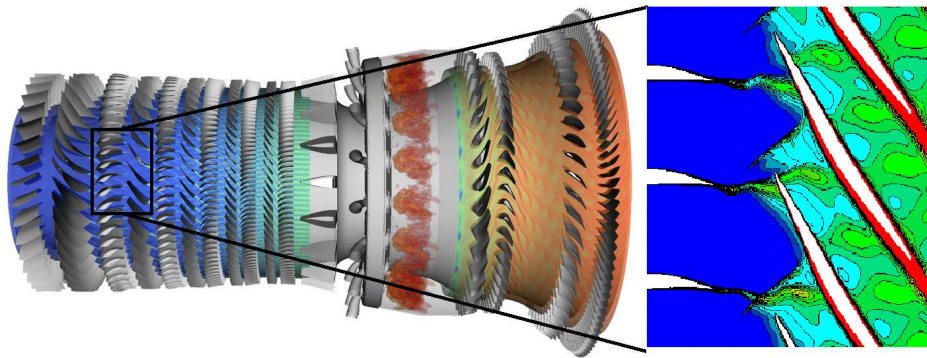


Figure 1.1: Jet engine with axial compressor showing stator and rotor blade rows.

for higher pressure ratios. Another method of decreasing size and weight of turbomachinery is by reducing the spacing between the stator and rotor blades. These changes, while reducing the size and weight of the engine, have resulted in unsteady flow characteristics not included in the design of the compressor using traditional steady tools.

Closely spaced and highly loaded blade rows are a significant source of unsteady flow in advanced high-performance turbomachines. Blade-row interactions such as the interaction of a shock with a shed vortex and a shock with a surface of a stator blade produce time-dependent non-uniformities and irregular flow patterns that influence compressor performance and blade vibrations. Understanding unsteady flows and their affect on compressor performance will aid in the development of more efficient and reliable turbomachines. The Air Force Research Laboratory (AFRL) Compressor Aero Research Lab (CARL) has been investigating transonic compressor blade-row interaction through experimental and computational research for several years. A better understanding of unsteady phenomena is needed to identify the impact of unsteady aerodynamics on compressor performance, to develop and validate tools for measuring and modeling unsteady flows, and to develop design tools that more accurately account for unsteady aerodynamics.

1.2 Experimental Compressors

Recent research on unsteady flows in highly loaded transonic fans and compressors [1–11] has shown that both high-fidelity experiments and simulations are essential for understanding the physics of blade-row interactions. The AFRL CARL Stage Matching Investigation (SMI) rig was the first experimental compressor used to investigate transonic blade-row interactions. The test rig used a wake generator to simulate loss generated by an upstream stage to more clearly observe how rotor-bow shocks could affect upstream flow (see Fig. 1.2). Gorrell et al. [2] found using the

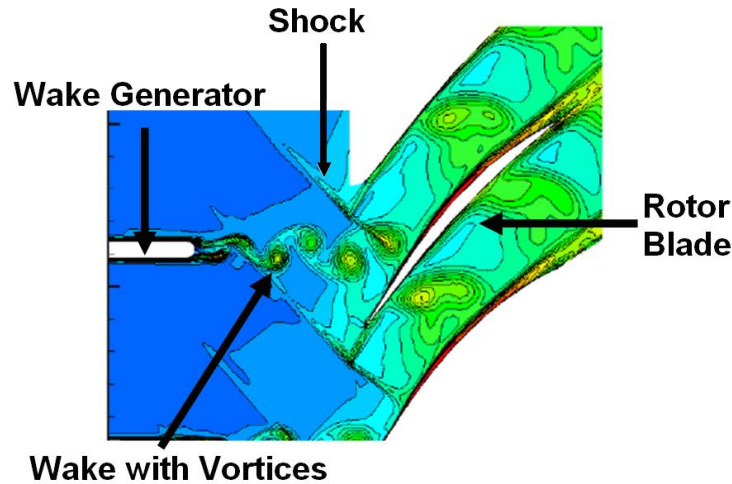


Figure 1.2: Flow field in SMI rig showing trailing edge of wake generator, unsteady flow, and rotor bow shock.

SMI rig that axial spacing between upstream stators and downstream transonic rotors significantly affects stage performance. A decrease in mass flow rate, pressure ratio, and efficiency were found when the spacing between a wake generator and rotor was decreased. As the axial spacing between rotor and wake generator decreased from the maximum spacing (55% chord downstream) to the minimum spacing (13% chord downstream), a 0.9% decrease in mass flow rate, 3.3% decrease in pressure ratio, and a 1.3 point loss in efficiency were observed. Performance reduction was attributed to additional loss production that occurred as a result of the interaction between the upstream wake generator and the downstream transonic rotor. Time-accurate CFD simulations were also used to investigate unsteady characteristics in the SMI rig. SMI setup and findings along with CFD results will be presented in chapter two.

In order to build on the knowledge learned from the SMI program the next step was to use realistic stator designs to investigate interactions between a transonic rotor and smaller vortices shed from thinner stator trailing edges. The Blade Row Interaction (BRI) rig followed the SMI

program by replacing the blunt wake generator with a realistic stator. The objective of the new hardware was to simulate an embedded transonic fan stage that produced a wake through diffusion with realistic geometry (thin trailing edge) rather than base drag (wake generator). The BRI rig was designed to not only vary the stator-to-rotor axial spacing but also the stator loading, or measure of the pressure difference between the two sides of the stator blade. Particle Image Velocimetry (PIV) was used to obtain flow visualization images and velocity vectors allowing for a quantitative and qualitative study of blade-row interactions. The focus of the BRI experiments was to observe the effect of loading, operating condition, and axial spacing on blade-row interactions. A more detailed explanation of the BRI rig is discussed in chapter two.

1.3 Objective

Blade-row interactions are the source of many unsteady flow characteristics in transonic compressors. These unsteady flow characteristics have yet to be specifically accounted for in the design of highly loaded transonic compressors. A more complete understanding of blade-row interactions and the unsteady flow produced by these interactions would allow designers to account for unsteady flow when designing highly loaded stators and predicting off-design performance of even nominally loaded stators. The objective of this research is to quantify for the first time the unsteady flow characteristics, specifically changes in vortex shedding in response to changes in loading, using PIV measurements. PIV data was used to analyze vortex size, strength, and location at three rotor/stator spacings and two loadings. A literature review containing a historical background, description of transonic compressors, and recent and related work will be discussed. A detailed description of the SMI and BRI rig and previous experimental and computational results will be presented. The PIV system, algorithms and data filtering will be addressed. Methods used

in evaluating vortex shedding and strength will be discussed along with qualitative and quantitative comparison between settings and loadings and their significance.

CHAPTER 2. LITERATURE REVIEW AND BACKGROUND

An understanding of the unsteady flow through a turbomachine is necessary in order to comprehend and overcome technical challenges encountered during the design and operation of high performance gas turbine engines. Unsteady flow phenomena are known to play a primary role in turbine engine operating limits. An area of interest for the last decade has been to evaluate the impact of unsteady flows on turbomachine performance. A better understanding of unsteady fluid dynamics can be incorporated into the design of turbomachine components.

Adamczyk [12] described the need for experimental and numerical work which focused on unsteady fluid mechanics and the impact on axial turbomachinery performance. Experimental results increase understanding of these unsteady flows and can also be used to verify results obtained from design tools. Adamczyk described a need for multi-stage design tools that do not rely on empirical formulations or data as inputs. He showed that in order to develop design tools that account for unsteady characteristics, a more complete understanding of unsteady flows that are classified as nondeterministic but are not turbulent in nature must be obtained. An example of these unsteady flow characteristics is the shedding of vortices from a blade's trailing edge.

Vortex shedding in turbomachines has been the focus of research for some time. Hathaway et al. [13] observed vortex shedding in fan rotors, which were shown to lead to spanwise redistribution of entropy by Kotidis and Epstein [14]. It has also been observed that the stretching of vortices lead to flow instabilities which resulted in rapid mixing [15]. These unsteady nonturbulent flows

appear to lead to the mixing of shear layers and therefore generate loss which reduces pressure rise and efficiency.

The magnitude of the impact of such mixing processes on aerodynamic performance of multistage axial flow turbomachines is still under investigation. Initial research was accomplished using low-speed compressor rigs. Results from experimental multistage subsonic compressors were presented by Smith [16] and Mikolajczak [17]. Experimental results showed that reducing the axial gap between blade rows increased the pressure ratio and isentropic efficiency. Recently, high-speed axial compressor research has been initiated. Experimental blade-row interactions studies in transonic compressors have focused on visualizing and quantifying the interaction mechanisms present in the flow field. Ottavy et al. [18] performed measurements and analysis on the interaction between the rotor bow shock and the wake shed from an Inlet Guide Vane (IGV). The experiment used laser two-focus anemometer measurements between an IGV and transonic rotor. The results showed that the shock wave had a large effect on the wake. Upstream of the shock wave the wake depth was reduced and the wake was overturned as a result of an expansion zone in the flow due to the curvature of the rotor blade suction surface. Downstream of the shock wave the wake-deficit increased and the wake was underturned.

Sanders and Fleeter [19], performed PIV measurements on the wake shed from an IGV in a transonic compressor. Their results demonstrated oblique shock effects in the upstream blade row, shedding and boundary layer separation, and unsteadiness in the upstream blade row driven by the downstream rotor.

2.1 Stage Matching Investigation Rig

Several experiments were conducted in the AFRL CARL facility at Wright-Patterson Air Force Base using transonic compressor test rigs. The Stage Matching Investigation (SMI) rig was the first AFRL research compressor to study blade-row interactions. The SMI rig was designed to experimentally reproduce the conditions of an embedded high-speed, highly-loaded transonic compressor stage. An upstream wake generator row, transonic rotor, and downstream stator row configuration was used. The wake generator could be set to three positions denoted as “close”, “mid” and “far” which allowed for a study of the effects on wake generator to rotor axial spacing. The three blade rows and three spacings in the SMI are shown in Fig. 2.1, and mean spacings normalized by the wake generators chord are given in Table 2.1.

Table 2.1: Wake generator axial spacing (normalized by local wake generator chord)

| Spacing | x/c (mean) | x/c (hub) | x/c (tip) |
|---------|------------|-----------|-----------|
| close | 0.13 | 0.10 | 0.14 |
| mid | 0.26 | 0.26 | 0.26 |
| far | 0.55 | 0.60 | 0.52 |

The wake generators were designed to produce a pressure loss typically found in modern technology, highly loaded, low aspect ratio, fan and compressor embedded front stages. Generally these wakes are turbulent and do not decay as rapidly as wakes from high-aspect-ratio stages with lower loading. To simplify the experiments, the wake generators were designed to be uncambered airfoils that do not turn the flow. They were also designed with the intent of producing a two-dimensional representation of wakes measured at the exit of a high-pressure-ratio, low-aspect-

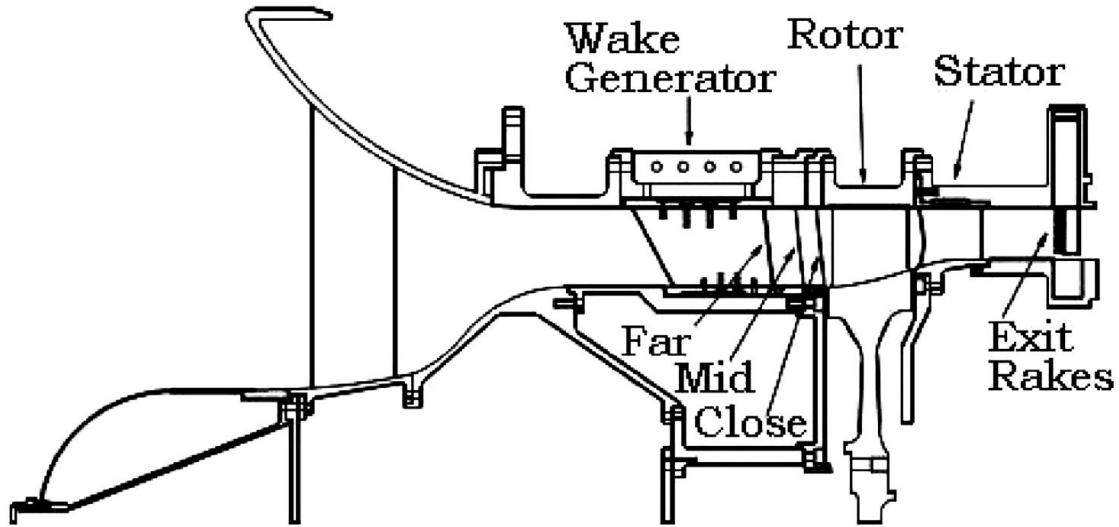


Figure 2.1: Cross-sectional view of the SMI compressor rig (from Gorrell, et al. [1])

ratio fan stage reported by Creason and Baghdadi [20]. Details of the wake generator design were presented by Gorrell et al. [1]. The SMI aerodynamic design parameters are shown in Table 2.2.

Table 2.2: SMI aerodynamic design parameters (from Gorrell et al. [1])

| Parameter | Rotor | Stator |
|----------------------------------|--------|--------|
| Number of airfoils | 33 | 49 |
| Average aspect ratio | 0.961 | 0.892 |
| Inlet hub/tip ratio | 0.75 | 0.816 |
| Flow/annulus area ($kg/s/m^2$) | 195.30 | — |
| Corrected tip speed (m/s) | 341.37 | — |
| M_{Rel} LE hub | 0.963 | 0.820 |
| M_{Rel} LE tip | 1.191 | 0.690 |
| Max D Factor | 0.545 | 0.502 |
| LE tip diameter (m) | 0.4825 | 0.4825 |

Probasco et al. [21] showed that, using the SMI rig in an IGV-Rotor-Stator configuration with close spacing of the IGV, spanwise variation of interaction effects occurred, as well as an unsteady pressure loading on the vane that varied with axial spacing. He also showed that bow

shock influences from the downstream transonic stage were significant and the bow shock influence grew with increased stage back pressure. Effects of axial spacing on flow rate and overflow of an embedded transonic compressor stages were investigated by Chriss et al. [22]. Mixing losses accounted for nearly all losses when spacing between the upstream wake generator and the rotor was more than 50% wake generator chord. As the spacing was decreased, blade-row interaction effects began to influence performance. Shock-wave interaction, blockage associated with wake ingestion by the rotor, and additional 3-D effects became important in determining the maximum mass flow rate.

The effects of blade-row axial spacing on the measured performance of a transonic compressor was presented by Gorrell et al. [2, 4]. Performance characteristics for the SMI rig are shown in Fig. 2.2. Measured data showed that the axial spacing between an upstream stator and downstream transonic rotor has a significant effect on stage performance. He suggested that loss, in addition to mixing loss, was present when the blade rows were close together. Extra loss production occurred as a result of interactions between the upstream wake generator and downstream transonic rotor.

To study in greater detail what unsteady fluid mechanics were responsible for the additional loss observed at close blade-row axial spacing, the SMI rig was analyzed experimentally using Particle Image Velocimetry and numerically. Gorrell et al. [2–4] also performed a study on the effect of blade-row spacing on performance. Previously, Smith [16] had shown that in subsonic compressors axial spacing between the blade rows of an axial flow compressor is associated with improved efficiency. Gorrell showed that mass flow rate, pressure ratio, and efficiency all decreased as the axial spacing between the stator and rotor was reduced in a transonic compressor rig. Reductions as great as 3.3% in pressure ratio and 1.3 points of efficiency were observed as axial spacing between

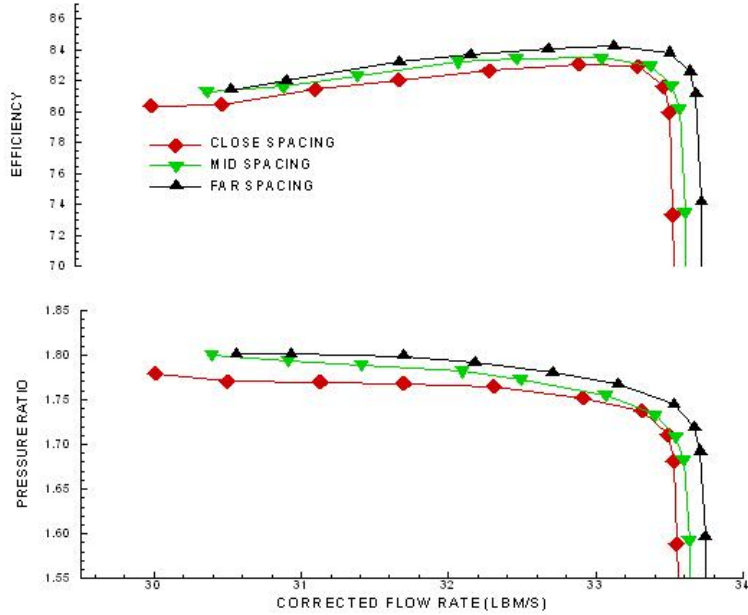


Figure 2.2: SMI performance (from Gorrell, et al. [2])

the blade rows was decreased from far to close spacings. It was also shown that the number of blades in the wake generator row also affected stage performance. Higher stator blade-row solidity led to larger changes in pressure ratio efficiency, and mass flow rate with axial spacing variation. Gorrell suggested that the drop in performance was a result of increased loss production due to blade-row interactions. PIV investigations by Estevadeordal et al. [23, 24] showed wake-blade synchronization, vortex shedding and wake-chopping for the SMI rig. Estevadeordal observed that the wake shedding was synchronized to the passing of the rotor bow shock. This caused the shock and vortices to always be in the same relative position ('phase-locked') resulting in little variation between individual realizations of an ensemble and the ensemble average.

Time-accurate simulations using the 3D, unsteady, Navier-Stokes CFD solver TURBO [3,6] combined with PIV data from the SMI experiment [8] revealed some important aspects of the production of additional loss. The main results of the simulations were that a previously uniden-

tified loss producing mechanism, resulting from the interaction of the transonic rotor bow shock with the trailing edge of the upstream wake generator, produced an increased loss production when the blade rows were drawn closer together axially. At close spacing as compared to far spacing, the rotor bow shock was stronger at the location where it interacted with the wake generator trailing edge (see Fig. 2.3 and 2.4).

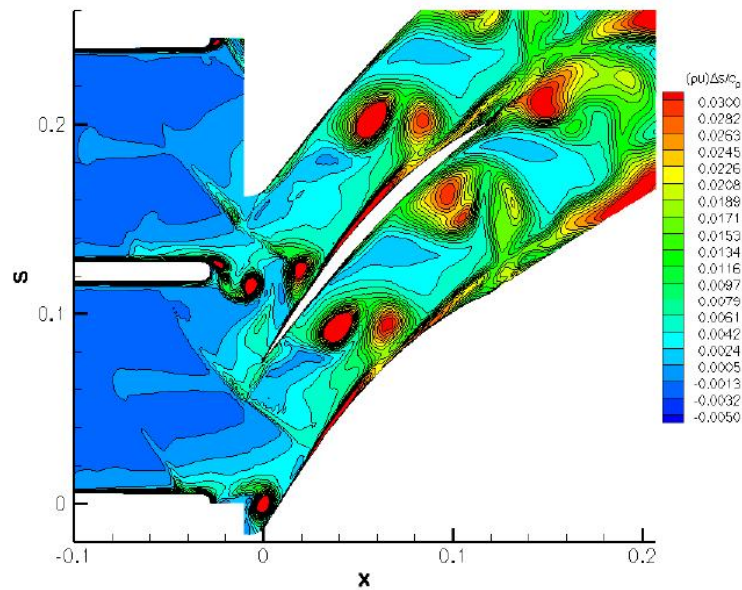


Figure 2.3: Entropy flux contours at close spacing (from Gorrell, et al. [3]).

It was observed that the rotor bow shock formed a pressure wave on the upper surface of the wake generator that propagated upstream. This moving pressure wave produced an entropy rise which resulted in lower efficiency, pressure ratio and mass flow rate. The magnitude of loss production was affected by the strength of the bow shock. It was also determined that at close spacing, vortices were shed from the trailing edge of the upstream stationary blade row in response to the unsteady, discontinuous pressure field that was generated by the downstream rotor bow shock. These shed vortices increased in size and strength and generated more loss as the spacing

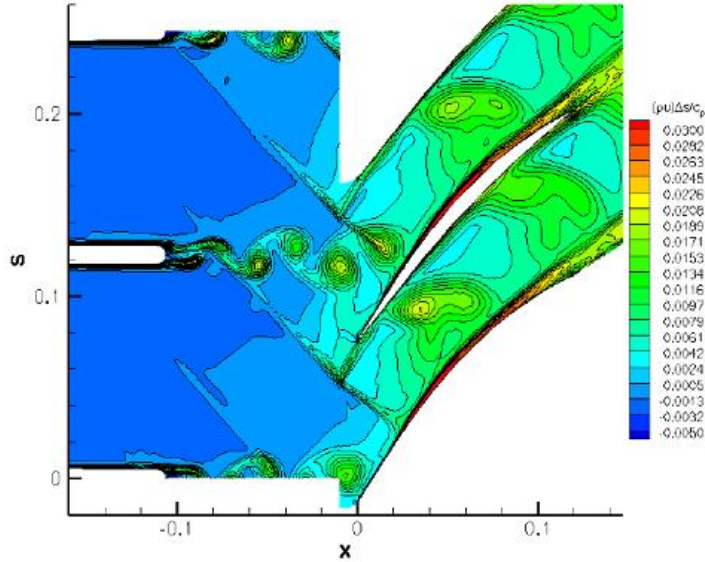


Figure 2.4: Entropy flux contours at far spacing (from Gorrell, et al. [3]).

decreased (see Fig. 2.5). These increases were a consequence of the effective increase in rotor-bow-shock strength at the stationary blade-row trailing edge. A relationship for the change in shed vorticity as a function of rotor-bow-shock strength was presented that captured the change in vorticity between close- and far-spacing TURBO simulations.

Time-accurate simulations of the flow and high-response static pressure measurements acquired on the stator blade surface revealed important aspects of the interaction of the shock with the wake generator. At close spacing the rotor bow shock was chopped by the wake generators trailing edge. The chopped bow shock became a pressure wave on the upper surface of the stator that was nearly normal to the flow and propagated upstream (see Fig 2.6). Using PIV and CFD results, Gorrell concluded that the magnitude of loss production was affected by the strength of the bow shock and how much it turned as it interacts with the trailing edge of the wake generator. At close spacing the interacting bow shock was stronger than at far spacing. At far spacing the rotor

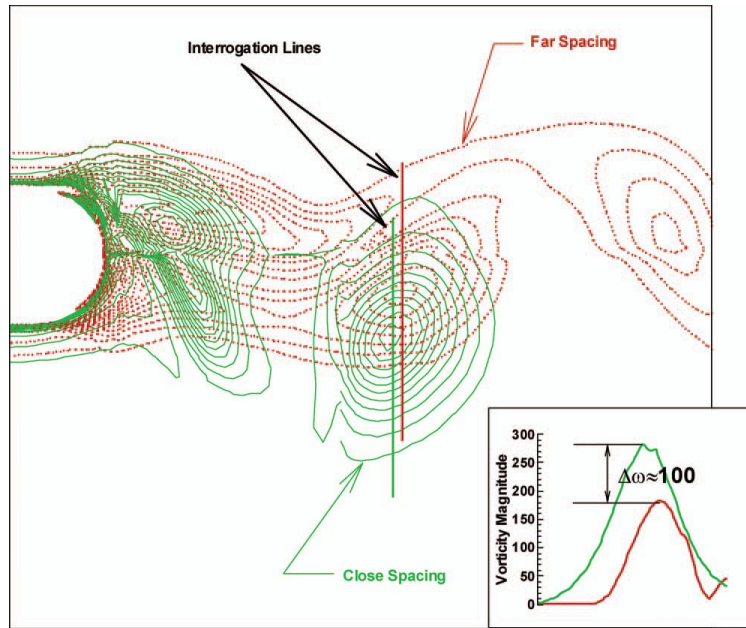


Figure 2.5: Vortex size comparison for Close and Far spacing (from Gorrell, et al. [3]).

bow shock degenerated into a bow wave before it interacted with the stator trailing edge and no significant pressure wave formed on the stator upper surface.

2.2 Blade Row Interaction Rig

In response to suggestions that the observations made in the SMI rig were the results of a blunt wake generator and may not be observed in realistic compressor hardware the Blade Row Interaction (BRI) rig was developed. The BRI rig, shown in Fig. 2.7 was a variation of the AFRL SMI rig. The BRI rig used much of the same hardware with the main difference being the replacement of the blunt, uncambered wake generator of the SMI rig with two upstream stator rows, called the swirler and deswirler (see Fig. 2.8). The rotors used in the SMI and BRI rigs were designed for axial inlet flow and, thus, required a swirler and deswirler to maintain axial inlet flow to the rotor.

These rows generated a wake by diffusion and the deswirler had a realistic stator trailing edge geometry. As the axial inlet flow passed through the swirler row, a tangential velocity (30 de-

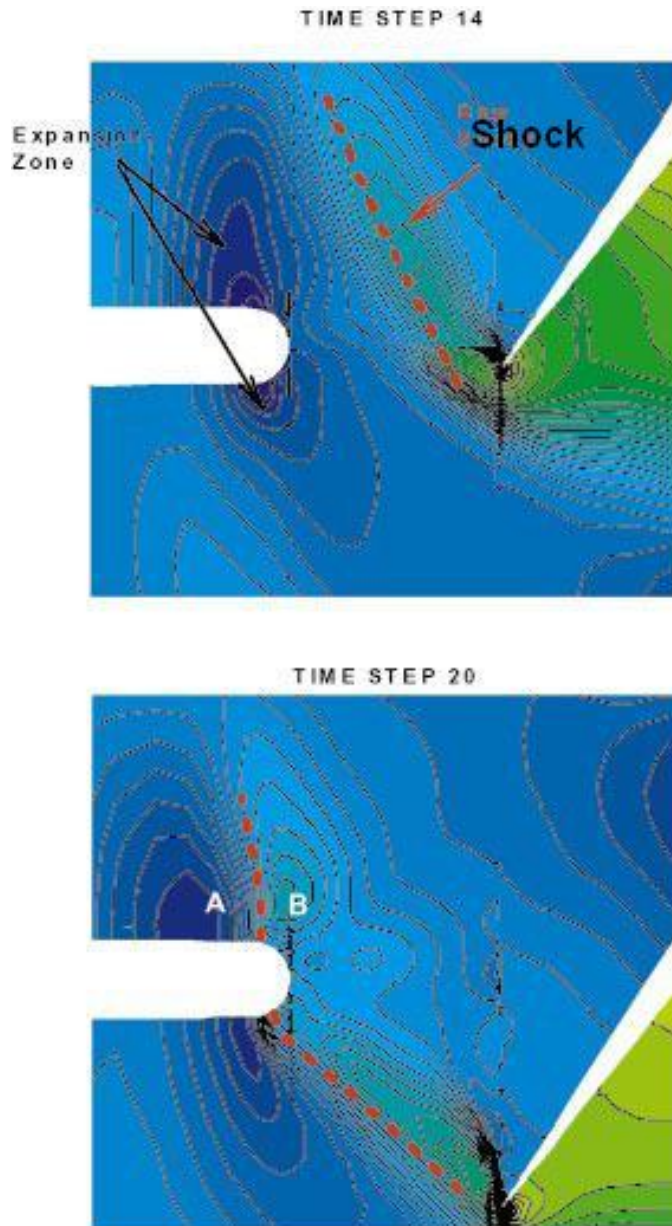


Figure 2.6: Shock turning normal to wake generator at close spacing (from Gorrell, et al. [4]).

degrees of turning) was introduced to the flow. The flow was then turned back to axial flow using the deswirler. The deswirler was highly loaded with a design diffusion factor of 0.45. The design intent was to move the loading as far forward as possible without leading edge separation. Deswirler loading was changed by adjusting the stagger angle of the swirler which changed the incidence to

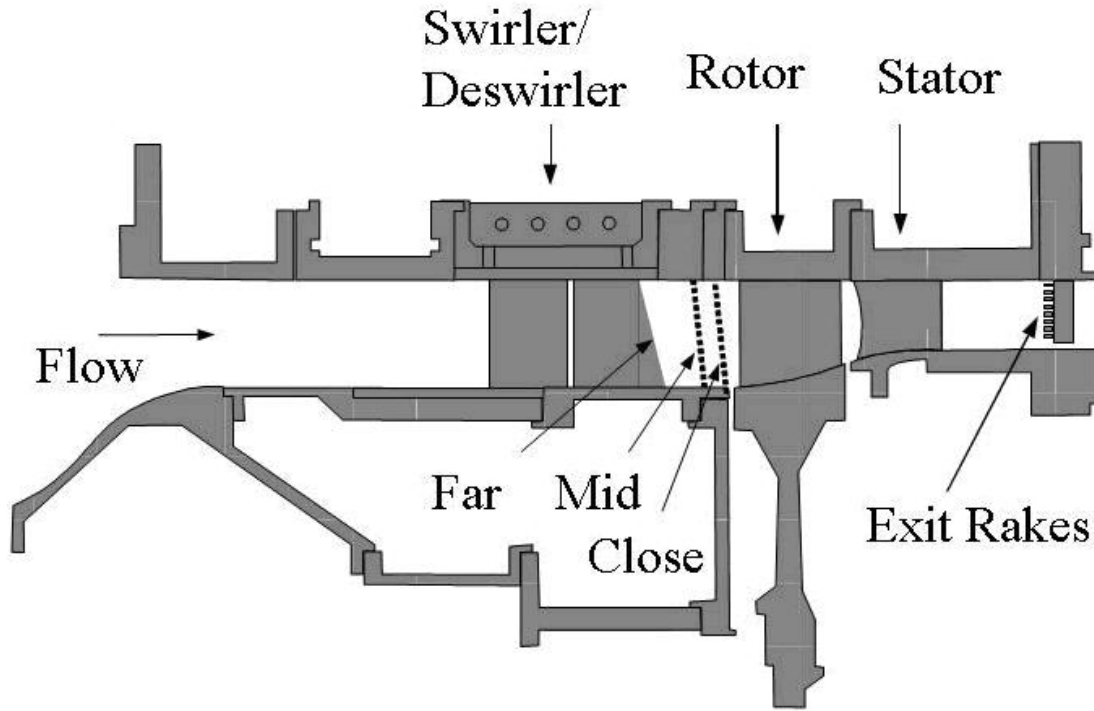


Figure 2.7: Blade-row-interaction (BRI) rig cross section in its general configuration.

the deswirler and consequently the suction side boundary layer thickness. Additionally, the swirler row could be clocked relative to the deswirler to control the pitchwise position of the wake from the first blade row and to optimize the total pressure loss at the entrance of the rotor. A stator row downstream of the rotor was also present. Similar to the SMI rig, the BRI rig was designed to permit the stator-to-rotor axial spacing to be set to three values—“close”, “mid”, and “far” (23%, 48% and 100% of the mean chord of the deswirler)—as shown in Fig. 2.7. Swirler-deswirler geometries at 50% span are shown in Fig. 2.8 along with an actual image of the deswirler trailing edge and rotor in Fig. 2.9.

The total pressure loss coefficient for the swirler-stator combination was measured by inserting a circumferential traverse assembly (rake) between the deswirler and rotor (see Ref. [1]). The loss coefficient is defined by equation 2.1 where P_{rake} is the total pressure measured by the

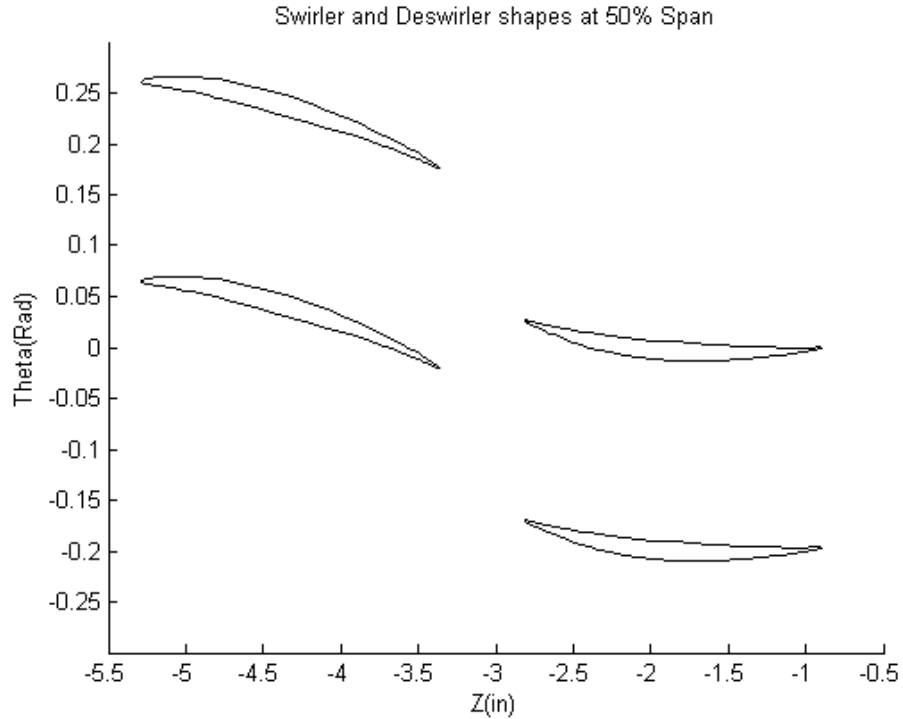


Figure 2.8: Swirler and Deswirler shapes at 50% span.

rake, P_{inlet} is the total pressure measured at the inlet, and p_{inlet} is a static pressure measurement located on the hub flow path just upstream of the swirler.

$$\bar{\omega} = \frac{P_{rake} - P_{inlet}}{P_{inlet} - p_{inlet}} \quad (2.1)$$

The loss coefficient decreased when the stagger angle was changed from 0 degrees to -3 degrees. At close spacing the reduction was 25.6%, mid spacing 16.7%, and far spacing 18.4%. Under such conditions, it is assumed the majority of the change in loss coefficient came from a change in loading of the stator, not the deswirler. Hereafter, a swirler stagger angle of 0 degrees will be referred to as nominal loading and the -3 degree swirler stagger angle will be referred to as decreased loading.

Swirler | Deswirler | Rotor |



Figure 2.9: Photograph of vane of interest in BRI rig.

The design parameters of the BRI rig stage are summarized in Table 2.3. The rotor and stator in the BRI rig were different from those used in the SMI rig. Thus, direct performance comparisons between the SMI and BRI rigs should be done with caution. The SMI simulated an embedded transonic core stage, while the BRI rig simulated an embedded fan stage. The major differences between the fan and core stages are fewer rotor blades (28 in the fan versus 33 in the core) and higher tip speed (414.53 m/s in the fan versus 341.37 m/s in the core), resulting in the tip relative Mach number being increased (1.389 versus 1.191) and the hub relative Mach number being transonic (1.100 versus 0.963).

Experimental and computational methods have been used to analyze the BRI rig. Performance maps for nominal and decreased loading for close, mid, and far spacings are shown in Fig.

Table 2.3: BRI aerodynamic design parameters

| Parameter | Deswirler | Rotor | Stator |
|----------------------------------|-----------|--------|--------|
| Number of airfoils | 32 | 28 | 49 |
| Average aspect ratio | 1.24 | 0.916 | 0.824 |
| Flow/annulus area ($kg/s/m^2$) | — | 196.30 | — |
| Corrected tip speed (m/s) | — | 414.53 | — |
| M_{Rel} LE hub | 0.750 | 1.100 | 0.830 |
| M_{Rel} LE tip | 0.720 | 1.389 | 0.700 |
| Max D Factor | 0.45 | 0.545 | 0.506 |
| LE tip diameter (m) | 0.4825 | 0.4825 | 0.4825 |

2.10 and 2.11. These figures show that with decreased loading efficiency is increased and that at mid spacing mass flow rate is greater than at close or far spacing. This differs from the SMI rig where efficiency was greatest at far spacing and decreased as spacing decreased. Preliminary PIV analysis of the AFRL BRI rig focused on wake shedding and rotor-bow shock strength and position [25, 26]. Qualitative observations were reported using flow visualization, instantaneous and averaged velocity fields, streamline patterns, and vorticity. These studies investigated the phenomena that occurs when rotor bow shocks in axial transonic compressors interact with upstream stator blades. This interaction produced unsteady phenomena such as vortices and separation that induced blockage and losses.

Estevadeordal et al. [25,26] has performed qualitative PIV analysis of blade-row interaction in the BRI rig for different operating conditions and blade configurations. Estevadeordal observed that the vortices shed from the stator are phase-locked and shed as counter rotating pairs in the wake. Similar to the SMI rig, rotor-bow-shock strength varied, depending on the axial gap between the stator and rotor and the operating condition. CFD observations of the BRI rig [4], showed that the shock turns normal to the blade after impacting the trailing edge. The rotor bow shock, after being chopped by the stator's trailing edge, turned more normal to the stator pressure surface and

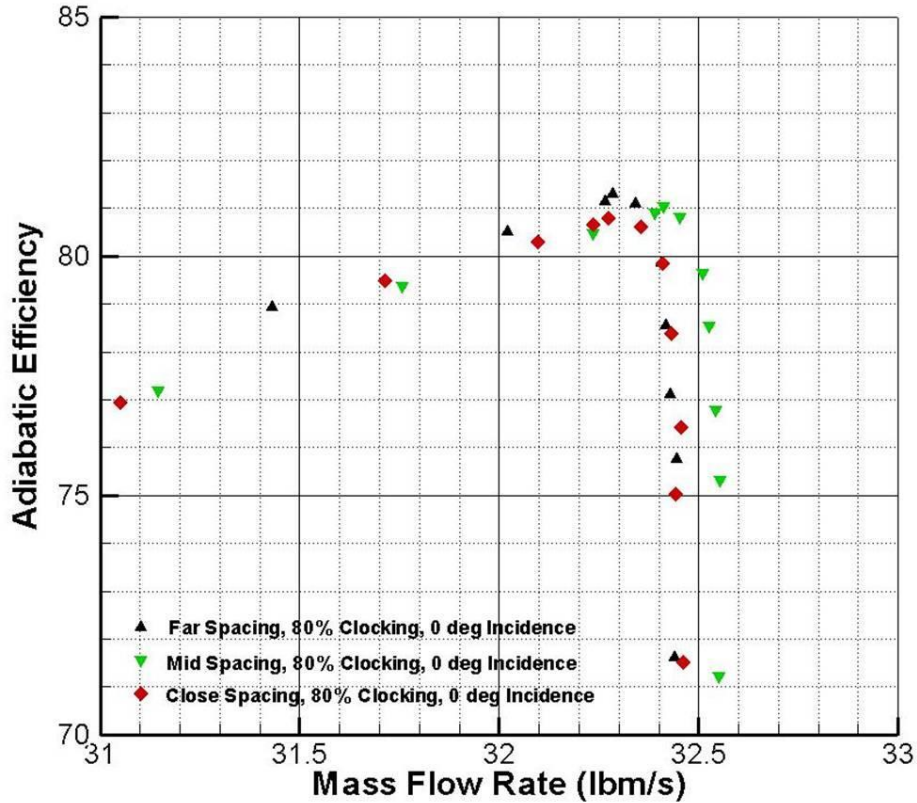


Figure 2.10: BRI performance at nominal loading.

propagated upstream. Estevadeordal also observed that different vortex shapes were produced due to different bow shock strength at near stall and peak efficiency. It was observed that the wake was flatter at peak efficiency with the blade row spacing set to close than at far spacing and that reducing the loading of the stator also produced thinner wakes.

High fidelity modeling of the blade row interactions in the BRI rig were performed by List et al. [10,27]. The resolution of the grids enabled the capture of shed vortices initiated by pressure interactions between the transonic rotor and the upstream deswirler row. List found, using entropy levels at midspan, regions of separation that were not expected based on analysis of the SMI. The cambered airfoil of the deswirler with diffusion is dramatically different from the uncambered airfoil of the SMI rig. List explained the cause of this separation on the suction side of the blade to

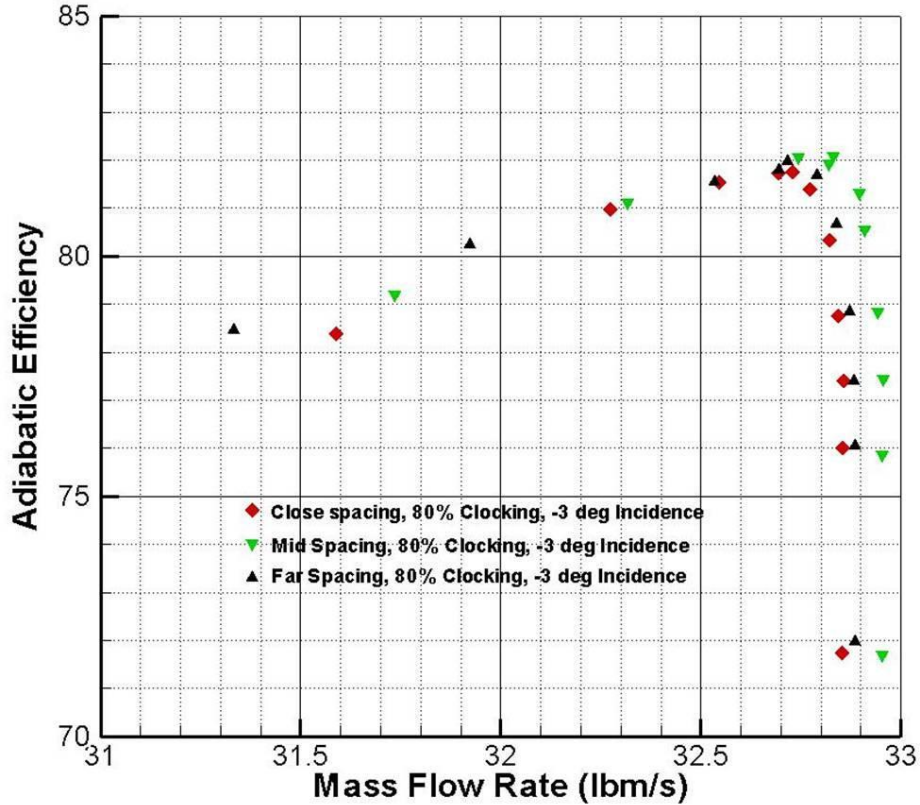


Figure 2.11: BRI performance at decreased loading.

be the result of the shock interaction with the blade and the adverse pressure gradient of the shock which added to the diffusion of the blade. List's [10] numerical investigation of the BRI rig showed that mid spacing exhibited the best performance due to the propagation of the wakes primarily through the center of the rotor passage. Far spacing behaved in much the same way but has a loss region entering the rotor with greater pitchwise extent, accounting for the performance deficit with respect to mid spacing. List also observed that the loss region associated with the closest axial spacing was greatest in spanwise extent and was concentrated closer to the pressure side of the rotor passage where it interacted with the boundary layer resulting in the lowest efficiency of the three spacings. The strength of the rotor bow shock, and thus axial spacing between blade rows, directly affected the strength of the shedding vortices and the wake behavior from the upstream

blade rows. List concluded that the path of the wake migration through the rotor passage impacted the rotor pressure ratio and efficiency.

To further investigate the interaction of a shock with the thin trailing edge of a stator, Langford et al. [5] experimentally studied the interactions between a shock wave formed by a shock tube and the trailing edge of highly loaded stators in a cascade. Using PIV and shadowgraph images, Langford found that as the strength of the shock wave increased, a larger vortex was formed. Langford suggest that the size of the vortex and thus the blockage it produced in the flow path could relate to the change of performance in the SMI rig investigations. Langford modeled a decrease in spacing by increasing shock strength. As a stronger shock impinged upon the upstream stator's trailing edge, more substantial blockage was induced. Langford investigated the blockage and loss associated with the vortex and concluded that the blockage ranged in size from 2.9%-14.3% of the stator pitch for the weakest and strongest shock respectively (see Fig. 2.12). Langford concluded that the loss associated with the vortex was small.

PIV investigation of the Langford's experimental setup by Langford [5] and Esteveordal [28] revealed that the blockage created by the shed vortices may have caused the onset of a suction side separation. However resolution of the affected area did not allow a thorough investigation of any quantifiable losses. It was noted that in a real transonic compressor, compared to the shock tunnel, an expansion wave would follow the bow shock forward causing a sequential loading and unloading causing a change in flow angles and maintaining circumferential periodicity [29]. A computational investigation of the experiment performed by Langford [5] was performed by van de Wall et al. [7]. Van de Wall found that a separation region behind the shock and ahead of the vortex is triggered by the shock, but the blockage of the vortex caused the separation to grow.

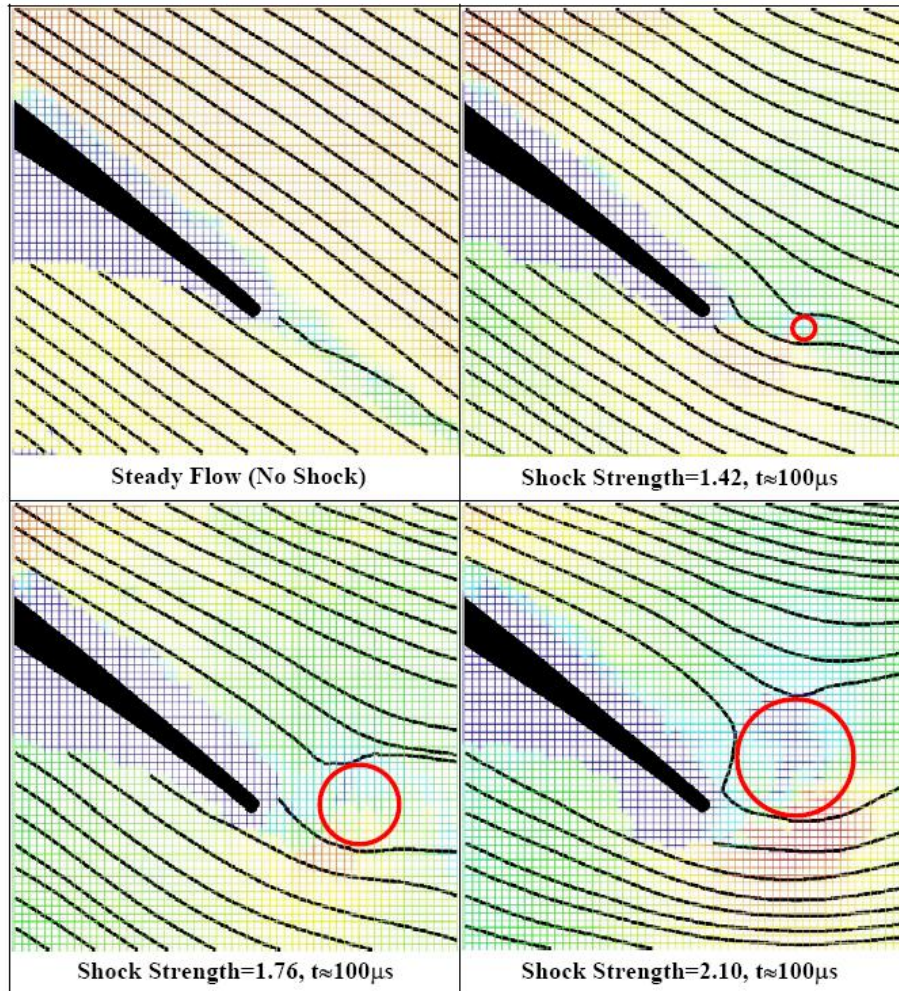


Figure 2.12: Instantaneous streamlines for steady flow and three different shock strengths, with corresponding effective blockage (from Langford, et al. [5]).

Research has shown that unsteady phenomenon are known to play a role in turbine engine operating limits. Experimental and computational research has been performed in order to more fully understand unsteady interactions and the effects of these interactions on performance. However, experimental results have not been presented using realistic stator geometries with a transonic rotor. Also, the effects of changing stator loading on blade row interactions has yet to be performed. The research presented analyzed the effects of stator loading, as well as, blade row interactions using realistic stator geometries located at different axial spacing from a transonic ro-

tor. A better understanding of blade row interactions will allow for designers to more accurately include these interactions into the design of high performance gas turbine engines.

CHAPTER 3. PARTICLE IMAGE VELOCIMETRY

Particle Image Velocimetry (PIV) is an optical method used to measure kinematic properties of a fluid. The fluid is seeded with submicron size particles which closely follow the fluid flow field. A laser sheet, which acts as a flash for a camera, is used to illuminate the area of interest. The particles reflect the light from the laser and are recorded using a digital camera. Using a pair of images recorded only a short time apart, the displacement of the particles can be determined through statistical analysis. From the displacement of the seed particles and the time between the two images the velocity field is obtained.

Several techniques exist for measuring flow velocities. Many of these techniques require placement of probes or other measurement devices that can disrupt the flow field under study. PIV allows for minimally intrusive velocity measurement through optical techniques. This allows the application of PIV to obtain unsteady characteristics in high-speed flows with shocks. PIV also allows for acquisition of an entire plane of velocity data opposed to other methods obtaining only a single data point. PIV enables spatially resolved measurements of the instantaneous flow velocity field within a very short time and allows the detection of large and small scale spatial structures in the velocity flow field. Another advantage of PIV is the capability of comparing 3D CFD results in a straight forward manner, requiring only interpolation of the numerical solution to a grid that matches the position of the PIV laser sheet. This comparison enables validation of numerical codes in order to decide whether the unsteady flow physics have been modeled correctly.

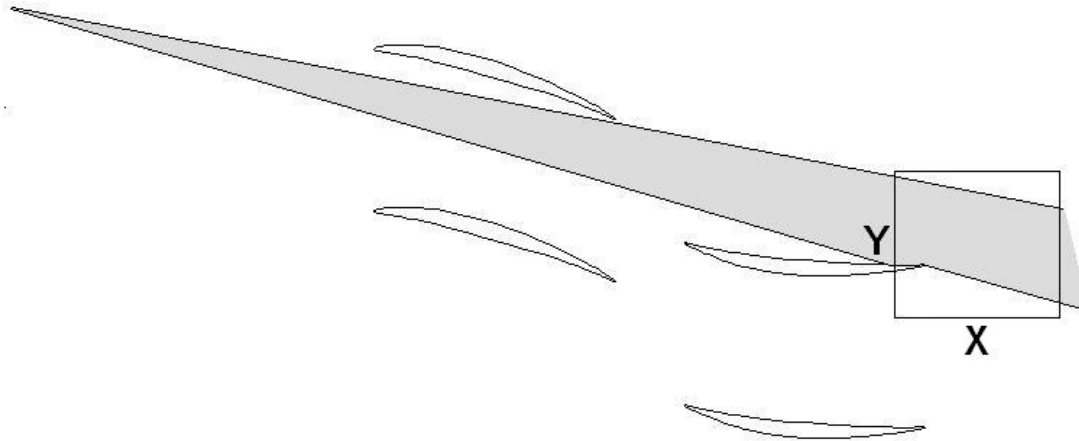


Figure 3.1: Projected laser sheet with squared region of study.

3.1 PIV Setup

The PIV system was developed and used at the AFRL CARL lab with the SMI and BRI rigs [8, 25, 26]. The research presented involved post processing PIV images and analyzing the data. The system included two lasers (Spectra Physics Nd:YAG, 532 nm), for double-instantaneous marking of the sub-micron seed particles in the flow field. The combined beams were directed through sheet-forming optics to illuminate the test section from upstream of the swirler (see Fig. 3.1) with a 2D plane approximately 1 mm thick. High-purity alumina seed particles were used for seeding due to the small-size of the particles with specific gravity similar to that of the air, minimizing particle lag which occurs when crossing a shock and in high speed flows of the compressor [30]. The seeding ports were located upstream of the test article bellmouth (the area of maximum diameter and minimum speed) to exert negligible perturbation on the flow. The seeder tube was located sufficiently far upstream of the PIV window area and injected negligible amounts of air and seed to avoid exerting any significant aerodynamic perturbation in the flow under study.

The light scattering from the seed particles was recorded on a cross-correlation CCD camera with 1600 x 1200 pixels (Model PCO 1600); this camera is capable of acquiring double exposures with an interframe time of 150 nsec. The camera repetition rate was set at 10 Hz for synchronization with the laser repetition rate. A 105-mm Nikon lens was used at an F stop of 5.6. The rotor one-per-revolution signal was used for triggering the synchronization system. A customized interface and a digital pulse generator (Stanford DG535) were employed for synchronization and remote control of the system. The horizontal viewing area was ~ 46 to 67 mm, and the time delay between the two frames of the double exposure was adjusted for each of the viewing areas and its flow speed to provide sufficient resolution and accuracy. In most experiments, this time was set at 1.5 microseconds to yield free-stream displacements around 10 pixels.

3.2 Cross-Correlation and Vector Calculation

From the digitized PIV images, the velocity fields were obtained using Parallel PIV software [31] on the BYU Supercomputer to perform cross-correlation techniques over interrogation domains of the images [30]. This was performed by separating the two images into several rectangular regions (interrogation windows or cells). An interrogation window was selected at a prescribed location on each image. The cross-correlation was performed over the two windows and the location of maximum correlation was identified (see Fig. 3.2). The correlation map was generated using the following steps: Compute the Fast Fourier Transform (FFT) of Cell 1 and Cell 2, transpose the FFT's, multiply Cell 2 by the complex conjugate of Cell 1, zero-pad the results, compute the inverse FFT of the result, transpose the FFT, and then output the results. This process is illustrated in Fig. 3.3. Although computationally expensive, zero padding was used in order to increase the resolution [32].

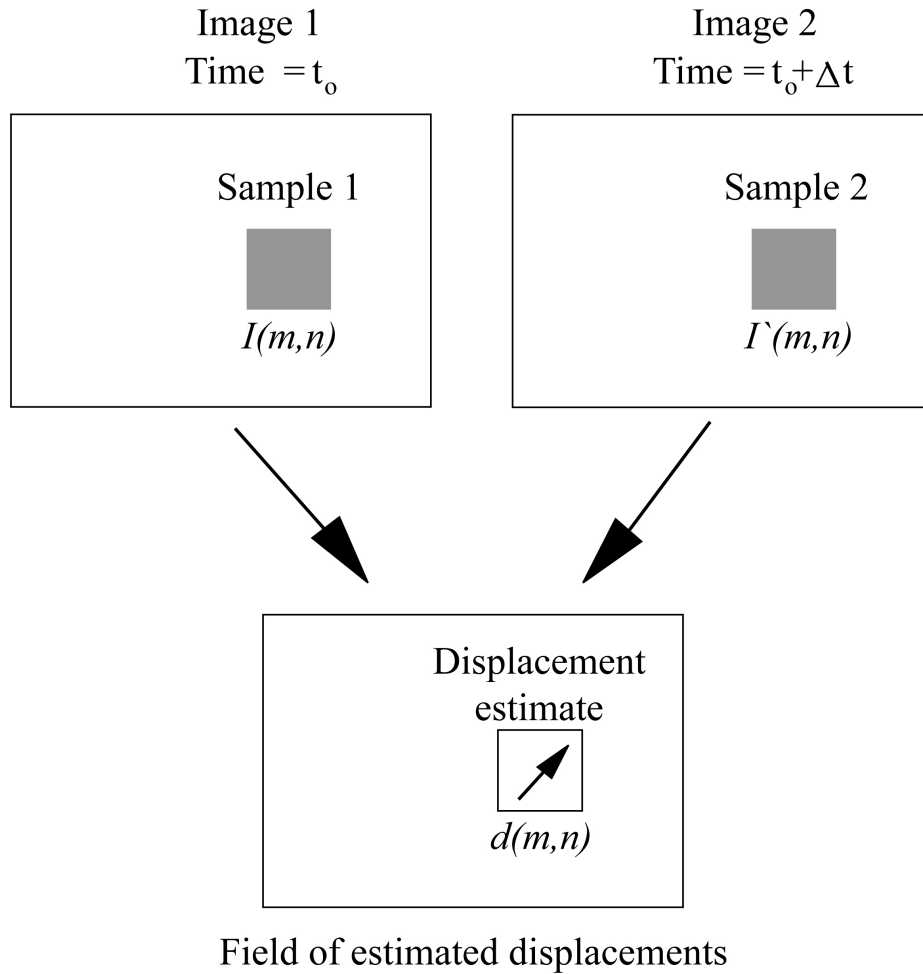


Figure 3.2: Cross correlation over two windows at same location.

Once a correlation map was calculated for a cell pair, the vectors were calculated by extracting a correlation sub-map, locating the maximum value in the correlation sub-map, defining the centroid area, calculating the centroid and then calculating the vector. The correlation sub-map was a square region taken from the center of the original correlation map and was half the size of the original correlation map. This effectively removes the outer pixels of the correlation map, keeping them out of the vector calculations. The centroid area was defined as the area surrounding the maximum point in the correlation sub-map. This surrounding area was defined to be 2 pixels which correlates to the particle radius (see Fig. 3.4). The centroid is calculated using the ratio of

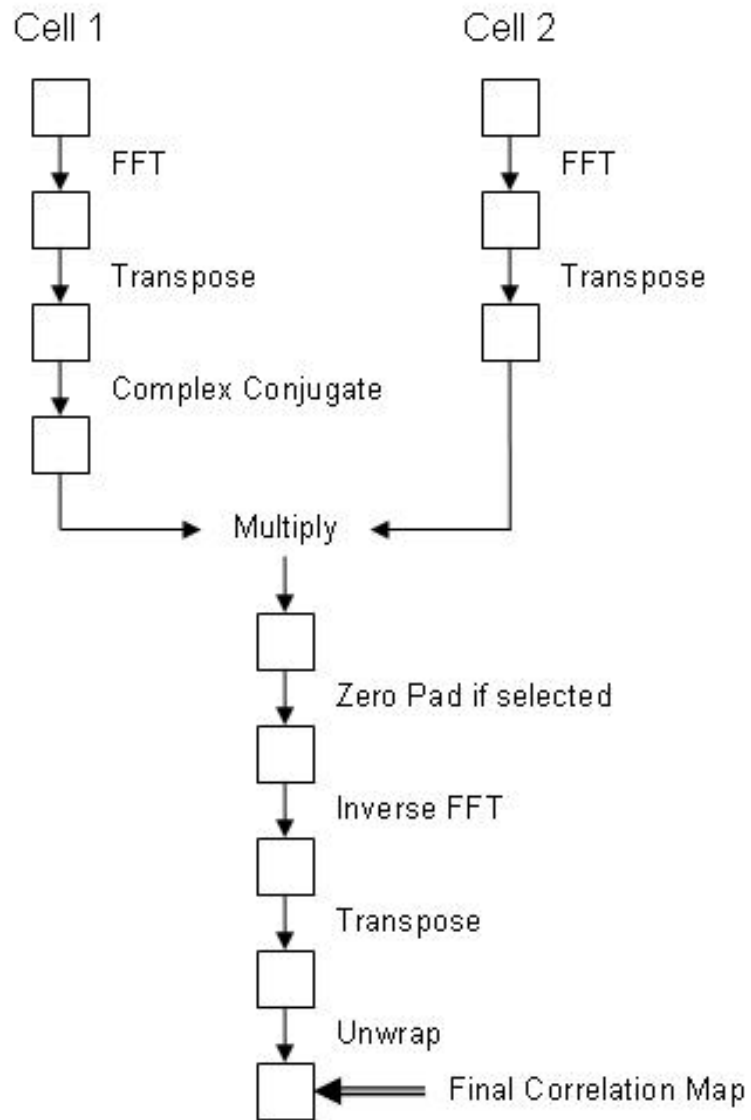


Figure 3.3: Calculations performed in cross correlation.

the first-order to zero-order moments of all the points in the centroid area (see eq. 3.1) where X and Y are the horizontal and vertical centroid, i and j the horizontal and vertical pixel index, C_{ij} is the pixel value at index (i,j) and Bg is the average pixel value of the background. The horizontal or vertical vector was calculated by finding the distance from the centroid to the middle of the cell. Since

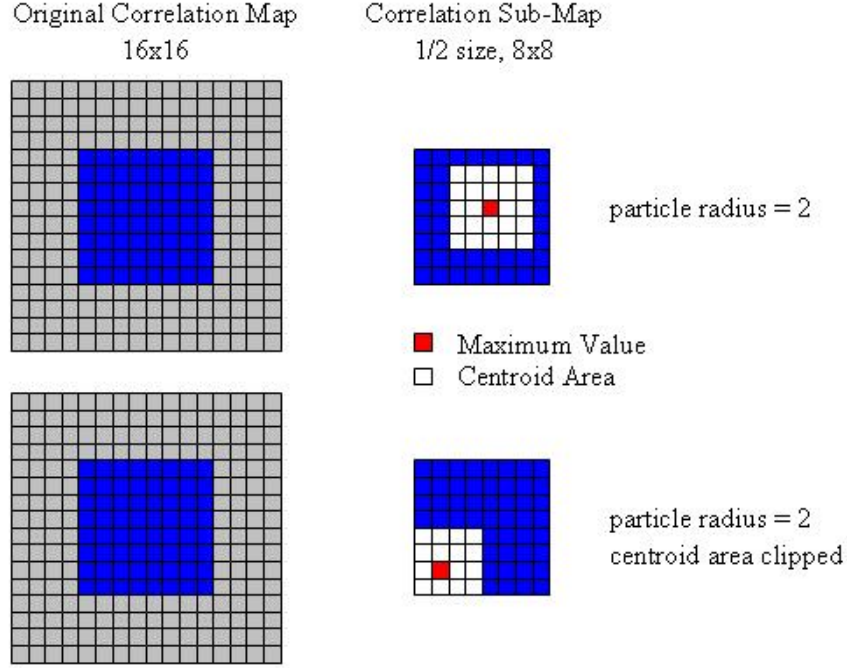


Figure 3.4: Original correlation map, sub-map and centroid area.

zero padding was used equation 3.2 was used to calculate the vectors. U and V are the horizontal and vertical vectors and N is the number of rows or columns in the cell before processing.

$$X = \frac{\sum_{i=left}^{right} \sum_{j=top}^{bottom} i(C_{ij} - Bg)}{\sum_{i=left}^{right} \sum_{j=top}^{bottom} C_{ij} - Bg} \quad Y = \frac{\sum_{i=left}^{right} \sum_{j=top}^{bottom} j(C_{ij} - Bg)}{\sum_{i=left}^{right} \sum_{j=top}^{bottom} C_{ij} - Bg} \quad (3.1)$$

$$U = \frac{1}{2}(X - \frac{N}{2}) \quad V = \frac{1}{2}(\frac{N}{2} - Y) \quad (3.2)$$

The data yield in the interrogation process was significantly increased by using a window offset equal to the local integer displacement in a second interrogation pass [33]. When computing a vector from a cell pair, there may be a case where a particle from the first cell has moved outside the region of the second cell. As an example (see Fig. 3.5), a particle at the position (10,8) moves to the location (30,36). In this situation a cell size of 64x64 would have to be used. How-

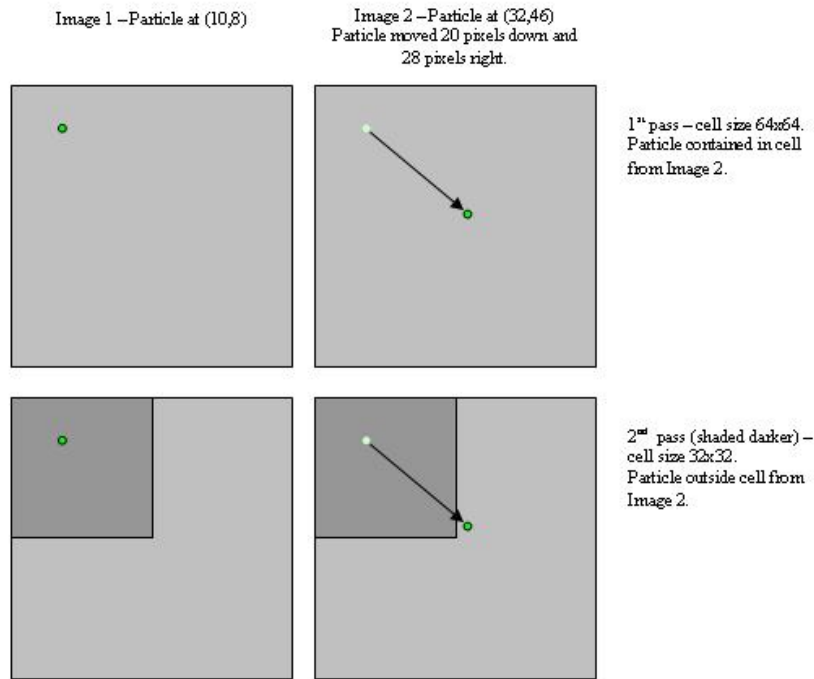


Figure 3.5: Particle has moved outside of reduced interrogation window.

ever, by performing multiple passes with successively smaller grids, the second cell can be moved according to the first vector calculated (see Fig. 3.6). Offsetting the interrogation windows according to the mean displacement and decreasing interrogation window size increased the fraction of matched particle images to unmatched particle images, which increased the signal-to-noise ratio of the correlation peak. This approach increased accuracy of calculated vectors and provided a higher spatial resolution for the final vector map. To maintain high accuracy, two and three passes were performed with interrogation cells overlapping 75%. The two passes were performed starting with a grid size of 128 pixels and then using a grid of 64 on the second pass. The use of only two passes allowed for clear velocity contours, where three passes appeared cluttered, and were used in visually inspecting flow field. The three passes were performed starting with a grid size of 128 pixels, 64 pixels, and then 32 pixels. These results were used in any data analysis allowing

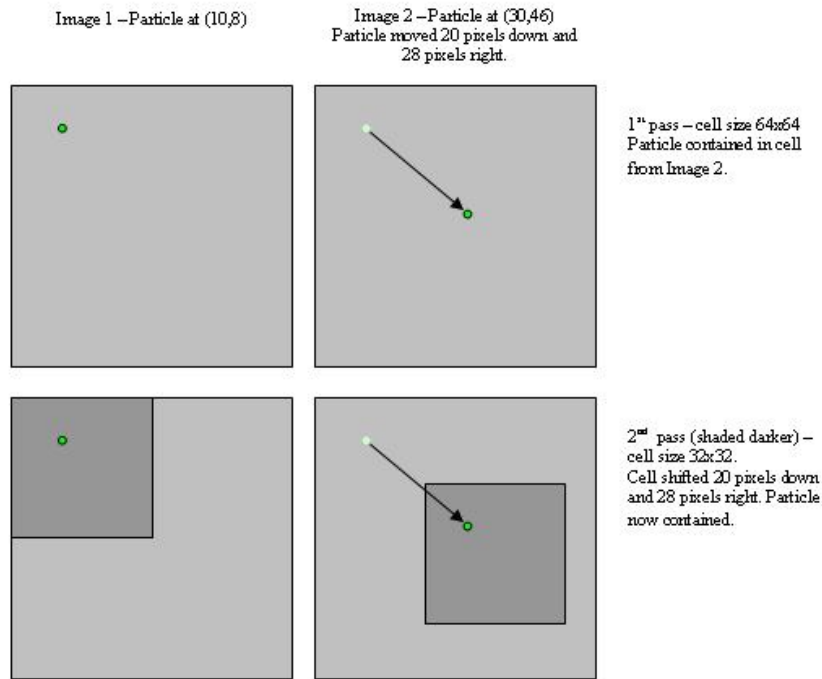


Figure 3.6: Window has been shifted based on results from previous pass.

for more data to be incorporated into calculations for a more complete understanding of the flow. With the 75% overlap the two and three passes yielded a grid resolution of 16 and 8 pixels respectively. Overlapping of interrogation domains yields more vectors. The overlapping is not merely interpolation since it includes new particles in every subregion.

Analyses were performed using an ensemble average from the PIV velocity fields. Although PIV is instantaneous in nature, the temporal evolution of the flow field could not be obtained due to the relatively slow repetition rate of the lasers that were suitable for PIV application within the transonic compressor. Natural phase locking caused by the rotor-blade potential field allowed for the temporal evolution to be inferred from the phased information obtained using an average. In this study the averaged data is presented using the median. The median was less affected by outliers than the mean, does not require that data be normally distributed, and offers a

smooth representation of the ensemble-average velocity fields. The median has also been found to be advantageous when a lower number of realizations are available and when the flow field contains low phase-randomness [34]. Each average velocity field calculation used a sufficient number of realizations (> 50) [35, 36]. Turbulent characteristics would require a higher number of realizations in the average but calculating these characteristics was not an objective of this study. The ensemble-averaging of the instantaneous velocity fields eliminated the fluctuations due to incoherent unsteadiness that are associated with turbulence and allowed for a comparison of the large coherent structures caused by blade row interactions.

Many factors are involved in the instantaneous-PIV uncertainty calculation process (e.g., laser, CCD, seeding, imaging, algorithms, photo diode, and oscilloscope). Uncertainty was established by Estevadeordal in Ref. [8]. The highest uncertainty was found to be associated with the velocity calculation that involves Δx (the displacement in pixels of each interrogation region), Δt (the time interval between the two exposures), and the magnification of the digital image relative to the object (pixel/meter). The displacement in pixels obtained by peak-locater algorithms can provide subpixel accuracy (< 0.1 pixels) after correction for various biases [30]. The Δt was adjusted to yield typical displacements of the main stream of > 10 pixels; the uncertainty of velocity is, thus, $< 1\%$. Values in the wake region, however, may have higher uncertainties due to the lower Δx . The maximum uncertainty in Δt was calculated from the time interval between the two laser light pulses with the aid of a photodiode that was connected to an oscilloscope (uncertainty 2%). It was found that this uncertainty increases with lower laser power and with lower Δt . A conservative uncertainty for the present experiments, which employed a Δt of about $12 \mu\text{s}$ and powers of around 1020 mJ, was found to be 1%. The magnification was measured, using images of grids located in the laser-sheet plane, to better than 1%. Combining these conservative measurements

of uncertainty yields a maximum error of $< 2\%$ in the freestream velocity and $\approx 10\%$ in the wake velocity near the swirler.

The uncertainty that results from various PIV algorithms (e.g., single pass and multipass) and data-filtering techniques (e.g., standard-deviation trimming and median) was also calculated for the average velocity field by Estevadeordal [8]. Mean, standard deviation, median, and median variability were calculated for the data sets and compared for each PIV algorithm and filtering technique. The average velocity field was interrogated at the various representative regions such as the freestreams above the swirler and before and after the shock, the shock regions, and the wake regions. The median variability was calculated using the median absolute deviation (MAD), which is defined as the median of the absolute distances to the median and is computed as an alternative to the standard deviation when that is not available. That was the case in the present experiments with sample sizes of 50 elements, which effectively allowed the computing of only one median. Therefore, its uncertainty, variability, and standard deviation cannot be calculated from a large-series standpoint, which would require a large population of medians. MAD is a robust measure of the median dispersion and does not have restrictions on the underlying distribution (such as normality). The mean uncertainty for Gaussian distributions is reduced by a factor of $1/\sqrt{N}$ (with N being the number of realizations) with respect to the uncertainty of the instantaneous values. If the sample size is low (< 30), a t-distribution test is more adequate to measure confidence [35]. The results showed that, with proper multipass PIV algorithms and data-filtering techniques, the mean standard deviation and the median variability could be decreased to $< 2\%$ and $< 1\%$, respectively, with the median offering more uniform and consistently lower variability in all areas. In the wake region these values increased to 12% and $< 10\%$, respectively, which could be attributed in part to actual phase randomness [34, 37].

At 99% corrected speed, where most of the BRI experiments were performed, consecutive rotor blades were separated in time by 140 μsec (one blade period) corresponding to 11 degrees in angle (blade-row pitch). Seven blade locations (delays/clockings), separated by 20 μsec , were typically chosen to characterize the flow field in a blade-row pitch. Appendix A contains a tutorial explaining the process used in running PPIV program on BYU Supercomputer. Flow visualization images for the seven blade delays for mid spacing at nominal loading can be seen in Fig. 3.7. Flow visualization images of all the blade delays for close, mid and far spacing at nominal and decreased loading are presented in Appendix B.

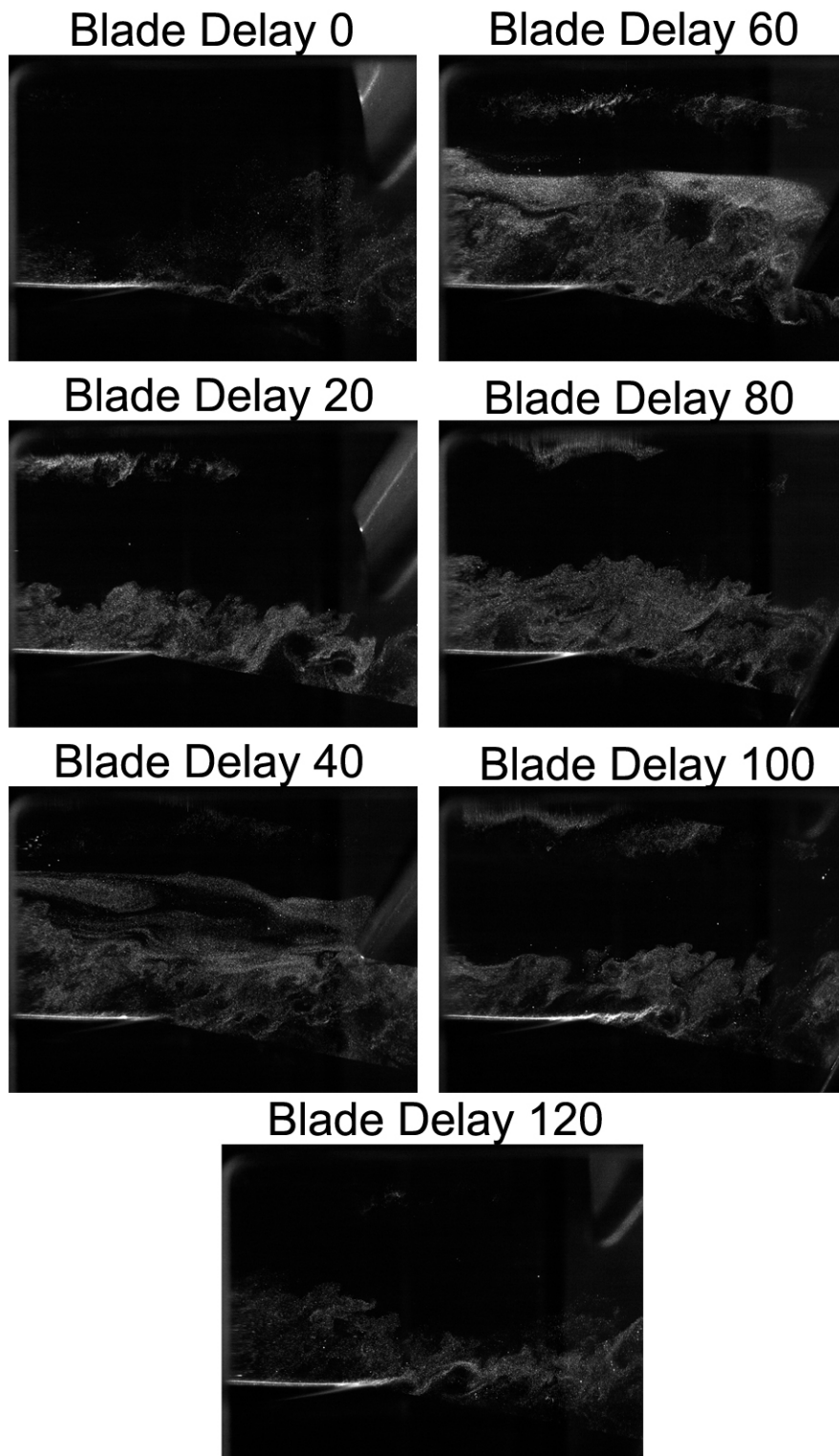


Figure 3.7: Flow visualization of seven blade delay for mid spacing at nominal loading.

CHAPTER 4. RESULTS

This section focuses on describing the unsteady flow downstream of the deswirlers using vortex strength, size and location as a function of loading and spacing. During the experimental investigations of the BRI rig, it was determined that the mid spacing configuration with decreased swirler loading demonstrated the highest efficiency of all configurations. Efficiency increased from close to mid spacing but decreased from mid to far spacing (see Fig. 2.10 and 2.11 for efficiency maps). The interactions between the rotor and upstream deswirlers give insights into one mechanism that affects stage efficiency. For the three spacings (close, mid and far) and nominal and decreased deswirlers loadings (0 and -3 deg swirler stagger), flow visualization and PIV results are shown in the Qualitative Observations section of this chapter. Methods used to calculate vortex characteristics are explained and results of characteristic comparisons are presented. Analysis of observations and calculations with respect to experimental investigations will be presented along with design implications.

4.1 Qualitative Observations

One significant observation from the SMI and BRI experiments has been the synchronization between the wake vortex shedding and the rotor passing frequency [4, 8, 25]. This was attributed to the rotor bow shock impacting the trailing edge of the upstream stator blade producing a change in circulation. On the SMI rig the influence and synchronization between the blade

passage and the vortex shedding decreased with increased axial spacing. This was attributed to a weakened rotor bow shock impacting the stator trailing edge at large axial spacing. It was also observed that the vortex location repeatability with respect to the rotor location decreased with downstream distance. This was attributed to natural downstream wake evolution. With the BRI rig, at closer spacing both the impacting shock was stronger and axial gap smaller so most vortex shedding observed appeared ‘strongly forced’ and ‘phase-locked’ [26] by the rotor passage. Vortex shedding and the synchronization of the shedding with the passing of the shock was determined from examination of various instantaneous flow visualizations, streamlines, and vorticity contours showing vortex shedding variations for a given blade delay (see Appendix B and C).

A flow visualization image displaying a wake from a far-spacing configuration at nominal loading is shown in Fig. 4.1. Figure 4.1 contains a sample picture that combines two independent frames (one colored red and the other green) separated in time by $1.5 \mu\text{sec}$. The rotor-blade position (or blade delay “BLDL”) was synchronized in these samples such that the deswirler trailing edge was aligned at mid-pitch between two rotor leading edge blades (BLDL0). Although shadows from the upstream stator blades prevent visualization of the lower section of the wakes, typical coherent structures of wake vortex shedding can be seen clearly. As with free-wake phenomena, when the wake travels downstream, naturally more wake motion occurs due to the turbulent random nature of the wake vortices [26]. Figure 4.1 shows the deswirler trailing edge, laser sheet edge, rotor, and vortices within the wake. Several vortices have been labeled for convenience in comparing the flow visualization image with other methods of vortex detection. Flow Visualization images for close, mid and far spacings at nominal and decreased loading for all blade delays can be found in Appendix B.

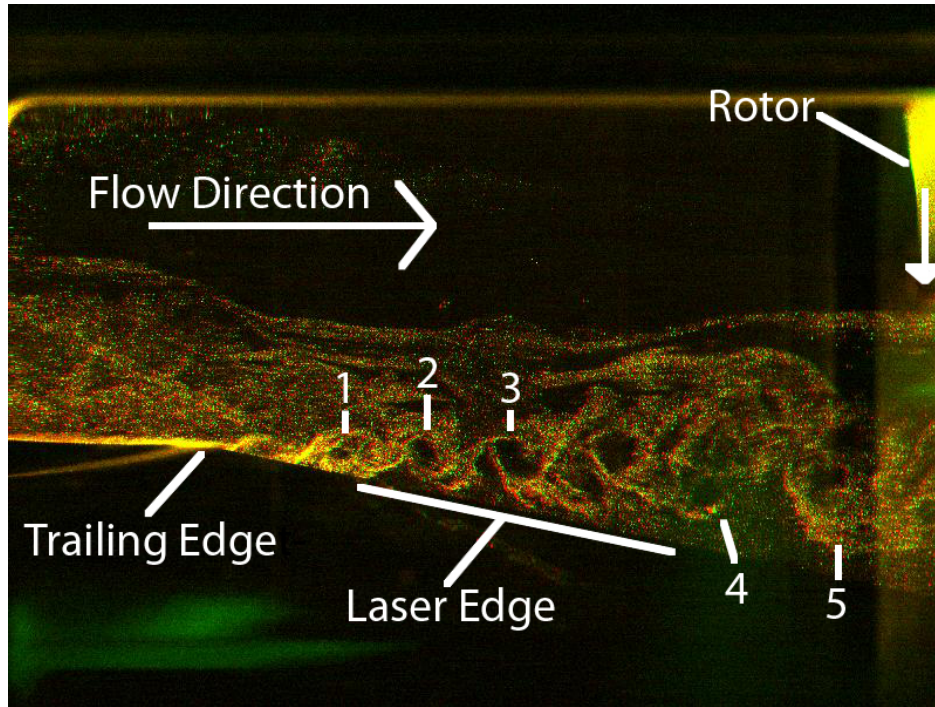


Figure 4.1: Deswirler wake flow visualization for far spacing, decreased loading, BLDL0.

The corresponding PIV velocity field for the instantaneous wake of Fig. 4.1 is shown in Fig. 4.2. A low-speed region that defines the wake can be seen in Fig. 4.2. The velocity vectors show the overall flow from the deswirler into the rotor (left to right). A slight change in direction can be seen in the vectors as the flow crosses the shock causing the flow to turn towards the shock. Speed contours with velocity vectors overlaid show the abrupt change in velocity across the shock and the slower wake region more clearly. The individual vortices observed in the flow visualization cannot be seen or traced in the velocity field until their convective velocity have been subtracted. Convective velocity is defined as the velocity at which the vortices propagate downstream. The convective velocity for near and far fields were estimated as the velocities at the center of vortices located near the deswirler trailing edge and far from the trailing edge. Figure 4.3 show the velocity field with streamlines and the near field and far field convective velocities subtracted, allowing for visualization of the vortices near and far from the deswirler trailing edge. The vortices labeled in

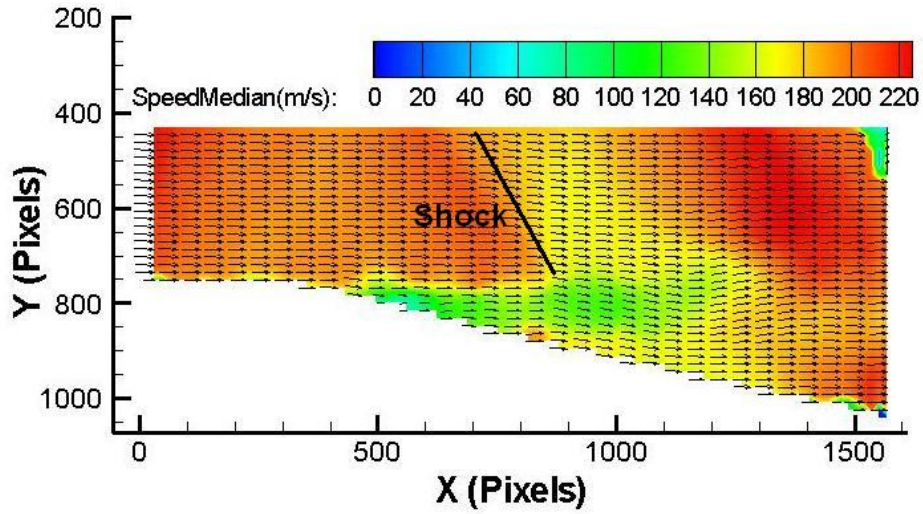


Figure 4.2: Average velocity vectors obtained from PIV for far spacing, decreased loading and BLDL0 with average speed contour showing decreased velocity of the wake and abrupt change of velocity and direction across the shock.

Fig. 4.1 are also labeled in Fig. 4.3. Vortex characteristics, such as a saddle, can be seen between vortex 2 and 3 when the near field convective velocity is subtracted. Figure 4.4 shows a close up on the saddle between vortex 2 and 3. These images and other images like them were used in tracking vortices and flow features at all blade delays and in locating vortex position to perform comparisons between compressor configurations. Speed contours for close, mid and far spacings at nominal and decreased loading for all blade delays can be found in Appendix C.

Averaged vorticity fields (Fig. 4.5), which are invariant with respect to frame of reference, identifies vortices of the wake and reveals the typical counter-rotating vortex pairs. Vorticity was calculated using the central difference method to solve eq. 4.1.

$$\omega_z = \frac{\partial v}{\partial x} - \frac{\partial u}{\partial y} \quad (4.1)$$

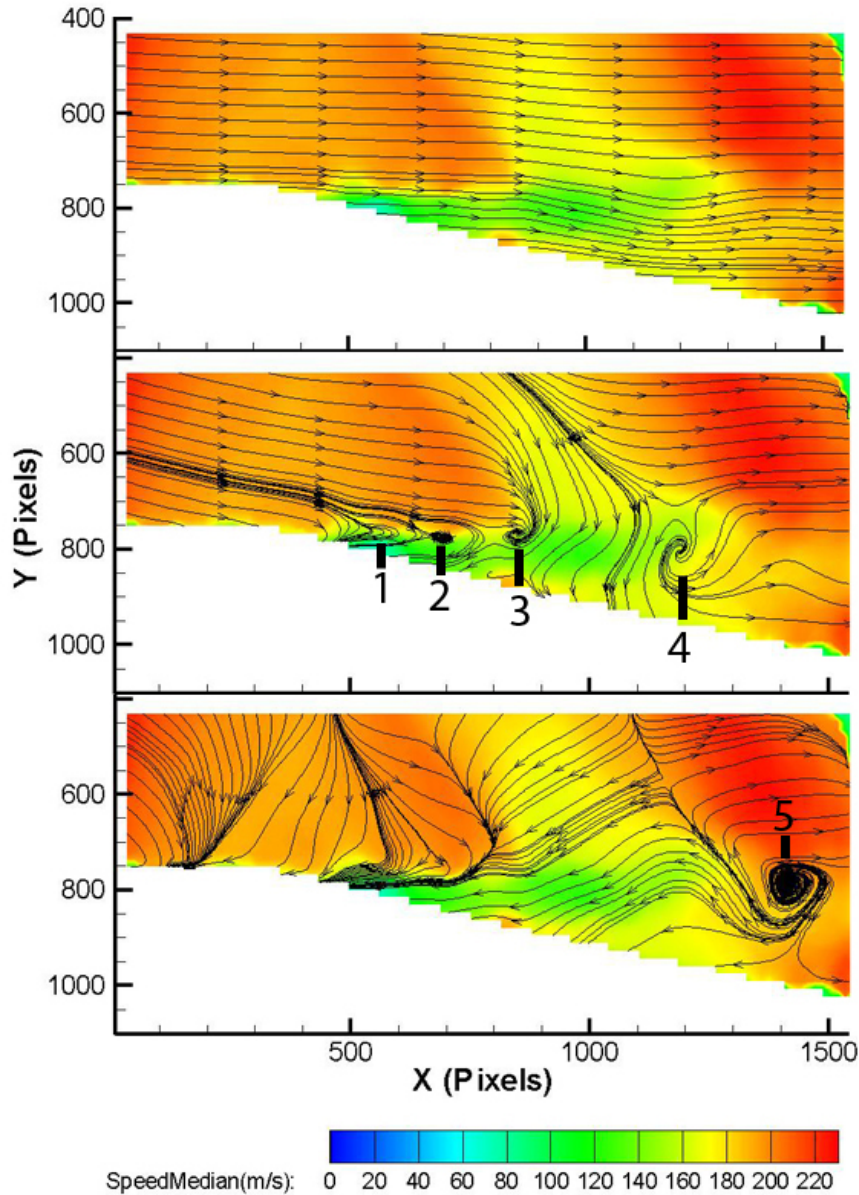


Figure 4.3: Streamlines of average velocity field of Fig. 4.1; Top image: no convective velocity subtracted, Middle image: near-field convective velocity subtracted, Bottom image: far-field convective velocity subtracted.

Although several methods were investigated (forward differences, central differences, Richardson extrapolation and least-squares approach [30]) the central difference method was chosen due to the relative accuracy, allowing for a comparison between blade delays and compressor configurations,

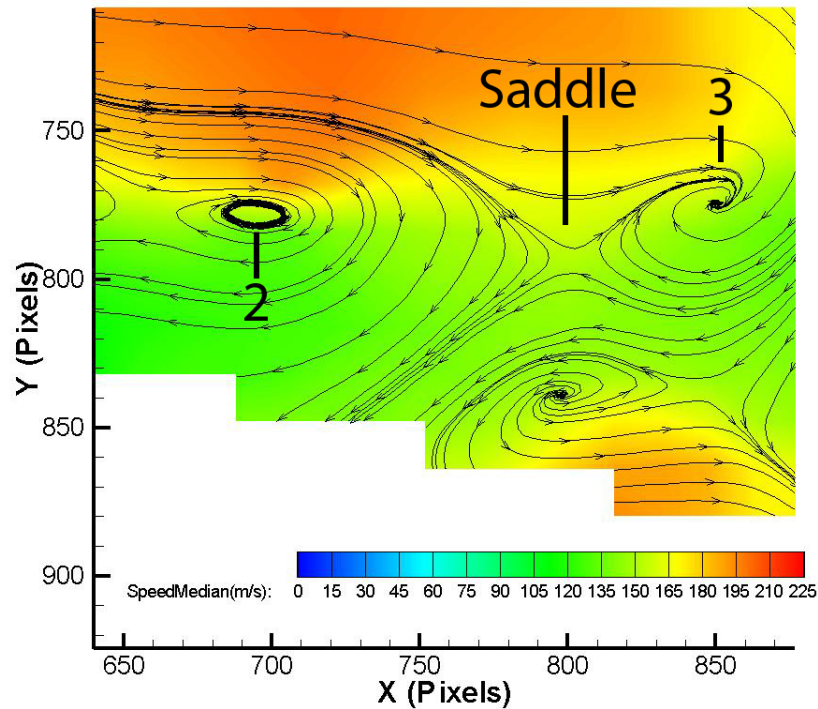


Figure 4.4: Close up of streamlines used to show the saddle between two vortices when convective velocity has been subtracted.

and ease of calculation using the program Tecplot [38]. Vorticity fields for close, mid and far spacings at nominal and decreased loading for all blade delays can be found in Appendix D.

It is worth noting that the vortices do not become washed out in the averaged velocity field. This is an indication that for a fixed blade clocking, these vortices are locked at a spatial location, which is similar to the “phase-locked” phenomena observed in the SMI rig [3, 8]. Analysis of the vortex path and its synchronization with the blade location were performed through examination of the various blade delays using flow-visualization images, streamlines and averaged vorticity fields. These observations are described in the Far Spacing and Mid and Close Spacing sections of this chapter.

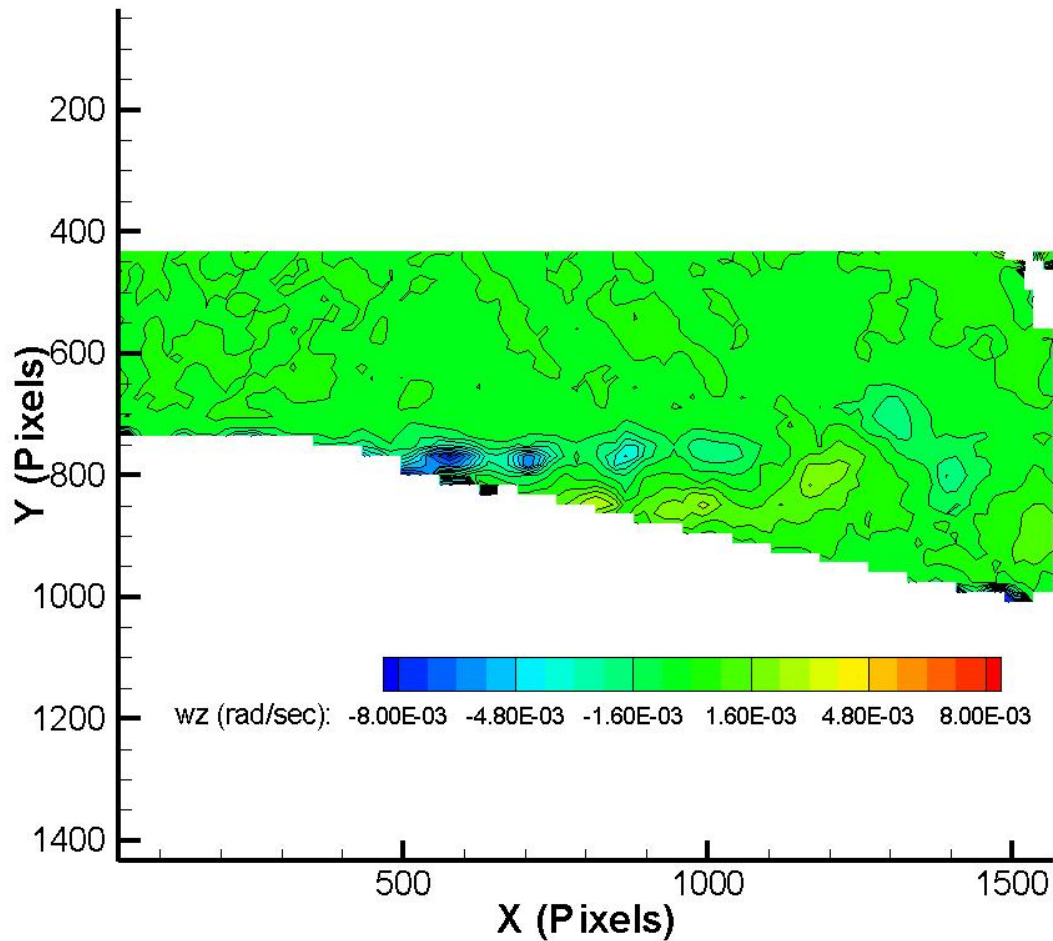


Figure 4.5: Vorticity contours of average velocity field of Fig. 4.1.

4.1.1 Far Spacing

Figures 4.6 and 4.7 present the velocity field with vorticity contours for far spacing at nominal and decreased loading using a coarse grid (two iterations, 64 pixel cell resolution, 75% cell overlap) to introduce the general flow field evolution in one blade period. These velocity contours show the upstream progression of the rotor-bow shock and the shedding of vortices within one blade period. They also show the main features of the compressor flow such as the low-velocity

region of the wake, the abrupt changes in velocity across the shock, and the accelerating flow region into the rotor passage. When comparing velocity contours for far, mid and close spacing it should be noted that magnification varies from $35 \frac{\text{pix}}{\text{mm}}$ for close spacing, $34 \frac{\text{pix}}{\text{mm}}$ for mid spacing and $24 \frac{\text{pix}}{\text{mm}}$ for far spacing. Thus the x and y axes in pixels correspond to different distances in meters at close, mid, and far spacing.

Figures 4.6 and 4.7 show that the shock impacts the trailing edge of the deswirler between blade delay 100 and 120. Three vortices, labeled **A**, **B** and **C** for nominal loading and **A'**, **B'** and **C'** for decreased loading, are shed for one blade period. These vortices were traced back to their time of shedding by using PIV data and flow visualization images due to the lack of complete PIV velocity data close to the trailing edge of the deswirler and laser field edge. The vortices labeled **A**, **B** and **C** in Fig. 4.6 first appear around blade delays 20, 60 and 120 respectively. The corresponding vortices **A'**, **B'** and **C'** for decreased loading were shed at the same blade delays as nominal loading. The exact moment of vortex shedding is unclear due to the $20 \mu\text{sec}$ time delay between images and the lack of visible seeding on the suction surface of deswirler.

A comparison of the blade periods for far spacing at nominal and decreased loading show several distinct differences. The vorticity of the vortices for nominal loading appears to be greater than that of the vortices at decreased loading. This will be discussed further in the Vortex Strength section of this chapter. Another noticeable difference between nominal and decreased loading is the difference between the vortices labeled **C** and **C'**. Analysis of flow visualization images and vorticity contours show that both vortices appear to be shed around blade delay 120. This shedding occurs close to the same time that the shock impacts the trailing edge of the deswirler. The vortex **C** is a well developed vortex; however the corresponding vortex at decreased loading **C'** appears

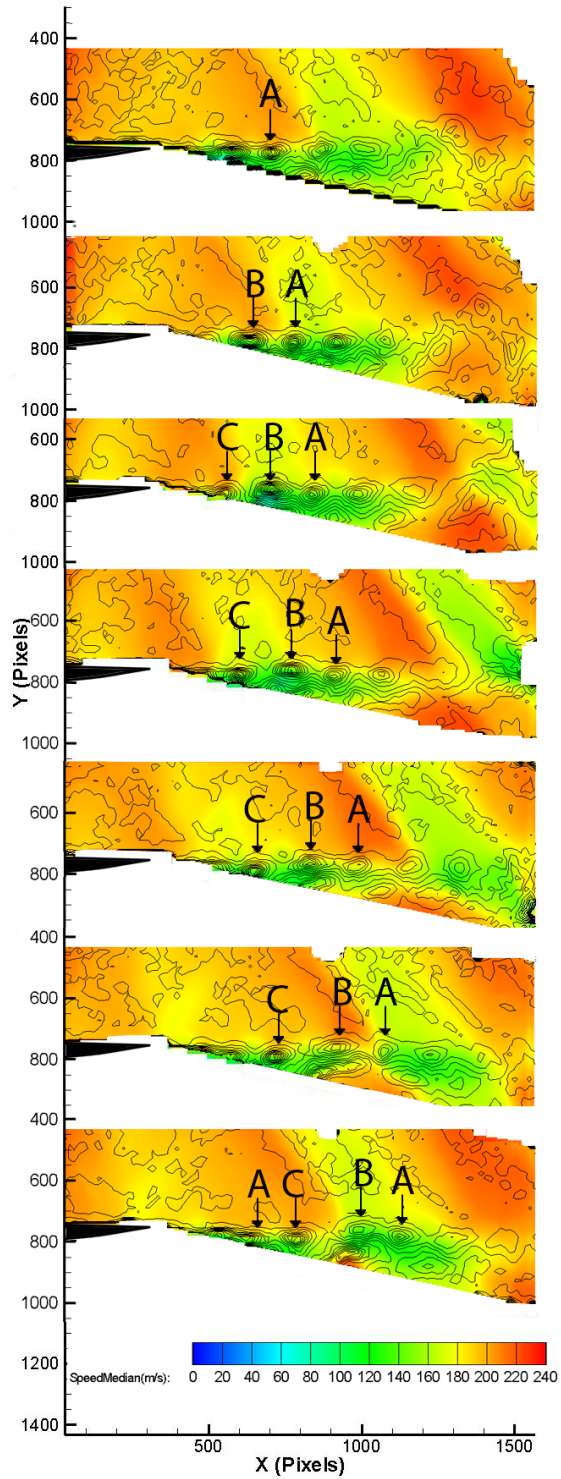


Figure 4.6: Far spacing, 50% span, at nominal loading. Median velocity with vorticity contours for one blade period (0, 20, 40, 60, 80, 100, 120 μsec blade delay from top to bottom).

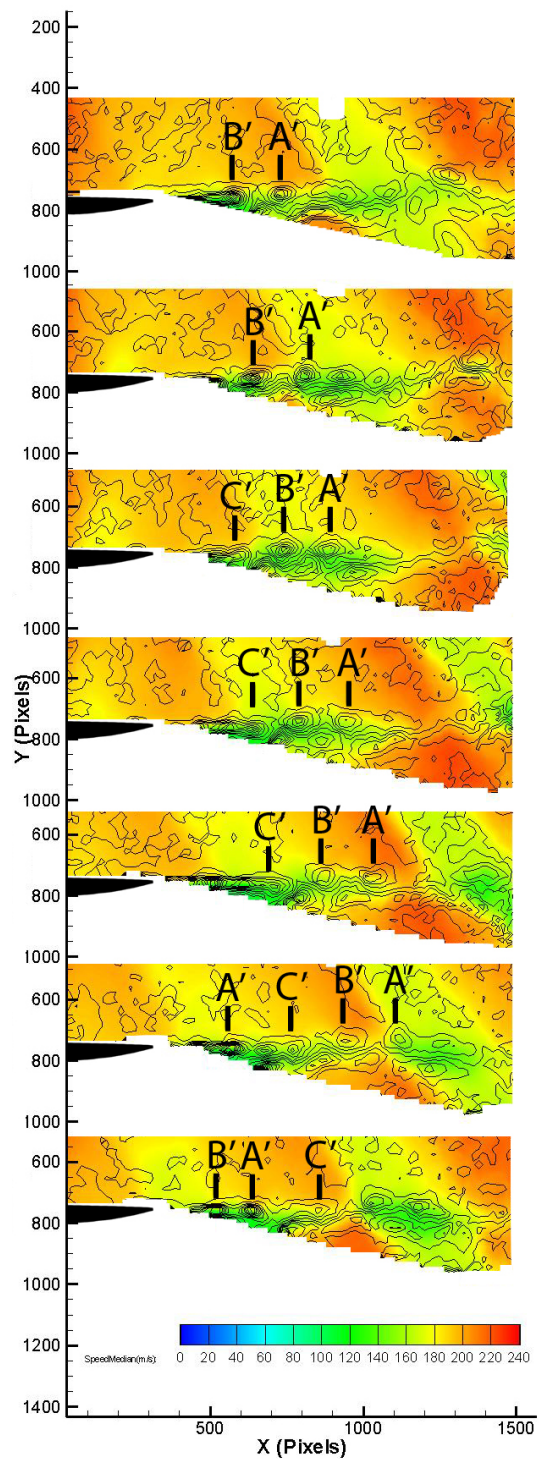


Figure 4.7: Far spacing, 50% span, at decreased loading. Median velocity with vorticity contours for one blade period (0, 20, 40, 60, 80, 100, 120 μ sec blade delay from top to bottom).

to have lower vorticity and not a strongly defined vortex core. The strength of these vortices will be compared in the Vortex Strength section of this chapter.

4.1.2 Mid and Close Spacing.

Figures 4.8 and 4.9 show the blade period for mid spacing at nominal and decreased loading. Similar to far spacing, three vortices are shed labeled **A**, **B** and **C**. After following the progression of the shock upstream using PIV data and flow visualization images (see Appendix B, C and D), vortex **C** appears to be shed close to blade delay 120 which coincides with the same blade delay that the shock impacts the trailing edge of the swirler. Vortices **A** and **B** are shed while the shock propagates up the deswirler at blade delay 20 and 40. The vortices at decreased loading, **A'**, **B'** and **C'**, are shed at similar blade delays as those at nominal loading. Similar to decreased loading at far spacing, the vortices appear to have weaker vorticity. It is also noted that vortices **C** and **C'** for mid spacing have lower vorticity values compared to **A**, **A'**, **B** and **B'** at mid spacing which was not obvious from Fig. 4.6 and 4.7 for far spacing. This will be discussed in the Vortex Strength section of this chapter. Figure 4.10 shows the blade delays of close spacing at nominal loading. Many of the blade delays for close spacing only show limited velocity data due to the rotor passing close to the trailing edge which decreased the visible flow field. Similar to what was observed at mid spacing a large and small vortex are present.

A visual comparison of the vortices and a study of shock location lead to the belief that the large vortices, labeled **A**, **A'**, **B** and **B'**, for all spacings are generated as the shock propagates up the deswirler. These vortices appear to be similar to the large vortices created by Langford's linear cascade shock experiment [5]. The vortices generated by Langford's experiments were shed in response to the unsteady increase in circulation on the stator that was induced by the shock. These

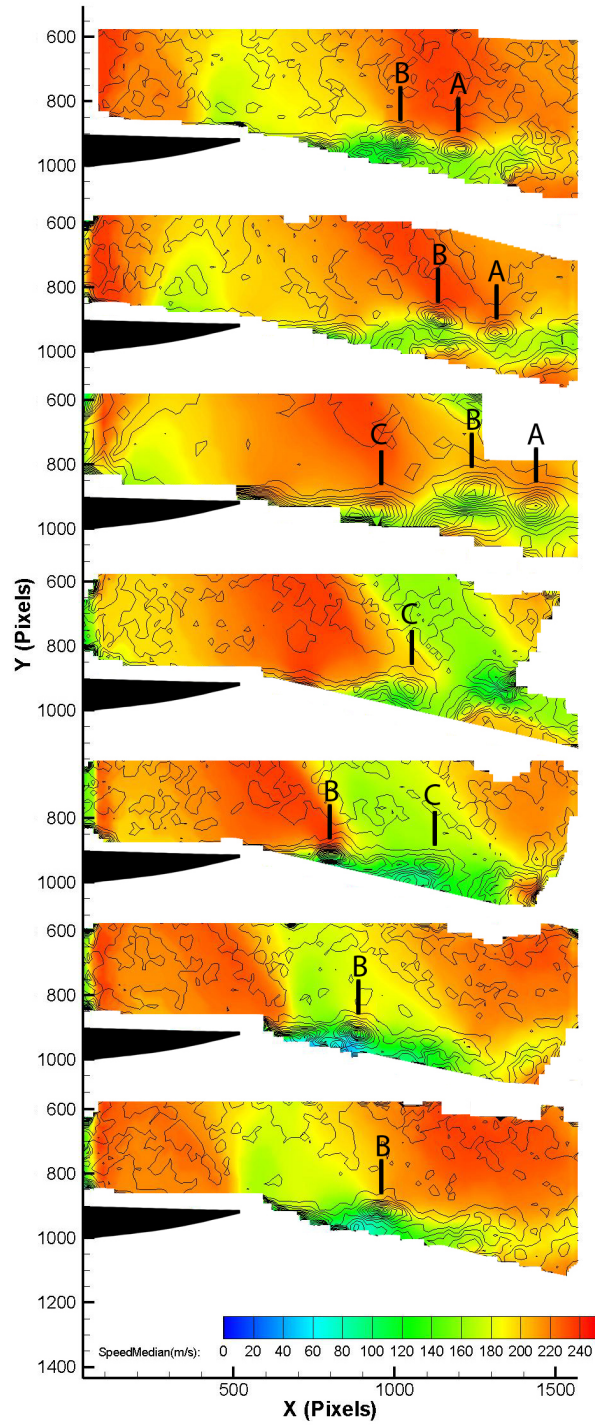


Figure 4.8: Mid spacing, 50% span, nominal loading. Median velocity with vorticity contours for one blade period (0, 20, 40, 60, 80, 100, 120 μ sec blade delay from top to bottom).

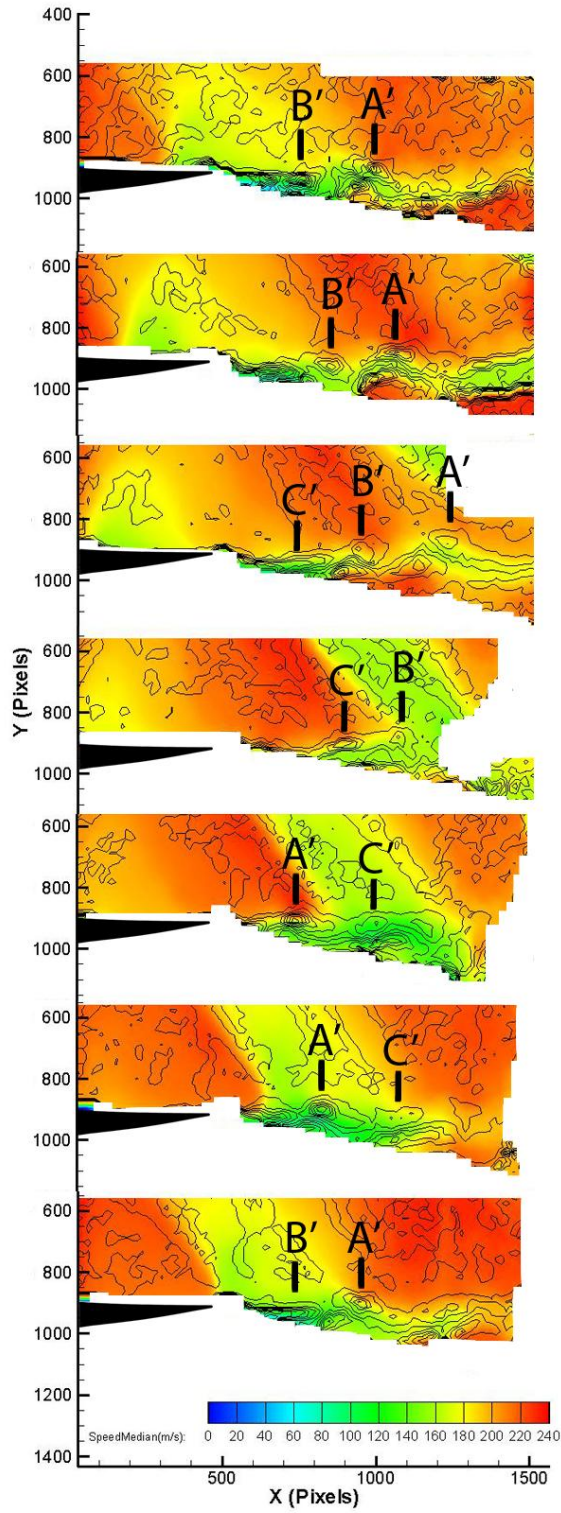


Figure 4.9: Mid spacing, 50% span, decreased loading. Median velocity with vorticity contours for one blade period (0, 20, 40, 60, 80, 100, 120 μ sec blade delay from top to bottom).

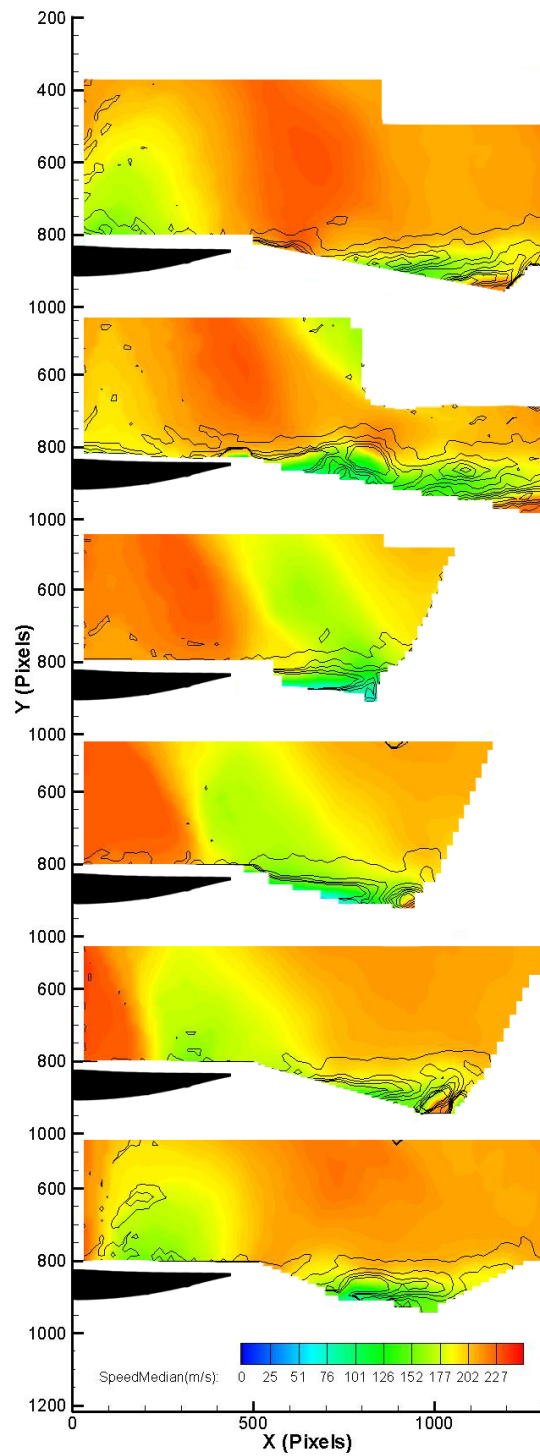


Figure 4.10: Close spacing, 50% span, nominal loading. Median velocity with vorticity contours for one blade period (0, 40, 60, 80, 100, 120 μsec blade delay from top to bottom).

vortices were found to increase in strength as shock strength was increased. The strength of the vortices labeled **A**, **A'**, **B** and **B'** will be investigated to determine if these vortices are a result of the interaction of the shock with the trailing edge of the deswirler.

4.2 Vortex Characteristics

Vortex characteristics such as vortex strength and size allow for quantitative comparisons between compressor configurations. These characteristics are discussed for close, mid and far spacings with nominal and decreased loading.

4.2.1 Vortex Radius

A visible difference between close, mid and far spacing and nominal and decreased loading was the size of the vortex. Gorrell et. al. [3] explained that a vortex was shed from the stator trailing edge in response to the unsteady increase in circulation on the stator caused by the passing of a shock. Langford also showed that vortex size increased directly with shock strength [5]. Here, the radius of the vortex was used to compare the size of the vortices between close, mid and far spacing. Vortex size can be used to understand the amount of blockage occurring between blade delays. As can be seen in Fig. 4.2, the wake propagates down stream at a slower velocity. The larger the wake region the slower the flow entering the rotor which can then affect the mass flow rate and compressor performance. The distance between the minimum and maximum velocity along a line passing through the center of the vortex is the vortex diameter $d(\theta)$. Measurements were repeated over several directions with $\theta \in [0, \pi]$. From the distance between the locations of maximum and minimum velocity the vortex core diameter and radius were obtained. Figure 4.11 shows the grid where points were taken to calculate vortex diameter. To account for the non-circular geometry

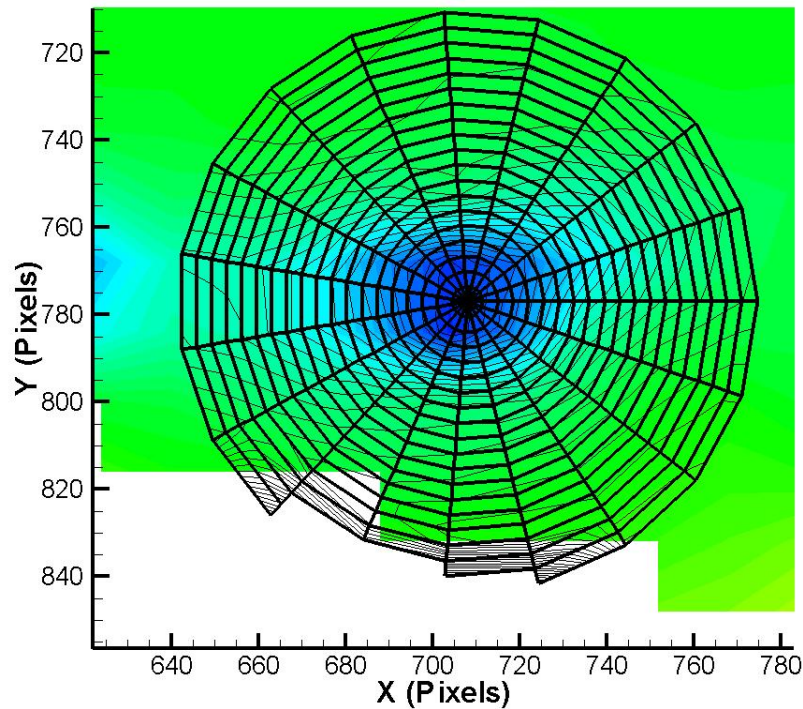


Figure 4.11: Grid used to find vortex radius

of the vortex, an equivalent vortex radius was obtained by averaging 20 radii obtained at different values of θ .

Vortices were compared at a similar location, 20% chord length downstream of the trailing edge, for close, mid, and far spacings at nominal and decreased loadings (see Table 4.2.1). There existed only a 2% difference when comparing the radii of the vortices at close, mid and far spacings for nominal and decreased loading. This seems to contradict the results obtained by Langford [5] since the size of the vortex did not change when spacing and consequently shock strength, was changed. However, the vortices being compared by Langford were mostly axisymmetric and the vortices being compared here are non-axisymmetric. The radii computed using the method described

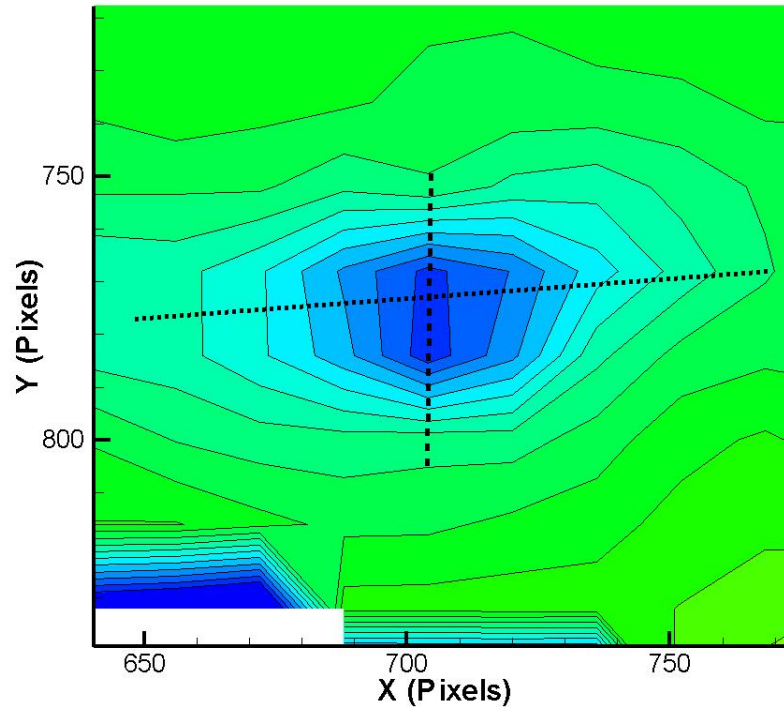


Figure 4.12: Image showing chordwise (parallel to flow) and pitchwise (perpendicular to flow) radius.

above averaged out the differences (see Fig. 4.12) between the chordwise radius (parallel to the flow) and pitchwise radius (perpendicular to the flow).

To more fully quantify the blockage that these vortices produce, the pitchwise radii were computed for the same vortices. There was a decrease in pitchwise radius of 19% from close to mid and a decrease in pitchwise radius of 19% from mid to far spacing at nominal loading. Vortices at decreased loading also experienced a decrease in pitchwise radius of 13% from mid to far. The vortex radius changed very little, 4% for mid spacing and 3% for far spacing, when compared between decreased and nominal loading (see Table 4.2.1). These measurements agree with Langford's findings that there exists a direct relationship between shock strength and passage blockage

due to the vortex. There is a decrease in the strength of the shock interacting with the deswirler trailing edge as deswirler/rotor spacing is increased from close to far resulting in a decrease of the shed vortex pitchwise radius. Pitchwise radius changed very little when deswirler/rotor spacing remained constant and loading was changed, a result of the shock strength remaining constant.

Table 4.1: Radius of vortices located 20% chord length downstream of deswirler

| Spacing | Loading | Radius (mm) | Pitchwise Radius (mm) |
|---------|-----------|-------------|-----------------------|
| close | nominal | 1.71 | 1.64 |
| mid | nominal | 1.80 | 1.33 |
| mid | decreased | 1.69 | 1.28 |
| far | nominal | 1.80 | 1.09 |
| far | decreased | 1.82 | 1.12 |

4.2.2 Vortex Strength

In order to quantitatively compare vortices within a blade period, generated at different spacings and loadings, circulation was computed. The circulation can be computed from the PIV data as either the line integral of the velocity or the area integral of the vorticity (see Eqn. 4.2).

$$\Gamma = \int \int \boldsymbol{\omega} \cdot \mathbf{n} \, dA = \oint \mathbf{u} \cdot d\mathbf{l} = \oint U dx + V dy \quad (4.2)$$

The circular area and integration path methods were both considered to find circulation. Both methods gave similar results with less than 1% difference. A non-circular integration path was used due to the complex vortical structures and the limited velocity data towards the bottom half of the vortices caused by the edge of the laser field (see Fig. 4.13). Raffel et al. [30] describes a

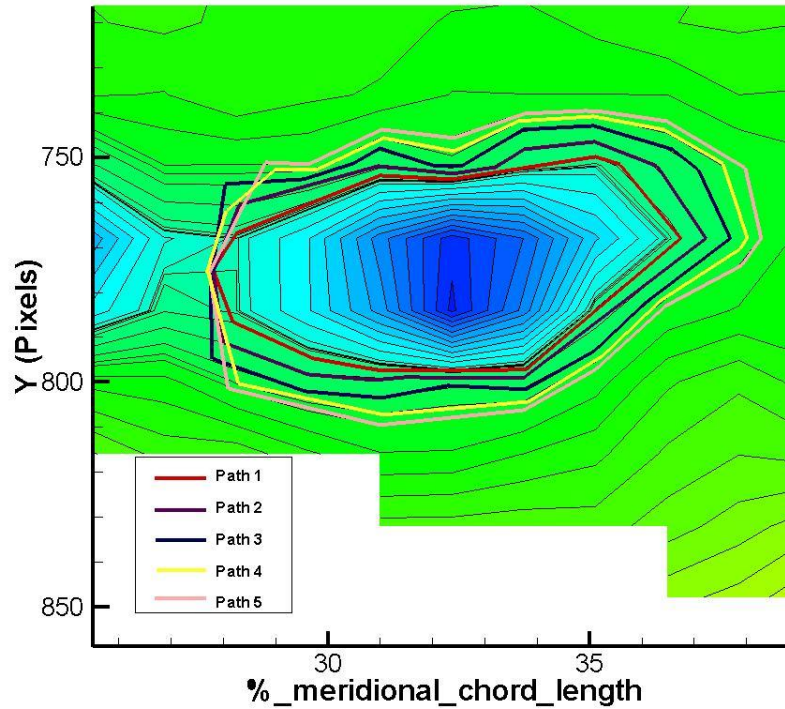


Figure 4.13: Integration paths for calculation of circulation.

method for obtaining circulation for non-circular paths. The ideal integration path would be defined by a dividing stream line which separates vortical structures. Since the circulation actually is an area-integral of vorticity, an integration along a constant vorticity contour near zero will generate a value close to the vortex's actual circulation. Given the path of integration, the evaluation of Eq. 4.2 was accomplished using the trapezoidal approximation.

The rankine vortex was used in the validation of a code written to calculate vortex strength. The rankine vortex model is an attempt to describe the velocity profile through vortices in real, viscous, fluids and can be mathematically modeled using eq. 4.3, where U_θ is tangential velocity, r is radius, r_c is the radius core and Ω is a constant (see Fig 4.14). Circulation of the rankine vortex can also be mathematically calculated using eq. 4.4. The method described above was used to

calculate the circulation of the rankine vortex at several radii which was then compared against the circulation calculated using eq. 4.4

$$U_{\theta} = \begin{cases} \Omega r & r < r_c \\ \Omega \frac{r_c^2}{r} & r \geq r_c \end{cases} \quad (4.3)$$

$$\Gamma = U_{\theta} 2\pi r \quad (4.4)$$

and was found to be within 0.7% of the actual circulation. Several non-circular integration paths were used in calculating vortex circulation (see Fig. 4.13). The circulation for each vortex was calculated several times and then averaged with the largest percent difference being 6%. The circulation of several vortices was calculated and then the velocities used in the calculations were adjusted to account for the largest change in circulation due to uncertainty of velocity. Using measurements taken at the vortices frame of reference, this was accomplished by adding the uncertainty of velocity to the positive velocities of the vortex and subtracting the uncertainty of velocity from the negative velocities of the vortex. This showed that the maximum uncertainty in the circulation calculation was 12% when incorporating uncertainty for velocity. Changes in circulation less than 12% were considered to be insignificant.

Section 4.1, Qualitative Observation, showed that several vortices are shed in one blade period. Vorticity contours suggested that the three vortices shed in a blade period may differ in strength. Analysis of the circulation of these vortices showed that there existed two stronger vortices followed by a weaker vortex that were shed in a blade period. For far and mid spacing at

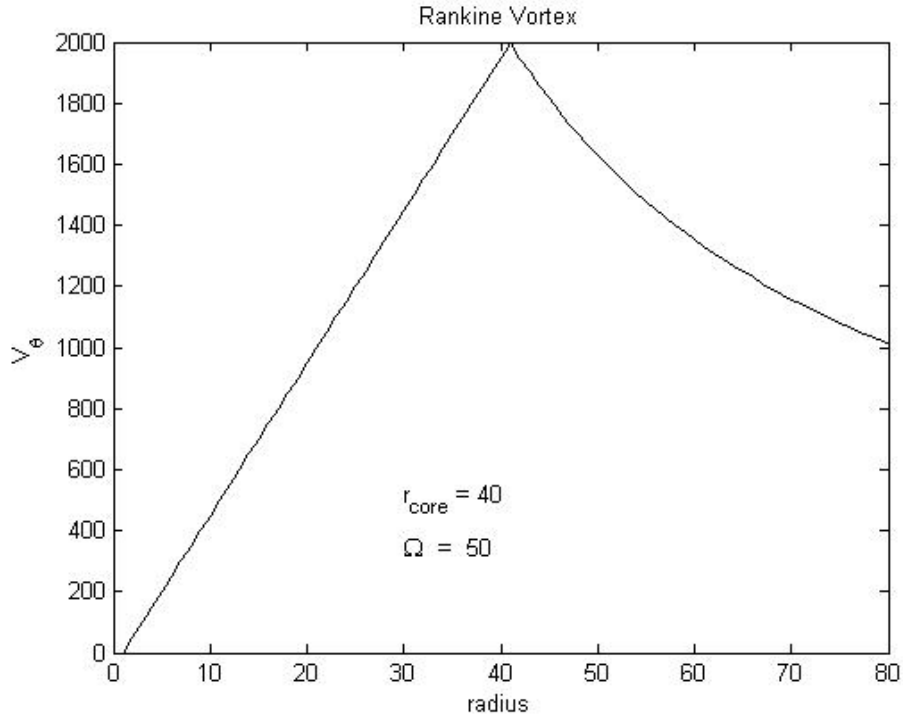


Figure 4.14: Tangential velocity of a Rankine Vortex.

Table 4.2: Circulation of vortices located 20% chord length downstream of deswirler trailing edge

| Spacing | Loading | Circulation $\frac{m^2}{s}$ |
|---------|-----------|-----------------------------|
| close | nominal | 0.705 |
| close | decreased | — |
| mid | nominal | 0.752 |
| mid | decreased | 0.568 |
| far | nominal | 0.580 |
| far | decreased | 0.462 |

nominal loading there was a difference of 20% and 18% between the stronger (**A**, **B**) and weaker vortices (**C**) and an insignificant difference of 3% between the two stronger vortices.

A comparison of the vortex strength was conducted to investigate how loading effected shed vortices. Vortex strength was compared for a stronger vortex at 20% chord downstream for

all three spacings at nominal loading (see Fig. 4.15) and for mid and far spacings at decreased loading (see Fig. 4.16). Results of the comparison are presented in Table 4.2.2. The data shows that there was a decrease in vortex strength by 25% for mid spacing and 20% for far spacing when loading was changed from nominal to decreased. These results show stator loading affects the strength of shed vortices from the stator trailing edge.

A comparison of the vortex strength was conducted to investigate how spacing affected shed vortices. A comparison of a vortex at 20% chord for close and mid stator/rotor spacings at nominal loading showed no significant change in circulation. There was a significant change between vortices at a common location for mid and far spacing of 23% for nominal loading and 19% for decreased loading. This supports conclusions of Gorrell et al. [3] and Langford et. al. [5] that vortex strength varies with shock strength.

The weaker vortices were also compared using mid and far spacings at nominal and decreased loadings. PIV results did not allow for a study at a specific distance downstream but the results of calculated circulation at different distances downstream of the trailing edge are shown in Fig. 4.17. It was observed that the weaker vortices shed at far and mid spacing at the same loading fall along a similar line. This is true at both nominal and decreased loading. This shows that the shock strength does not affect the strength of the weaker vortex. Since this vortex has the same strength at both mid and far spacings and changes with loading, the shock is not the direct cause of shedding but instead the vortex may be a naturally shed vortex differing in strength due to a difference in loading.

Three vortices were shed for each blade period in both far and mid spacings. Two of these vortices were labeled stronger, having a higher circulation value. The other was labeled weaker due to a decrease in circulation of $\sim 20\%$. The stronger vortices decreased in strength as spacing

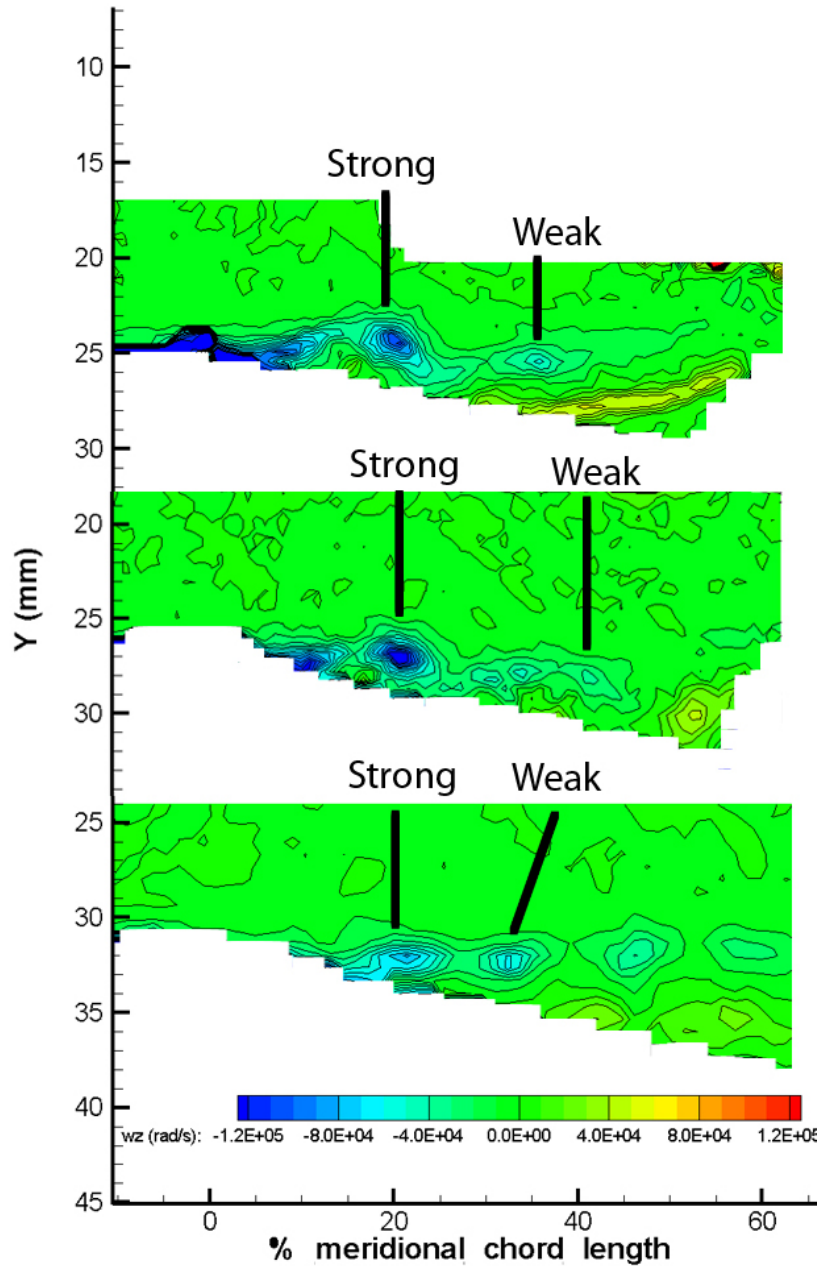


Figure 4.15: Vortices at 20% meridional chord length for close, mid, and far spacings at nominal loading.

between deswirler and rotor was increased from mid to far spacing. These stronger vortices are therefore a result of the interaction of the shock with the deswirler. As the shock impacting the trailing edge of the deswirler became weaker (increased spacing), vortex strength decreased. The

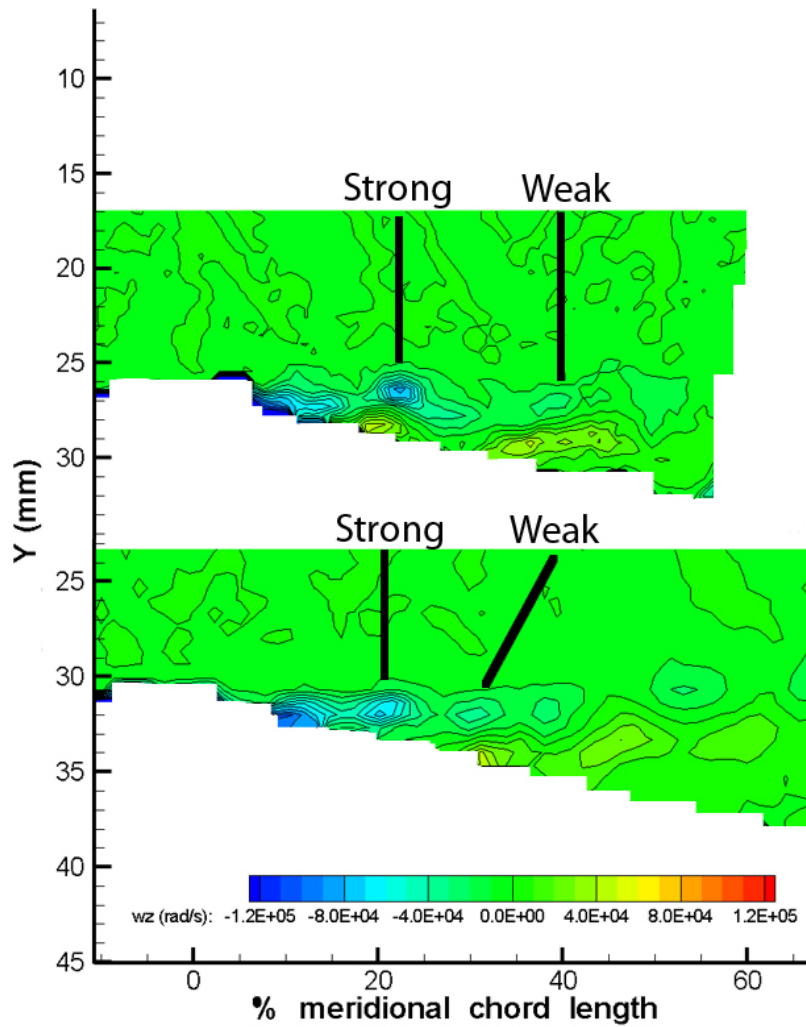


Figure 4.16: Vortices at 20% meridional chord length for mid, and far spacings (top to bottom) at decreased loading.

weaker vortices strength changed little with increased shock strength but changed with loading. The weaker vortices are not a direct result of the shock impacting the trailing edge. However, since the weaker vortices strength changed with loading it is believed that these shed vortices are a result of natural shedding.

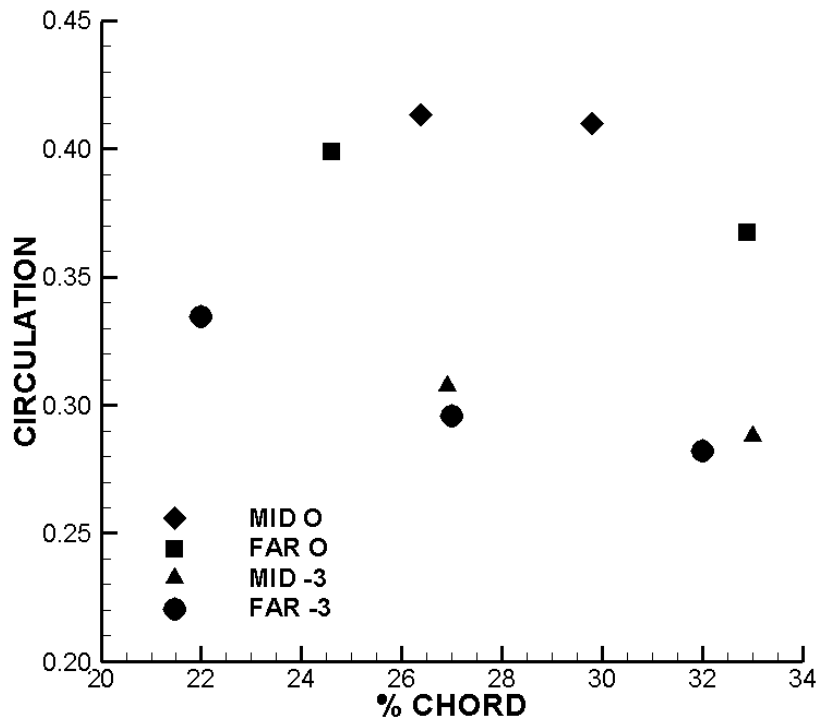


Figure 4.17: Circulation of weaker vortices at mid and far spacings (top and bottom) for nominal and decreased loadings.

4.3 Design Implications

This research shows a clear relationship between the loading of an upstream stator, the axial gap between a stator and transonic rotor, and the vortices generated from the interaction of the stator trailing edge with a rotor bow shock. A stator with higher loading will shed stronger vortices than a stator with lower loading. Crocco's theorem suggests the stronger vortices would generate increased entropy. This research quantifies the magnitude of change in circulation possible when nominal changes to stator loading are made. Furthermore, as has been demonstrated by List [39] and Nolan [11], the path vortices and wakes take through a rotor passage also affect the pressure ratio and efficiency of the rotor. The magnitude of loss generated as a vortex convects through

a rotor passage will also be affected by the strength of the vortex entering the rotor. Previous research showed vortex size increased as spacing decreased from far to mid spacing. These BRI results show the same trend. The magnitude of the pitchwise radius has a direct effect on blockage. A larger vortex will cause streamlines to deviate away from axial to go around the vortex and this process generates additional loss. It was also determined that while vortex size did not change with loading, the circulation of the vortices changed significantly. The strength of a vortex did change with loading for the same shock strength. The change in loading associated with reducing stator loss coefficient by $\sim 20\%$ decreased the strength of the shed vortex by $\sim 20\%$. With the quantitative understanding made possible from this research, improved design and performance prediction of highly loaded transonic fan and compressor stages is possible by taking into account the size and strength of vortices shed due to blade-row interactions.

CHAPTER 5. CONCLUSION

Transonic blade row interactions generate a complex unsteady flow field that affects the aerodynamic performance of gas turbine engine fans and compressors. The BRI rig is a high-speed, highly loaded compressor used to simulate the interactions between a transonic rotor and a stator. PIV data was obtained at the AFRL CARL facilities capturing the blade-row shock interaction for two loadings and three spacings. This research analyzed PIV measurements of the AFRL BRI rig. Analysis of the PIV images was presented for close, mid and far spacing at nominal and decreased loadings. The objective of the research was to use vortex size, strength and location of vortex with respect to shock location to analyze how spacing and loading effect blade row interactions. This was the first time the effects of spacing and loading on blade row interactions had been studied using realistic geometries in a transonic compressor. Several new and important conclusions regarding transonic blade-row interactions can be made.

Vortex size decreased by 19% in the pitchwise direction as spacing was increased from close to mid and from mid to far at nominal loading. There was also a decrease in vortex size of 13% from mid to far spacing at decreased loading. There was no significant change in vortex size when vortices were compared at similar spacing but different loadings. Therefore, the vortices generated from the rotor bow shock at close spacing, corresponding to a stronger shock strength, would produce more blockage, due to a larger radius, than vortices shed from interaction with a weaker bow shock (increased axial spacing).

It was found that three vortices were shed for each blade period. These vortices differed in strength with two being considered stronger vortices and one weaker (a decrease of $\sim 18\%$ in strength). Using flow visualization images, streamlines and vorticity contours the location of the vortex could be determined with respect to shock location. The strong vortices were found to shed close to the time the shock impacted the trailing edge and while the shock propagated up the trailing edge of the deswirlor. The weaker vortex was found to form after a shock had propagated up the deswirlor and before another shock had interacted with the trailing edge. The stronger vortex strength was related to the axial spacing and thus shock strength with a decrease in circulation of 23% for nominal loading and 19% for decreased loading from mid to far spacing. Loading also affected the strength of these stronger vortices with a decrease in strength by 25% for mid spacing and 20% for far spacing when compressor configurations were changed from nominal to decreased loading. The strength of the weaker vortices was not greatly affected by changes in spacing but a decrease of 20% existed when loading was changed from nominal to decreased loading.

The research showed that stator loading as well as axial gap have a significant effect on the strength and size of vortices shed due to transonic blade-row interactions. Decreasing the axial spacing results in an increase of shock strength interacting with the stator trailing edge producing a stronger and larger vortex. A decrease in loading on the stator will result in a decrease in strength of the vortex being shed. For the BRI rig reducing the stator loss coefficient by $\sim 20\%$ reduced the strength of a shed vortex by $\sim 20\%$. However, changing the loading on the deswirlor had no effect on vortex size. Understanding and accounting for such unsteady flow physics will allow designers to better design and predict the performance of transonic fan and compressor stages at both design and off-design operating conditions.

Future work with the analysis of the BRI rig could include a study using CFD. Time-accurate CFD codes are now used to simulate compressor operation and investigate complex unsteady-flow phenomena. The experimental results presented could be used for validating CFD models. It is recommended that accurate CFD results be used to investigate vortex-shock interactions, shock unsteadiness, wake-shock interaction, and the suction-side of the deswirler. The PIV results presented were not able to capture the flow field on the suction side of the deswirler. CFD results could be used to verify if separation on the suction-side occurs and how this separation contributes to the shed vortices within the wake. PIV data was only taken for a nominal and decreased loading. Different configurations should also be studied including additional swirler staggers that would increase the loading on the deswirler. It is recommended that CFD simulations be performed for a swirler stagger angle of $+ 1.5$ degrees at all three spacings and a $- 3$ degrees for close spacing. These results could be compared with performance data taken with the BRI rig. CFD simulations should also be used to determine exact blade loading.

Effects of spacing and stator loading on the passage of wake through rotor should be investigated. The effects of the passage of a stronger vortex through the rotor passage should be investigated as well as the path vortices take through the rotor passage. More time steps should be investigated to allow for more complete study of vortex shedding. More time steps would be used to show exactly when and why vortex pairs are shed and why they differ in strength. PIV results were limited to a study of a single plane of data at 50% span. CFD results would allow for study of 3D interactions and unsteady flow caused at the hub and tip.

REFERENCES

- [1] Gorrell, S. E., Copenhaver, W. W., and Chriss, R. M., 2001. “Upstream Wake Influences on the Measured Performance of a Transonic Compressor Stage.” *AIAA Journal of Propulsion and Power*, **17**, pp. 43–48. vi, viii, 2, 10, 17
- [2] Gorrell, S. E., Okiishi, T. H., and Copenhaver, W. W., 2003. “Stator-Rotor Interactions in a Transonic Compressor, Part 1: Effect of Blade-Row Spacing on Performance.” *ASME Journal of Turbomachinery*, **125**, pp. 328–335. viii, 2, 11, 12
- [3] Gorrell, S. E., Car, D., Puterbaugh, S. L., Estevadeordal, J., and Okiishi, T. H., 2006. “An Investigation of Wake-Shock Interactions with Digital Particle Image Velocimetry and Time-Accurate Computational Fluid Dynamics.” *ASME Journal of Turbomachinery*, **128**(4), pp. 616–626. viii, 2, 11, 12, 13, 14, 15, 44, 53, 60
- [4] Gorrell, S. E., Okiishi, T. H., and Copenhaver, W. W., 2003. “Stator-Rotor Interactions in a Transonic Compressor, Part 2: Description of a Loss Producing Mechanism.” *ASME Journal of Turbomachinery*, **125**, pp. 336–345. viii, 2, 11, 16, 20, 39
- [5] Langford, M. D., Breeze-Stringfellow, A., Guillot, S. A., Solomon, W., Ng, W., and Estevadeordal, J., 2007. “Experimental Investigation of the Effects of a Moving Shock Wave on Compressor Stator Flow.” *ASME Journal of Turbomachinery*, **129**(1), pp. 127–135. viii, 2, 23, 24, 49, 53, 54, 60
- [6] Turner, M. G., Gorrell, S. E., and Car, D., 2005. “Radial Migration of Shed Vortices in a Transonic Rotor Following a Wake Generator: A Comparison Between Time Accurate and Average Passage Approach.” ASME Paper GT2005-68776. 2, 12
- [7] van de Wall, A., Breeze-Stringfellow, A., and Dailey, L., 2006. “Computational Investigation of Unsteady Flow Mechanisms in Compressors with Embedded Supersonic Rotors.” ASME Paper GT2006-90633. 2, 23
- [8] Estevadeordal, J., Gorrell, S., and Copenhaver, W., January-February 2007. “PIV Study of Wake-Rotor Phenomena in a Transonic Compressor Under Various Operating Conditions.” *AIAA Journal of Propulsion and Power*, **23**, pp. 235–242. 2, 12, 28, 35, 36, 39, 44
- [9] Van Zante, D., Chen, J., Hathaway, D., and Chriss, R., 2008. “The Influence of Compressor Blade Row Interaction Modeling on Performance Estimates from Time-Accurate, Multistage, Navier-Stokes Simulations.” *ASME Journal of Turbomachinery*, **130**(1), January. 2
- [10] List, M. G., Gorrell, S. E., and Turner, M. G., 2008. “Investigation of Loss Generation in an Embedded Transonic Fan Stage at Several Gaps Using High-fidelity, Time-accurate CFD.” ASME Paper GT2008-51220. 2, 21, 22

- [11] Nolan, S. P. R., Botros, B. B., Tan, C. S., Adamczyk, J. J., Greitzer, E. M., and Gorrell, S. E., 2009. “Effects of Upstream Wake Phasing on Transonic Axial Compressor Performance.” *ASME Paper GT2009-59596*. 2, 63
- [12] Adamczyk, J. J., 2000. “Aerodynamic Analysis of Multistage Turbomachinery Flows in Support of Aerodynamic Design.” *ASME Journal of Turbomachinery*, **122**, pp. 189–217. 7
- [13] Hathaway, M. D., Gertz, J. B., Epstein, A. H., and Strazisar, A. J., 1986. “Rotor Wake Characteristics of a Transonic Axial-Flow Fan.” *AIAA Journal*, **24**(11), p. 1802. 7
- [14] Kotidis, P. A., and Epstein, A. H., 1991. “Unsteady Radial Transport in a Transonic Compressor Stage.” *ASME Journal of Turbomachinery*, **113**, pp. 207–218. 7
- [15] Van de Wall, A. G., Kadambi, J. R., Boyle, R. J., and Adamczyk, J. J., 1996. “The Transport of Vortices Through a Turbine Cascade.” *ASME Journal of Turbomachinery*, **118**(4), pp. 654–662. 7
- [16] Smith, L. H., 1966. “Wake Dispersion in Turbomachines.” *ASME Journal of Basic Engineering*(3), pp. 668–690. 8, 11
- [17] Mikolajczak, A. A., 1977. “The Practical Importance of Unsteady Flow.” *Unsteady Phenomena in Turbomachinery*(AGARD CP-144). 8
- [18] Ottavy, X., Trebinjac, I., and Voullarmet, A., 2001. “Analysis of the Interrow Flow Field Within a Transonic Axial Compressor: Part 1 - Experimental Investigation.” *ASME Journal of Turbomachinery*, **123**, pp. 49–56. 8
- [19] Sanders, A., and Fleeter, S., 2000. “Experimental Investigation of Rotor-Inlet Guide Vane Interactions in Transonic Axial-Flow Compressor.” *AIAA Journal of Propulsion and Power*, **16**, pp. 421–430. 8
- [20] Creason, T., and Baghdadi, S., 1988. Design and Test of a Low Aspect Ratio Fan Stage AIAA Paper 88-2816. 10
- [21] Probasco, D. P., Wolff, J. M., Copenhaver, W. W., and Chriss, R., 1998. “Axial Spacing Effects in a Transonic Compressor on the Upstream Vane Loading.” *AIAA Paper no. 98-3431*. 10
- [22] Chriss, R. M., Copenhaver, W. W., and Gorrell, S. E., 1999. “The Effects of Blade-Row Spacing on the Flow Capacity of a Transonic Rotor.” *ASME Paper 99-GT-209*. 11
- [23] Estevadeordal, J., Gogineni, S., Goss, L., Copenhaver, W., and Gorrell, S., 2002. “Study of Wake-Blade Interactions in a Transonic Compressor Using Flow Visualization and DPIV.” *ASME Journal of Fluids Engineering*, **124**, pp. 166–175. 12
- [24] Estevadeordal, J., Gogineni, S., Goss, L., Copenhaver, W., and Gorrell, S., 2001. “DPIV Study of Wake-Rotor Synchronization in a Transonic Compressor.” AIAA Paper 01-3095. 12
- [25] Estevadeordal, J., Gorrell, S., Gebbie, D., and Puterbaugh, S., 2007. “PIV Study of Blade-Row Interactions in a Transonic Compressor.” AIAA Paper 2007-5017. 20, 28, 39

- [26] Estevadeordal, J., Gorrell, S., and Puterbaugh, S., 2008. “PIV Measurements of Blade-Row Interactions in a Transonic Compressor for Various Operating Conditions.” AIAA Paper 2008-4700. 20, 28, 40
- [27] List, M. G., Gorrell, S. E., Turner, M. G., and Nimersheim, J. A., 2007. “High-fidelity Modeling of Blade Row Interaction in a Transonic Compressor.” AIAA Paper 2007-5045. 21
- [28] Estevadeordal, J., Langford, M. D., Breeae-Stringfellow, A., Guillot, S. A., and Ng, W. F., 2007. “PIV Investigation of the Flow Field in a Transonic Compressor Cascade with a Moving Shock Wave.” AIAA Paper 2007-5064. 23
- [29] Kerrebrock, J. L., 1977. *Aircraft Engines and Gas Turbines*. MIT, Cambridge, MA. 23
- [30] Raffel, M., Willert, C. E., and Kompenhans, J., 1998. *Particle Image Velocimetry*. Springer. 28, 29, 35, 43, 56
- [31] McCray, T. W., Estevadeordal, J., and Puterbaugh, S. L., 2005. “Parallel Computing for Linux Clusters Application to Particle Image Velocimetry.” AIAA Paper 2005-1385. 29
- [32] Stearns, S. D., and Hush, D., 1990. *Digital Signal Analysis*., second ed. Prentice Hall. 29
- [33] Westerweel, J., 1997. “The effect of a discrete window offset on the accuracy of cross-correlation analysis of PIV recordings.” *Experiments in Fluids*, **23**, pp. 20–28. 32
- [34] Estevadeordal, J., and Kleis, S. J., 1999. “High-resolution measurements of two-dimensional instabilities and turbulence transition in plane mixing layers.” *Experiments in Fluids*, **27**(4), pp. 378–390. 35, 36
- [35] Coleman, H. W., and Steele, W. G., 1989. *Experimentation and Uncertainty Analysis for Engineers*. John Wiley and Sons, New York. 35, 36
- [36] Inoue, L. Y. T., and Berry, D. A. and Parmigiani, G., 2005. “Relationship between Bayesian and Frequentist Sample Size Determination.” *The American Statistician*. 35
- [37] Estevadeordal, J., Gorrell, S., and Copenhaver, W., 2004. “DPIV Study of Wake-Rotor Interactions in a Transonic Compressor Under Various Operating Conditions.” *11th International Symposium on Flow Visualization* August 2004, Notre Dame, Indiana. 36
- [38] www.tecplot.com Tecplot 360, A complete CFD visualization tool that helps analyze, explore and understand complex simulation data. 44
- [39] List, M. G., Gorrell, S. E., and Turner, M. G., 2010. “Investigation of Loss Generation in an Embedded Transonic Fan Stage at Several Gaps Using High-fidelity, Time-accurate Computational Fluid Dynamics.” *ASME Journal of Turbomachinery*, **132**(011014), January. 63

APPENDIX A. RUNNING PPIV ON MARYLOU4

A.1 Introduction

Before you start running any programs on Marylou4 it's a good idea to actually understand what you are doing. Below are some typical questions that a new user might have.

A.1.1 PIV

Particle Image Velocimetry (PIV) is an optical method used to measure kinematic properties of a fluid. The fluid is seeded with submicron size particles which closely follow the flow field. A laser sheet is delivered to the area of interest which acts as a flash for the camera. The particles reflect the light from the laser, and the camera is able to take pictures of the particles. Using a pair of images the displacement of the particles can be determined through statistical analysis. From the displacement of the seed particles and the time between each image pair the velocity field is obtained.

A.1.2 PPIV

PPIV or Parrallel PIV is a code written by Tom McCray, Fourth Innovative Scientific Solutions, Inc., that allows for the vector calculation to be performed on multiple processors. This greatly decreases the time needed to process data for large sets of image pairs.

A.1.3 Marylou4

Marylou4 is a Supercomputer at BYU's Fulton Supercomputing Laboratory (FSL). Marylou4 is a Dell 1955 Linux cluster. There are 630 nodes, each with two Intel 2.6GHz Xeon EM64T dual-core processors and 8 GB of fully-buffered RAM. 210 of the nodes are connected with an Infiniband switch for improved MPI performance, as well as standard Ethernet. All 630 nodes are connected with Gigabit Ethernet.

This information is written for the new user. This document contains a brief explanation of BYU's Supercomputer Marylou4, where to find needed information on the Supercomputer, examples and explanation on how to submit and run PPIV and other useful information. It is intended to establish a starting point for someone who has never had any experience with the supercomputer, PIV and parallel computing.

A.2 BYU's Supercomputer Marylou4

The best place to start learning about Marylou4 would be the website dedicated to BYU's supercomputer (<http://marylou.byu.edu>). For a quick overview open Resources under Main Menu and then Marylou4. For more information read Marylou4 FAQ found under quick links on the main page.

A.2.1 Accessing Marylou4

The first step you need to take in order to begin your journey into supercomputing will be setting up an account. All you need to do is follow the steps in Getting an Account found under the Main Menu section of the Website. While you are waiting for your account to be activated (this can take up to a couple days) you'll need to be learning a few things.

When you started the process of getting an account you were informed that before gaining access to the supercomputer you would need the following:

1. A secure shell client (SSH, various versions available for free)
2. A basic knowledge of UNIX (e.g. how to login, edit files, use ssh, scp).
3. A legitimate need for supercomputing resources.
4. Students need approval from a faculty mentor (i.e., the faculty member with whom you are doing your research) before your account is created. Any problems with student accounts will be brought to the attention of the faculty mentor.

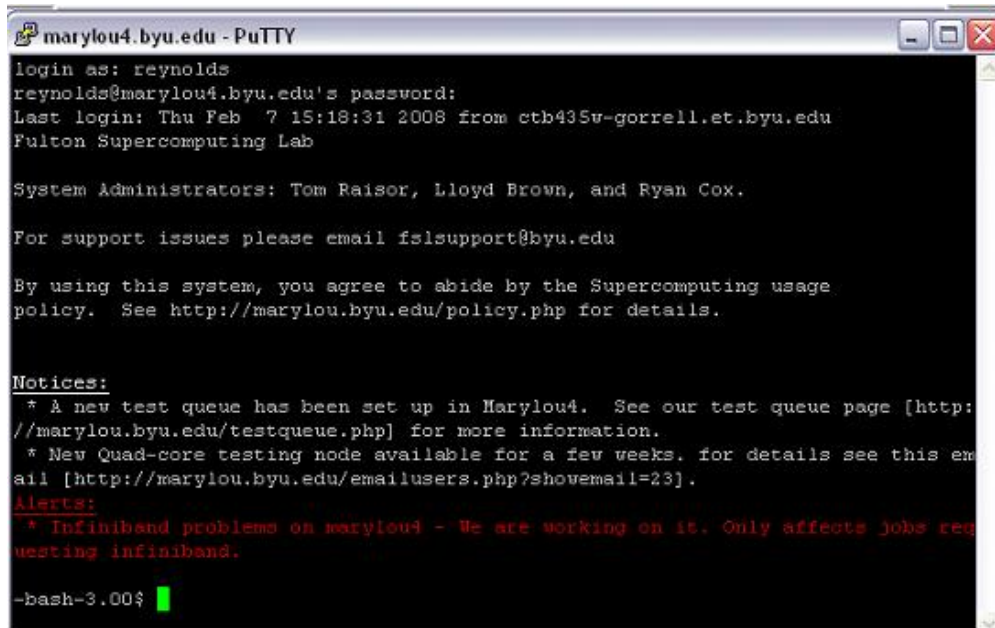
Numbers 3 and 4 probably didn't worry you too much but if you're a new user 1 and 2 may have given you a scare. The following sections will help establish a base and give direction so you can learn for yourself.

A.2.2 Secure Shell Client

Secure Shell or SSH is a network protocol that allows data to be exchanged over a secure channel between two computers. For that reason it is used in communicating from your home computer or any remote computer you decide to use and the supercomputer. SSH is used to log into a remote machine and execute commands. You will need to download SSH onto the computer you plan on using to submit jobs. A common SSH that you can download for a windows based machine is PuTTY. You can download PuTTY at www.putty.org. Also, the Caedm computers have SSH that you can use. There are several different SSH software's that are available. For convenience it is assumed that PuTTY is being used. When you use SSH to connect to marylou4 you will have to

put in the host name (Marylou4.byu.edu). You will then be asked for your username and password.

You are now logged into Marylou4 and should see a screen like that shown in Fig. A.1.



```
marylou4.byu.edu - PuTTY
login as: reynolds
reynolds@marylou4.byu.edu's password:
Last login: Thu Feb 7 15:18:31 2008 from ctb435v-gorrell.et.byu.edu
Fulton Supercomputing Lab

System Administrators: Tom Raisor, Lloyd Brown, and Ryan Cox.

For support issues please email fslsupport@byu.edu

By using this system, you agree to abide by the Supercomputing usage
policy. See http://marylou.byu.edu/policy.php for details.

Notices:
* A new test queue has been set up in Marylou4. See our test queue page [http:
//marylou.byu.edu/testqueue.php] for more information.
* New Quad-core testing node available for a few weeks. for details see this em
ail [http://marylou.byu.edu/emailusers.php?showemail=23].
Alerts:
* Infiniband problems on marylou4 - We are working on it. Only affects jobs req
uesting infiniband.

-bash-3.00$
```

Figure A.1: Marylou4's command prompt

A.2.3 Learning and Using Linux

Now that you have logged into Marylou4 you may not know what to do. You are probably accustomed to the Windows desktop with pictures and folder icons representing directories. Marylou4 doesn't give you the luxury of viewing your folders as an icon, but those folders (directories) are still there. In order to access these directories you will need to invest a little time in learning Linux

As already mention Marylou4 is a Linux cluster. To navigate through your directories you will need to learn the linux language. The window seen in figure 1 is the command prompt. This is where you will enter commands needed to create and submit jobs. The quickest way to learn linux

is to start exploring and to learn by doing. There are several books that will help you get started that you can check out from the library. Also, the internet has many useful tutorials and command lists. Don't be afraid to learn. If you get lost in all the computer jargon use the internet to search all the confusing terms. Below are a few commands that you can try at the command prompt.

Type: **ls** (that's LS but in lowercase) and then hit enter

The **ls** command will list the content of the directory that you are in

Type: **cd compute** and then hit enter

Use the **cd** command to change to another directory. This is like double clicking or opening a folder in Windows. By typing **cd compute** you just changed to the compute directory. Now type the **ls** command. This will list what you have in the compute directory. If this is your first time you probably don't have anything in your compute directory. Therefore, after typing the **ls** command nothing should show up.

Now use the **cd** command again but this time don't put anything after **cd**. This will bring you back to your home directory (the directory you were at when you started). Another useful command is the **mkdir**. This command is used to make another directory much like creating a folder in windows. Try this out by typing **mkdir PIV**. This will create a directory called PIV. In order to see the directory you just created you will need to use the **ls** command. You can remove this directory by using the **rm -r PIV**. Right now these are just commands that will get you started learning linux. Later we will be using these same commands to create a directory, change to that directory, and create and save a file within that directory. We will be using these commands and many more as we prepare to run PPIV on Marylou4.

There are hundreds of commands that you can learn to navigate your way through the command prompt. These are only a few to get you started. As you read through the rest of this

document you will learn a few more commands. However, to become comfortable with submitting jobs you will need to dedicate more time learning this new language.

A.2.4 Submitting a Job

The quickest way to learn how to submit a job on Marylou4 is by completing the tutorial on the supercomputer website. The tutorial is found in PBS Batch Tutorial under Quick Links. Included below are some helpful hints that could be useful as you complete the 9 steps of the tutorial

Step 1 (in the tutorial)

```
echo "1234 * 4321" | bc
```

help: to get the | after 4321" you press shift and \. The | is called a pipe the job identifier will look like this

```
"your number".fslsched.et.byu.edu
```

Step 5: Create a shell script (in the tutorial)

In this portion of the tutorial you will be creating a shell script. A shell script is a program interpreted and executed by the shell, which is essentially a command line interpreter. So, think of a shell script as a list of commands that are run in sequence.

This tutorial advises you to use your preferred text editor. A text editor is just a simple program used for writing text much like notepad or wordpad in windows. There are several text editors supported by marylou4. Many people are comfortable with vi or vim however, nano is a fairly straight forward text editor that we will use for this tutorial. At the command prompt type **nano** and press enter. You have now opened the text editor and can follow the tutorial.

Once you have written your script you will need to save and close the text editor. In nano you will exit the program and it will then ask you if you want to save. To exit as shown at the bottom of the window use `^ X` where the `^` means Ctrl (press Ctrl-X). You will then be asked to save modified buffer type `Y`. You then will name the script by typing **pbsprimer** and then pressing enter.

After completing the tutorial read over PBS batch information found under Quick Links. Some of this information will be a little confusing but become familiar with it so you can refer to this information as you write the script to submit the PPIV job.

A.3 Shell Script

Now that you have completed the tutorial and have started learning the linux language you are ready to write the script used in submitting your PIV job to the supercomputer. Below is an example of a script used to submit PIV. This is just one of the many ways that it can be done. The numbering 1-13 has been placed in front of the script for convenience.

1. `#!/bin \bash`
2. `#PBS -l nodes=1:ppn=3,walltime=00:20:00`
3. `#PBS -N PPIV`
4. `#PBS -m abe`
5. `#PBS -M 'your email'@byu.net`
6. `PROG=\fslhome\reynolds\bin\ppivexe`
7. `PROGARGS="piv\settings\parameters1.txt"`

8. `mpie=\opt\mpiexec\bin\mpiexec`
9. `SCRATCH_DIR=\fslhome\reynolds\compute`
10. `cd $SCRATCH_DIR`
11. `cp $HOME/piv/settings/parameters1.txt $SCRATCH_DIR`
12. `cp $PROG $SCRATCH_DIR`
13. `$mpie ppivexe "parameters1.txt"`

Lines 1-5 should look familiar since you did these in the tutorial. In line 2 the `-l` after `#PBS` is a lower case L

Lines 6-9 are defining variables that will later be used. These variables will be explained in the section Parallel PIV Setup.

Line 10 changes the directory that the script will be run in to the Scratch Directory or the compute directory (see line 9). All jobs are run from the compute directory. This is done for the following reasons: The compute folder is faster than the home directory, the compute folder is available from all Marylou4 nodes, and mainly because programs can NOT be run directly from the home directory.

Line 11 and 12 The command `cp` is used to copy files and directories that are needed to run the piv executable to the compute directory.

Line 13 This uses mpiexec to run the PPIV executable. Mpiexec is program used to initialize a parallel job from within a PBS batch or interactive environment. The FSL strongly encourages the use of mpiexec over mpirun. See PBS Batch information under Quick Links for more information.

A.4 Parallel PIV Setup

In order to run the PPIV executable you will need to create two configuration files. These files will be used by the executable to find the information it needs.

A.4.1 Parameters

The first file contains the PIV parameters. The specific filenames and directories used in this document are only suggestions but they are consistent with the example code. The files can have any name as long as they are valid filenames for the operating system and are less than 512 characters in length. The following paragraphs describe the format for each file.

PIV Parameters `fslhome/username/piv/settings/parameters.txt`

The above line requires that you create directories. Under your home directory, the directory you start at when you first log in, you will need to create the `piv` directory. Refer to the section *Learning and Using Linux*, for a review of how to create a directory. Within the `piv` directory you will create another directory called `settings`. It is within the `settings` directory that you will use `nano` to create a text document with following information (see Fig. A.2).

A.4.2 Images

PIV Image Pair List `/fslhome/username/piv/settings/images.txt`

Each line in the image pair list file contains the full path to a PIV image (see Fig. A.3). The first line contains the full path to Image Pair 1, Image 1. The second line contains the full path to Image Pair 1, Image 2. The third line contains the full path to Image Pair 2, Image 1, and so on. The filenames must be valid filenames for the operating system and less than 512 characters in length.

| Line | Description | Example |
|------|--|--|
| 1 | Full path to image pair list | /fs/home/username/piv/settings/images.txt |
| 2 | Output directory (full path) | /home/user/piv/data/results |
| 3 | Grid file (full path) | "none" if no grid file is used /home/user/piv/data/grid.csv |
| 4 | Output file type | 0=dpiv, 1=tecplot |
| 5 | 1 st iteration cell size | 128 |
| 6 | 1 st iteration overlap (0-99) | 75 |
| 7 | 1 st iteration correlation correction (0= disabled, 1=enabled) | 1 |
| 8 | 1 st iteration correlation correction overlap (0-99) | 75 |
| 9 | 1 st iteration vector calculation option (0=centroid) | 0 |
| 10 | 1 st iteration zero padding (0=disabled, 1=enabled) | 1 |
| 11 | 1 st iteration vector region (2, 4, 8 or 16) | 4 |
| 12 | 1 st iteration particle radius | 2 |
| 13 | 2 nd iteration cell size (0=no iteration) | 64 |
| 14 | 2 nd iteration overlap | 75 |
| 15 | 2 nd iteration correlation correction | 1 |
| 16 | 2 nd iteration correlation correction overlap | 75 |
| 17 | 2 nd iteration vector calculation option | 0 |
| 18 | 2 nd iteration zero padding | 1 |
| 19 | 2 nd iteration vector region | 4 |
| 20 | 2 nd iteration particle radius | 2 |
| 21 | 3 rd iteration cell size (0=no iteration) | 32 |
| 22 | 3 rd iteration overlap | 75 |
| 23 | 3 rd iteration correlation correction | 1 |
| 24 | 3 rd iteration correlation correction overlap | 75 |
| 25 | 3 rd iteration vector calculation option | 0 |
| 26 | 3 rd iteration zero padding | 1 |
| 27 | 3 rd iteration vector region | 4 |
| 28 | 3 rd iteration particle radius | 2 |
| 29 | 4 th iteration cell size (0=no iteration) | 0 |
| 30 | 4 th iteration overlap | 75 |
| 31 | 4 th iteration correlation correction | 1 |
| 32 | 4 th iteration correlation correction overlap | 75 |
| 33 | 4 th iteration vector calculation option | 0 |
| 34 | 4 th iteration zero padding | 1 |
| 35 | 4 th iteration vector region | 2 |
| 36 | 4 th iteration particle radius | 2 |

Figure A.2: Description of Parameters file for running PPIV.

At first you may want to only use 1 image pair to test the script and executable. When you have a working script and need to process more images you may want to use the following.

Creating the image file manually can be very time consuming. The following linux command can do the job easily. If your image pairs are sequentially numbered and are stored in the same directory, like the previous table, use the following command to generate your image list file.

```
% find /home/user/piv/data/*.tif | /home/user/piv/settings/images.txt
```

| Line | Description | Example |
|------|------------------------------------|--|
| 1 | Full Path to Image Pair 1, Image 1 | /fs/home/username/piv/data/image_001.tif |
| 2 | Full Path to Image Pair 1, Image 2 | /fs/home/username/piv/data/image_002.tif |
| 3 | Full Path to Image Pair 2, Image 1 | /fs/home/username/piv/data/image_003.tif |
| 4 | Full Path to Image Pair 2, Image 2 | /fs/home/username/piv/data/image_004.tif |
| 5 | Full Path to Image Pair 3, Image 1 | /fs/home/username/piv/data/image_005.tif |
| 6 | Full Path to Image Pair 3, Image 2 | /fs/home/username/piv/data/image_006.tif |
| 7 | Full Path to Image Pair 4, Image 1 | /fs/home/username/piv/data/image_007.tif |
| 8 | Full Path to Image Pair 4, Image 2 | /fs/home/username/piv/data/image_008.tif |

Figure A.3: Description of Image list file for running PPIV.

The find portion of the command generates the list of full path names. The ζ portion of the command places the output of find into /home/user/piv/settings/images.txt.

To copy Images from your computer onto the Supercomputer see the section on Transferring Files

Example PIV Parameter File:

```

/home/user/piv/settings/images.txt
/home/user/piv/data/results
none
0
128
75
1
75
0
1
4
2
64
75
1
75
0
1
4
2
32
75
1
75

```


0
1
4
2
0
75
1
75
0
1
2
2

Example PIV Image List File (50 images, 25 image pairs):

/home/user/piv/data/image_001.tif
/home/user/piv/data/image_002.tif
/home/user/piv/data/image_003.tif
/home/user/piv/data/image_004.tif
/home/user/piv/data/image_005.tif
/home/user/piv/data/image_006.tif
/home/user/piv/data/image_007.tif
/home/user/piv/data/image_008.tif
/home/user/piv/data/image_009.tif
/home/user/piv/data/image_010.tif
/home/user/piv/data/image_011.tif
/home/user/piv/data/image_012.tif
/home/user/piv/data/image_013.tif
/home/user/piv/data/image_014.tif
/home/user/piv/data/image_015.tif
/home/user/piv/data/image_016.tif
/home/user/piv/data/image_017.tif
/home/user/piv/data/image_018.tif
/home/user/piv/data/image_019.tif
/home/user/piv/data/image_020.tif
/home/user/piv/data/image_021.tif
/home/user/piv/data/image_022.tif
/home/user/piv/data/image_023.tif
/home/user/piv/data/image_024.tif
/home/user/piv/data/image_025.tif
/home/user/piv/data/image_026.tif
/home/user/piv/data/image_027.tif
/home/user/piv/data/image_028.tif
/home/user/piv/data/image_029.tif
/home/user/piv/data/image_030.tif

/home/user/piv/data/image_031.tif
/home/user/piv/data/image_032.tif
/home/user/piv/data/image_033.tif
/home/user/piv/data/image_034.tif
/home/user/piv/data/image_035.tif
/home/user/piv/data/image_036.tif
/home/user/piv/data/image_037.tif
/home/user/piv/data/image_038.tif
/home/user/piv/data/image_039.tif
/home/user/piv/data/image_040.tif
/home/user/piv/data/image_041.tif
/home/user/piv/data/image_042.tif
/home/user/piv/data/image_043.tif
/home/user/piv/data/image_044.tif
/home/user/piv/data/image_045.tif
/home/user/piv/data/image_046.tif
/home/user/piv/data/image_047.tif
/home/user/piv/data/image_048.tif
/home/user/piv/data/image_049.tif
/home/user/piv/data/image_050.tif

A.5 Transferring Files

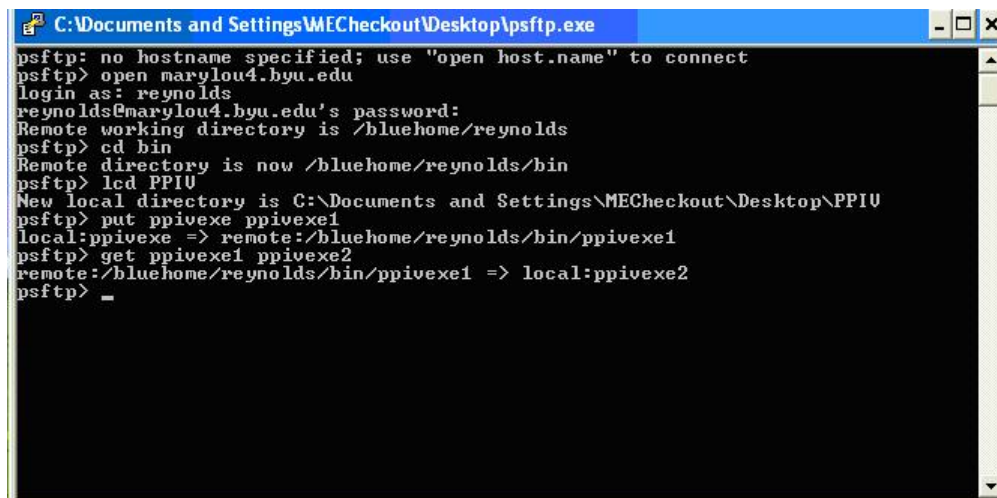
To be able to run PPIV you will have to copy the executable and other needed files, such as the image files, onto the Supercomputer. This is done using SFTP (Secure File Transfer Protocol). Since we are using PuTTY SSH we will also use the PuTTY version of SFTP called PSFTP. This can be downloaded from www.putty.org. Many explanations on how to use PSFTP can be found on the Internet (see <http://the.earth.li/~sgtatham/putty/0.52/html/Chapter6.html> for an in depth explanation).

Here is a brief explanation on how to transfer file using the PuTTY FTP function to and from Marylou4 Perform these steps to transfer files between Marylou4 and your computer.

1. Download psftp from www.PuTTY.org
2. Start the psftp session by Double click on the file named Psftp.exe
3. Open a connection to Marylou4. type *open Marylou4.byu.edu*

4. Give needed information such as login name and password
5. Change to the appropriate directory on Marylou4 (for example, cd /bin).
6. Change directories to the appropriate directory on your computer (for example, lcd /PPIV).
7. Use put to transfer files to Marylou4 and get to retrieve files from Marylou4. put file_name new_file_name or get file_name new_file_name
8. End the ftp session by entering quit.

An example of these commands can be seen in Fig. A.4.



```
C:\Documents and Settings\MECheckout\Desktop\psftp.exe
psftp: no hostname specified; use "open host.name" to connect
psftp> open marylou4.byu.edu
login as: reynolds
reynolds@marylou4.byu.edu's password:
Remote working directory is /bluehome/reynolds
psftp> cd bin
Remote directory is now /bluehome/reynolds/bin
psftp> lcd PPIU
New local directory is C:\Documents and Settings\MECheckout\Desktop\PPIU
psftp> put ppivexe ppivexe1
local:ppivexe => remote:/bluehome/reynolds/bin/ppivexe1
psftp> get ppivexe1 ppivexe2
remote:/bluehome/reynolds/bin/ppivexe1 => local:ppivexe2
psftp> _
```

Figure A.4: PSFTP command prompt with commands on how to transfer files.

A.6 Running PPIV Executable

Now that the configuration files have been created you are ready to run the executable. Line 6 of the example code shows the name and location of the executable.

6. PROG=/fslhome/reynolds/bin/ppivexe

The executable has been named ppivexe. It needs to be located in the bin directory which will need to be created. You will need to move the executable from the computer you are using to the supercomputer and into the bin directory. See Transferring Files to accomplish this.

After writing your script, configuration files, and locating all the needed information into the correct directories you are ready to submit your job to the supercomputer. Refer to the Learning How to Submit a Job to submit the job.

Because of the nature of computers, your first job will most likely not run. This could be for several reasons. To find out why your code isn't running the best place to look will be the error file that is generated when a code runs (refer to the PBS Batch tutorials). Reading through this document may give you an idea where the glitch is. The problem may be as simple as a spelling or typing error (it's really easy to mix up the #1 and the letter l) or it may be a complex error such as a need to re compile. (If you believe the error is due to compiling refer to the section on compiling). The only way to find the error is to search. With time you will be able to locate the error. Don't be afraid to resubmit the job after you've made some corrections. With luck you'll have a perfect running job in no time.

APPENDIX B. FLOW VISUALIZATION IMAGES

This appendix is intended to supply the reader with additional images showing the flow between the upstream deswirlor and the downstream rotor. Figures are included for close, mid and far spacings at nominal and decreased loading for most blade delays.

B.1 Close Spacing, Nominal Loading



Figure B.1: Close spacing, Nominal loading, Blade Delay 0



Figure B.2: Close spacing, Nominal loading, Blade Delay 40

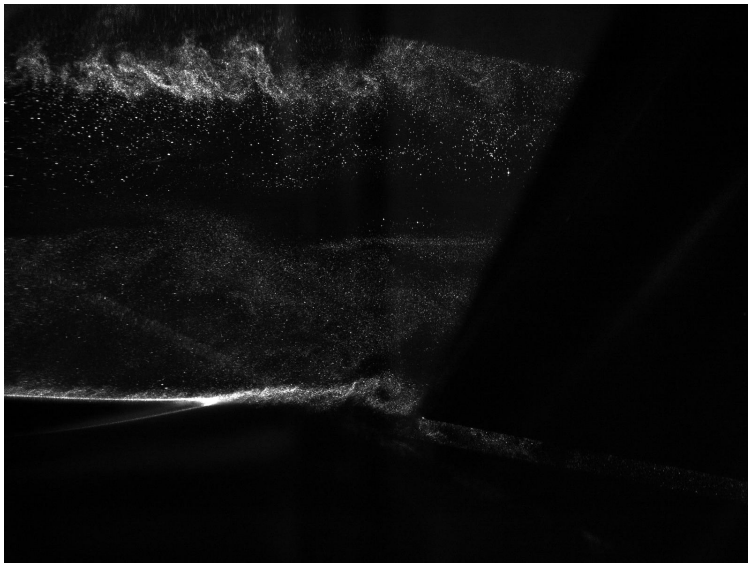


Figure B.3: Close spacing, Nominal loading, Blade Delay 60



Figure B.4: Close spacing, Nominal loading, Blade Delay 80

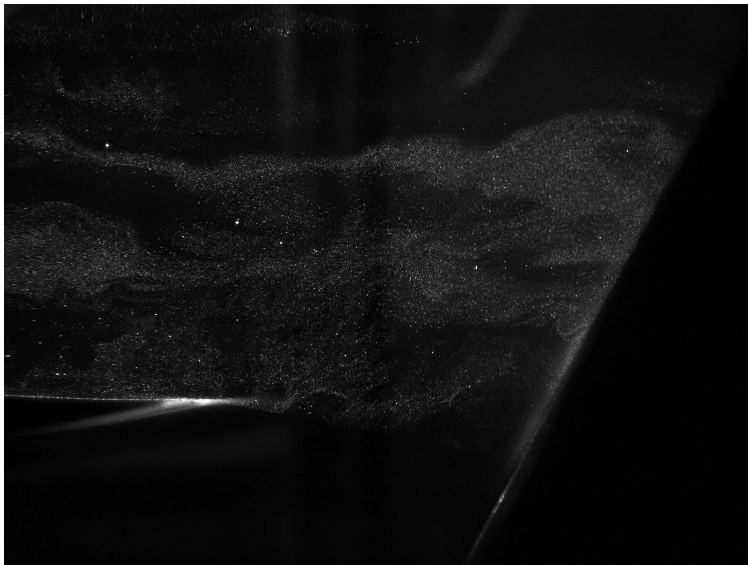


Figure B.5: Close spacing, Nominal loading, Blade Delay 100



Figure B.6: Close spacing, Nominal loading, Blade Delay 120

B.2 Mid Spacing, Nominal Loading



Figure B.7: Mid spacing, Nominal loading, Blade Delay 0

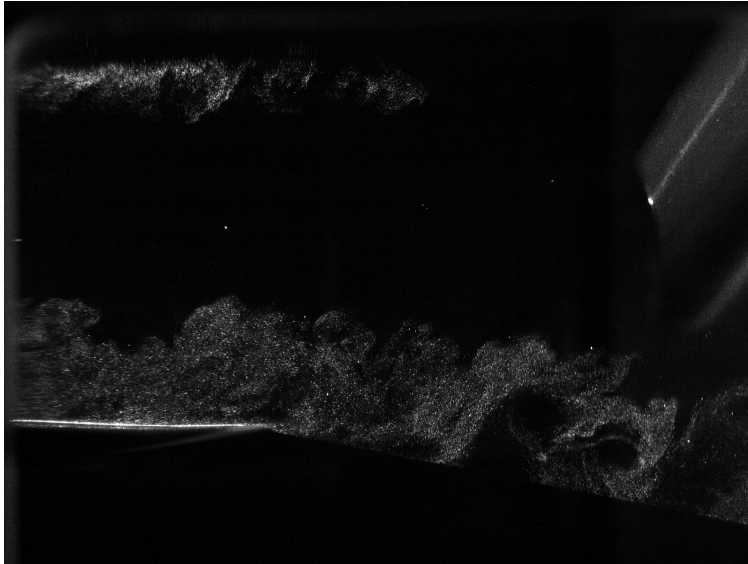


Figure B.8: Mid spacing, Nominal loading, Blade Delay 20

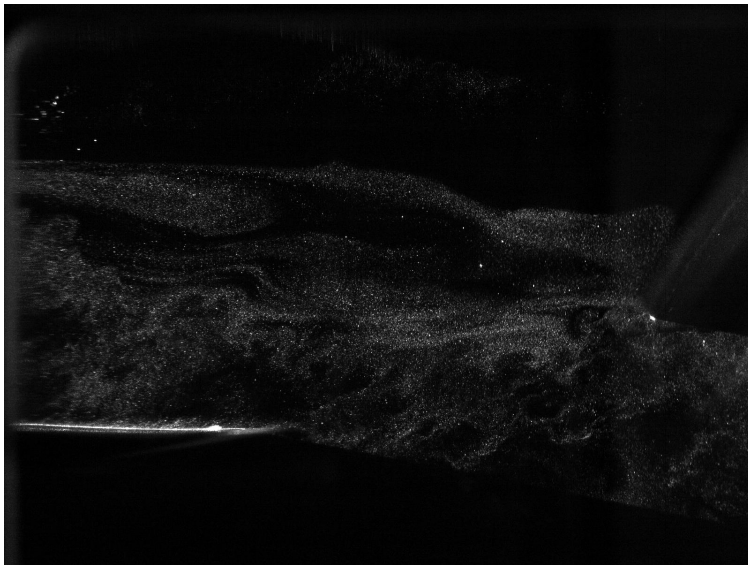


Figure B.9: Mid spacing, Nominal loading, Blade Delay 40

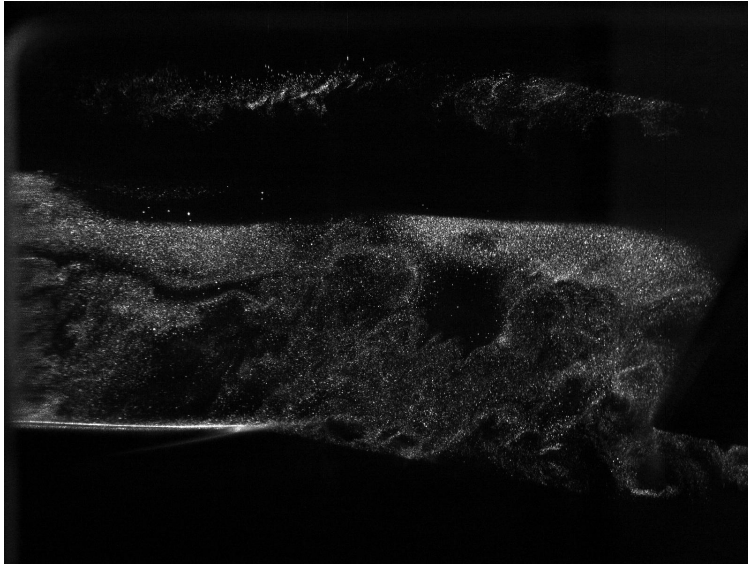


Figure B.10: Mid spacing, Nominal loading, Blade Delay 60

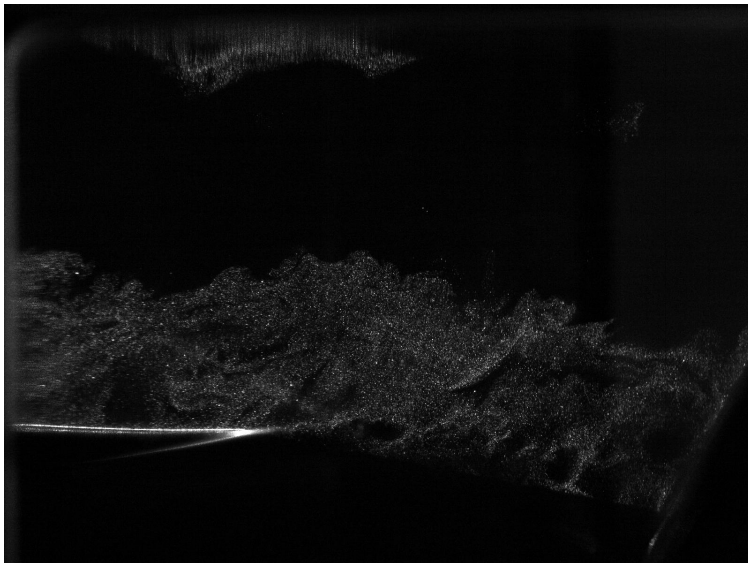


Figure B.11: Mid spacing, Nominal loading, Blade Delay 80

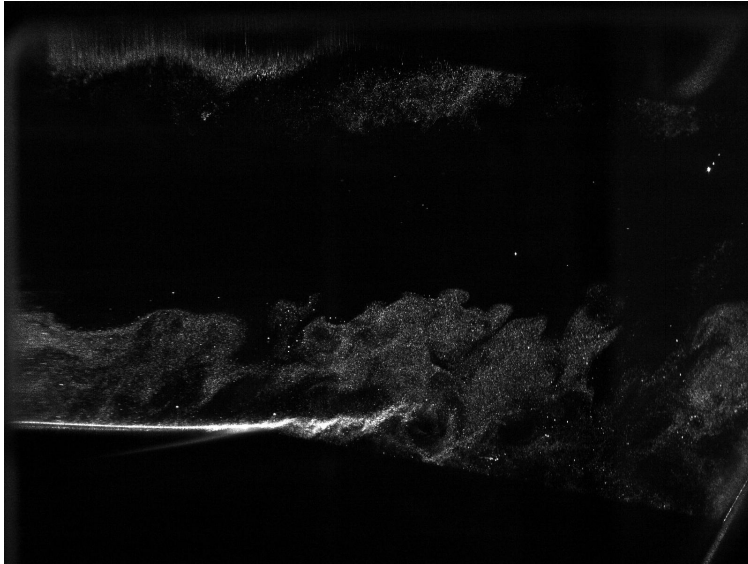


Figure B.12: Mid spacing, Nominal loading, Blade Delay 100

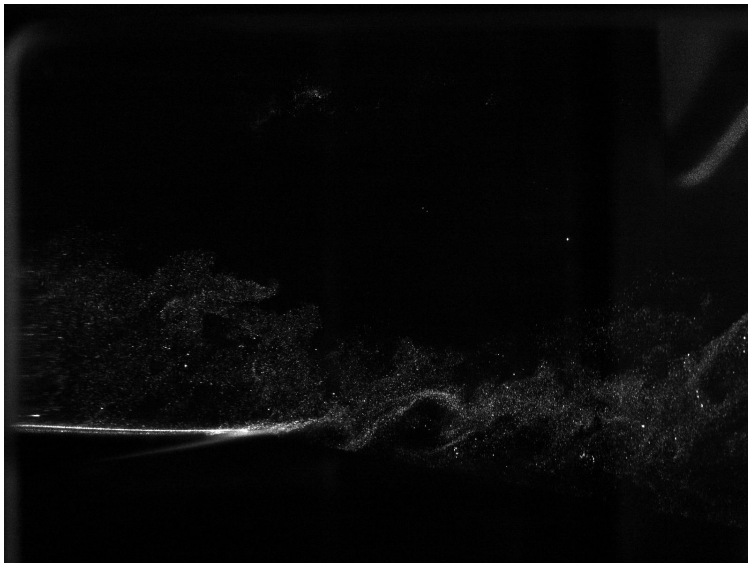


Figure B.13: Mid spacing, Nominal loading, Blade Delay 120

B.3 Mid Spacing, Decreased Loading

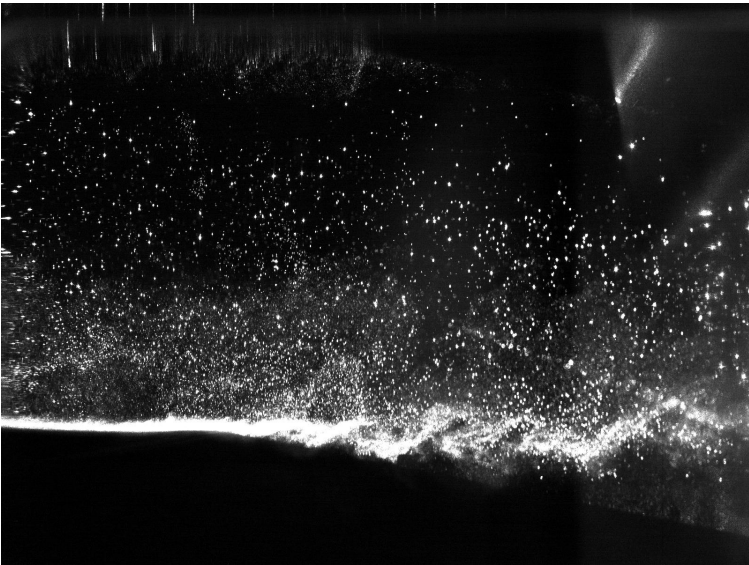


Figure B.14: Mid spacing, Decreased loading, Blade Delay 0

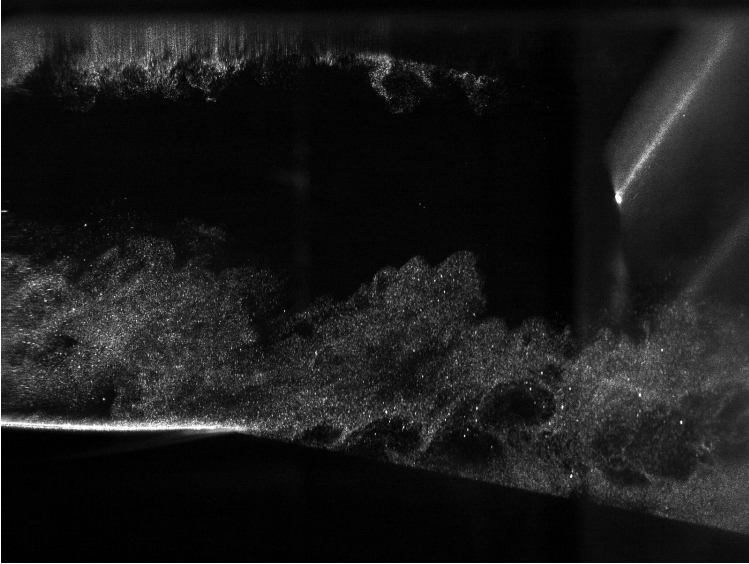


Figure B.15: Mid spacing, Decreased loading, Blade Delay 20

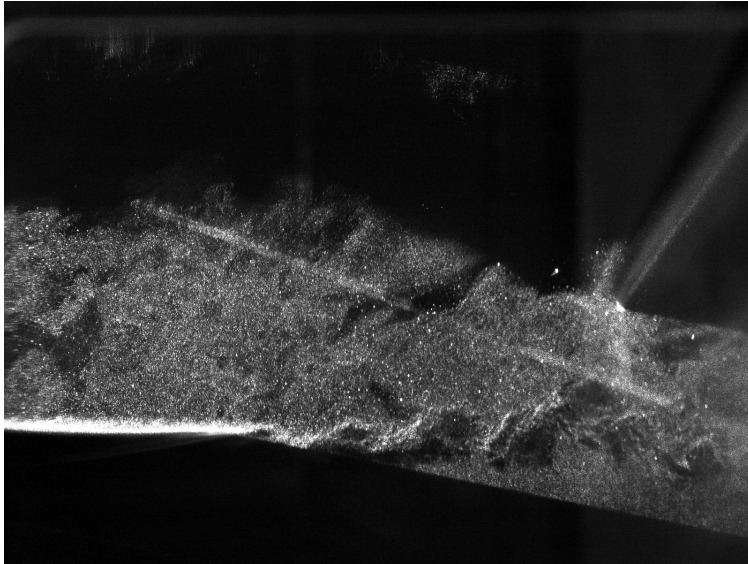


Figure B.16: Mid spacing, Decreased loading, Blade Delay 40

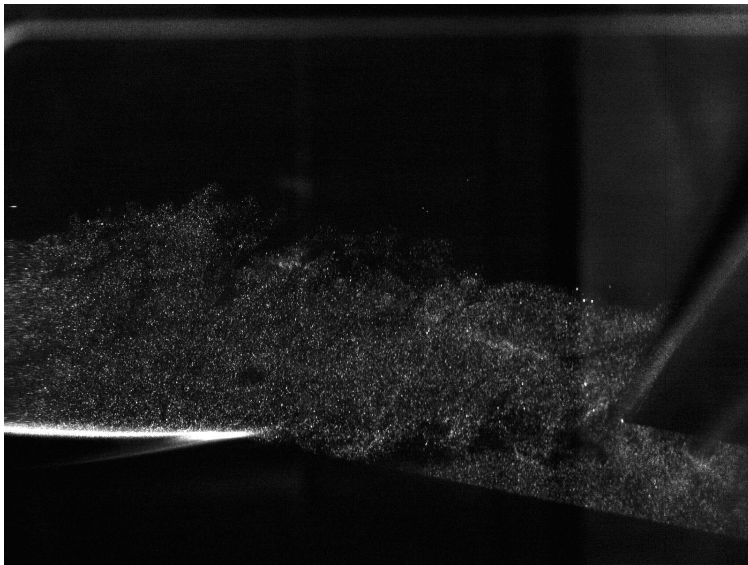


Figure B.17: Mid spacing, Decreased loading, Blade Delay 60

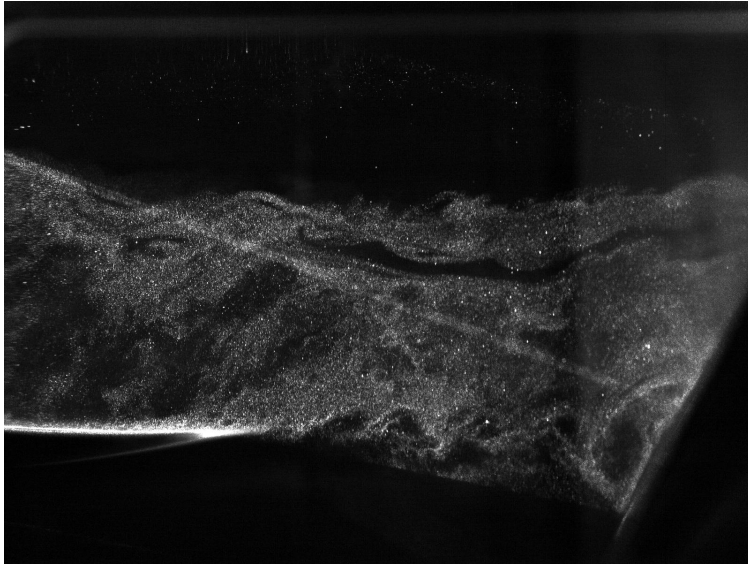


Figure B.18: Mid spacing, Decreased loading, Blade Delay 80

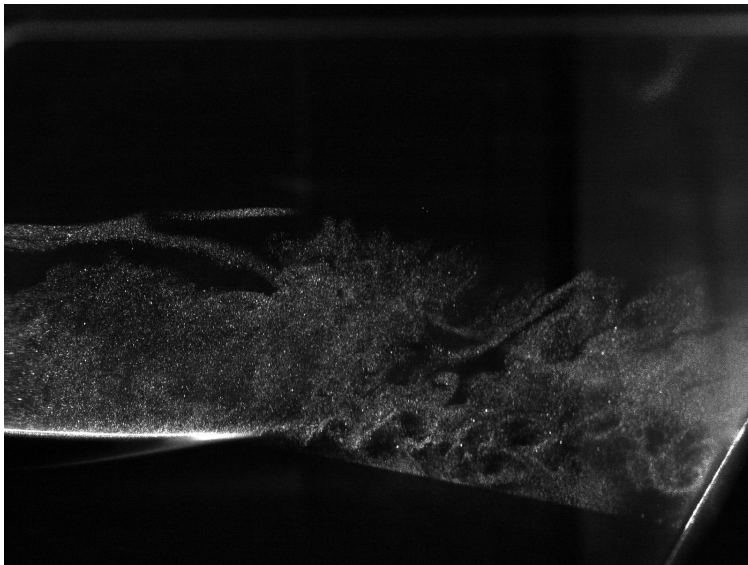


Figure B.19: Mid spacing, Decreased loading, Blade Delay 100

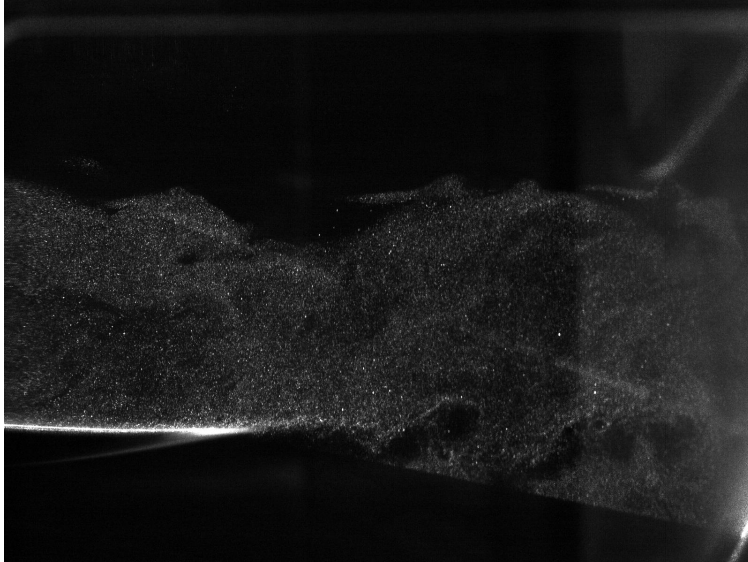


Figure B.20: Mid spacing, Decreased loading, Blade Delay 120

B.4 Far Spacing, Nominal Loading

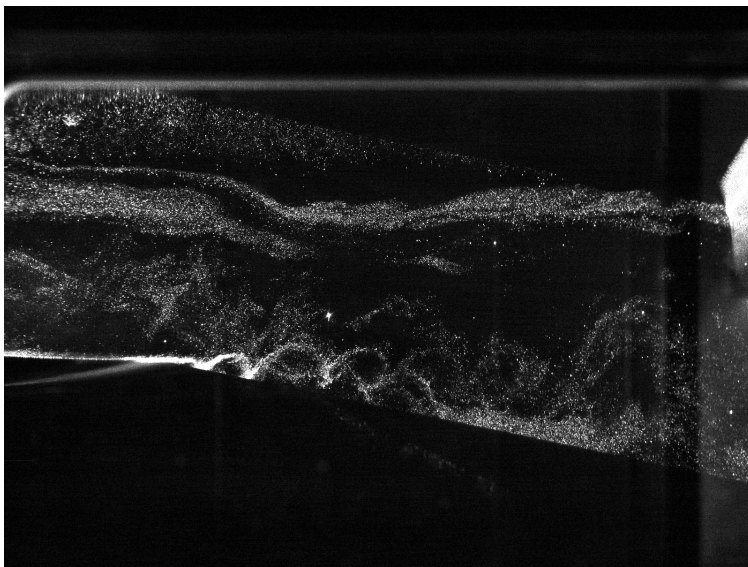


Figure B.21: Far spacing, Nominal loading, Blade Delay 20

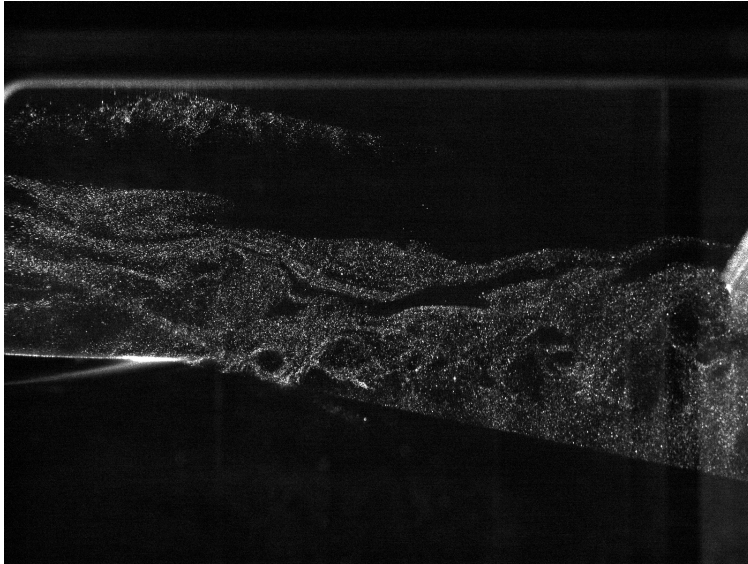


Figure B.22: Far spacing, Nominal loading, Blade Delay 40

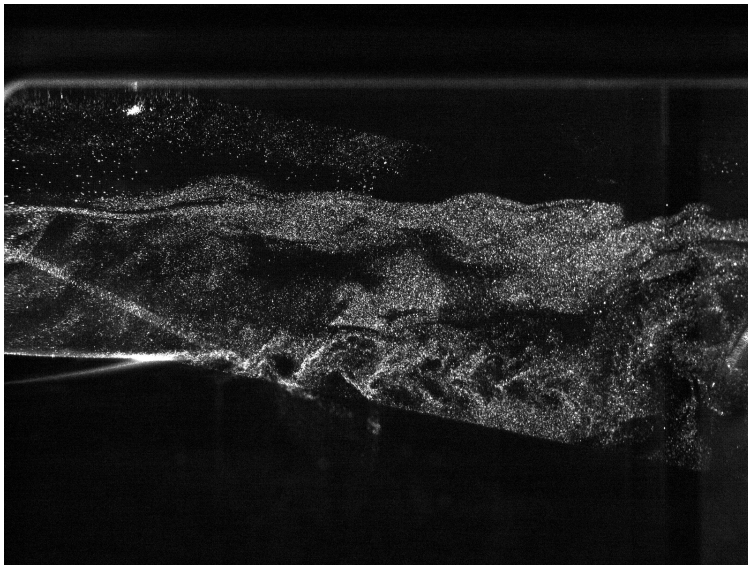


Figure B.23: Far spacing, Nominal loading, Blade Delay 60

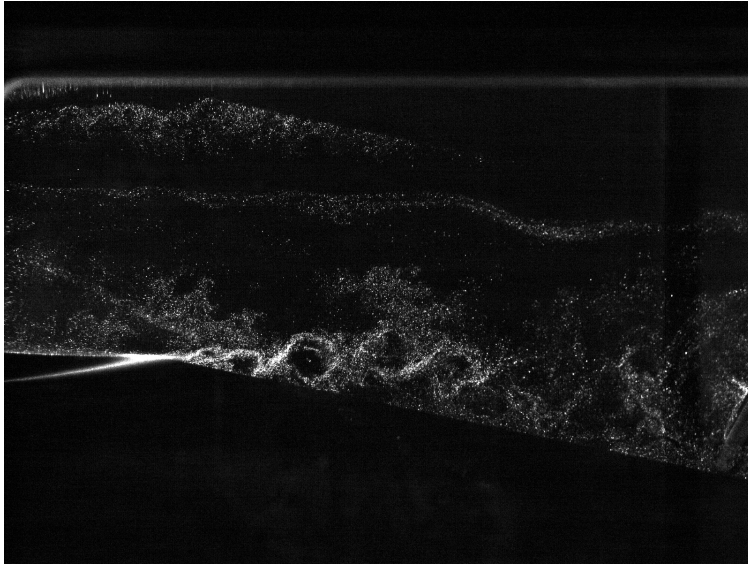


Figure B.24: Far spacing, Nominal loading, Blade Delay 80

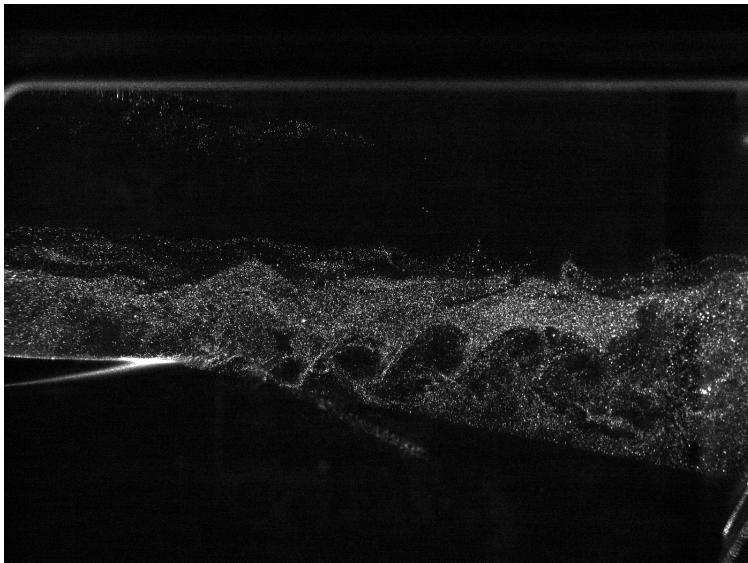


Figure B.25: Far spacing, Nominal loading, Blade Delay 100

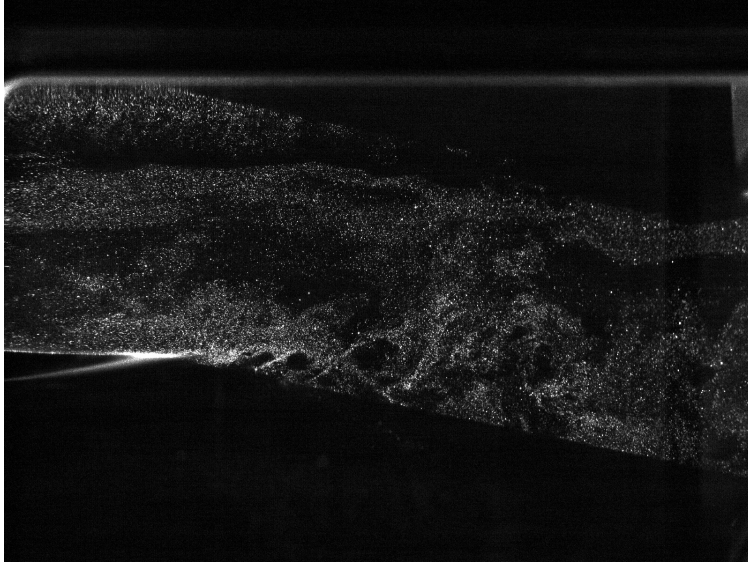


Figure B.26: Far spacing, Nominal loading, Blade Delay 120

B.5 Far Spacing, Decreased Loading

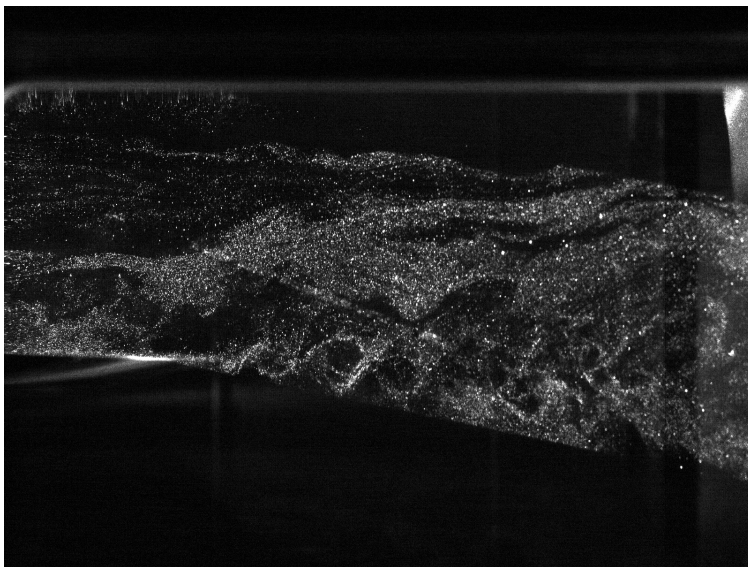


Figure B.27: Far spacing, Decreased loading, Blade Delay 0

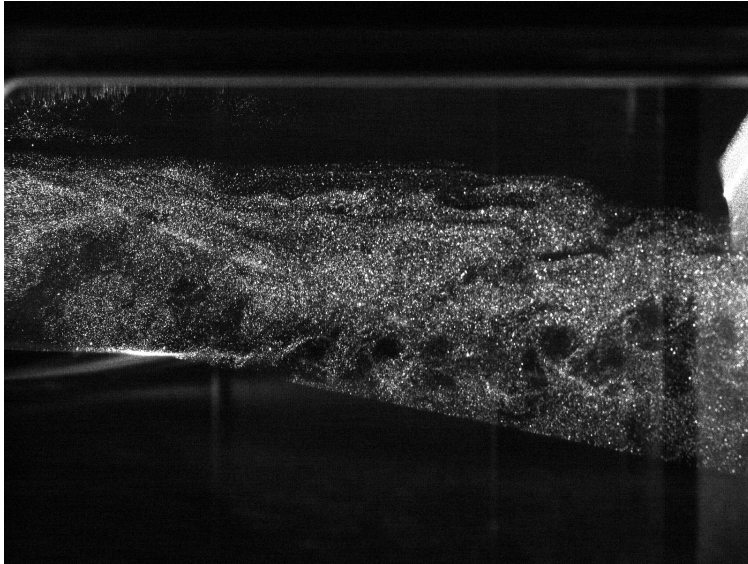


Figure B.28: Far spacing, Decreased loading, Blade Delay 20

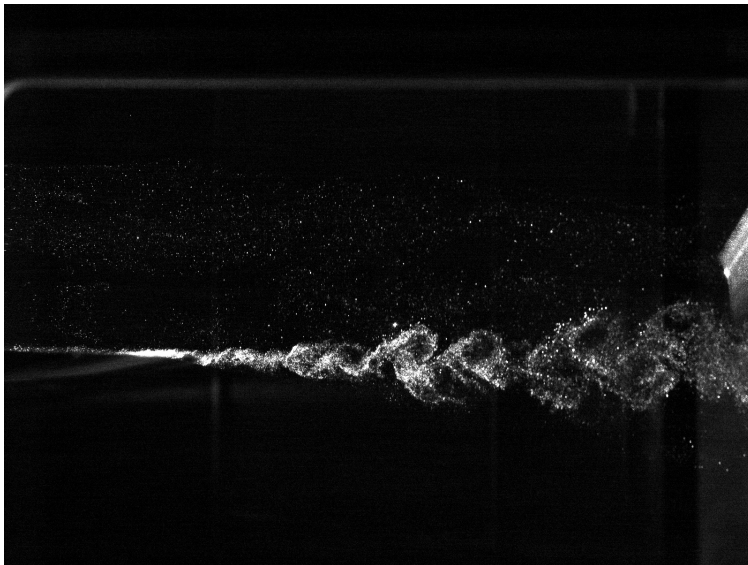


Figure B.29: Far spacing, Decreased loading, Blade Delay 40

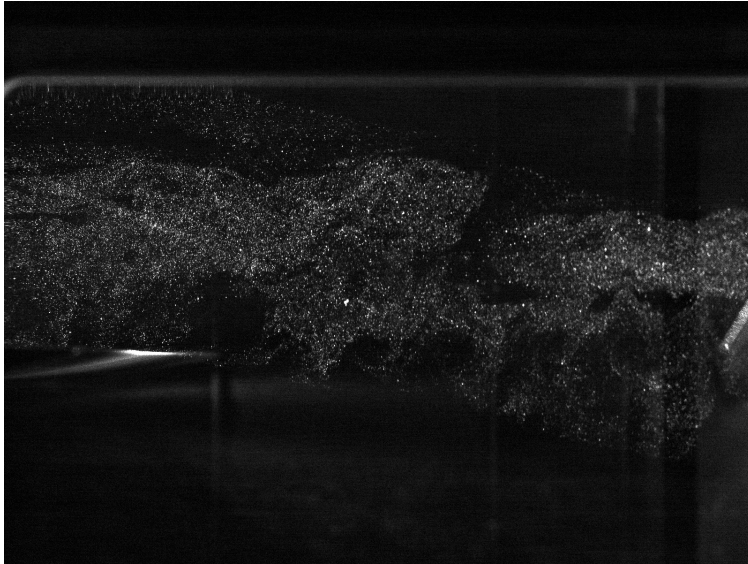


Figure B.30: Far spacing, Decreased loading, Blade Delay 60

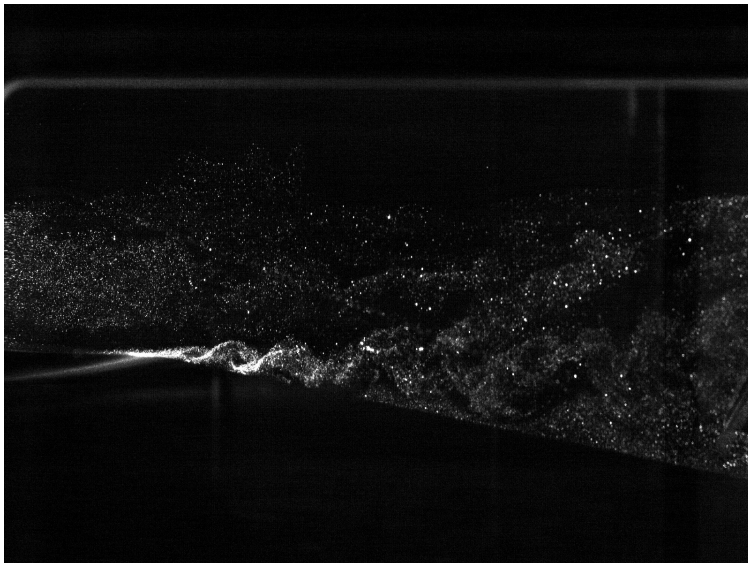


Figure B.31: Far spacing, Decreased loading, Blade Delay 80

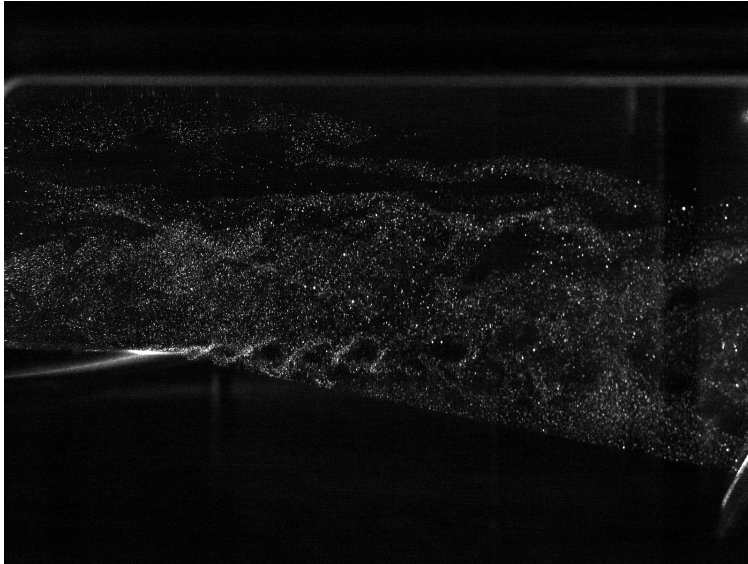


Figure B.32: Far spacing, Decreased loading, Blade Delay 100

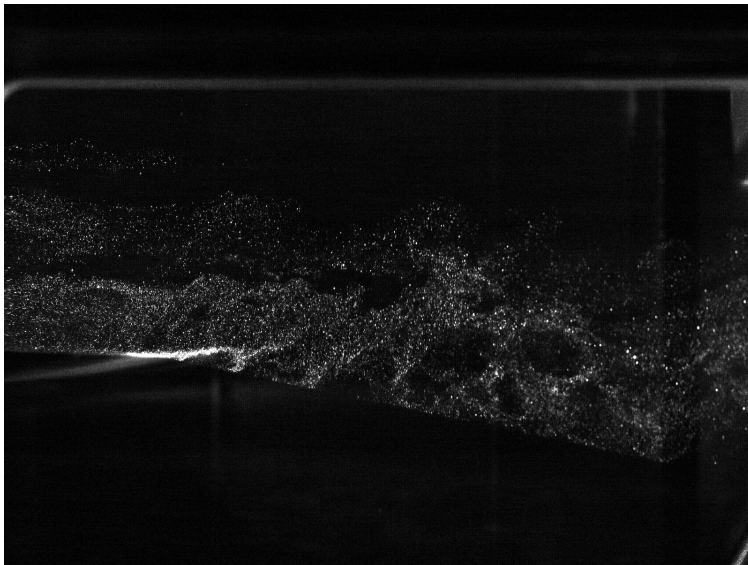


Figure B.33: Far spacing, Decreased loading, Blade Delay 120

APPENDIX C. SPEED CONTOURS

This appendix is intended to supply the reader with additional images showing the flow between the upstream deswirlor and the downstream rotor. Figures are included for close, mid and far spacings at nominal and decreased loading for most blade delays.

C.1 Close Spacing, Nominal Loading

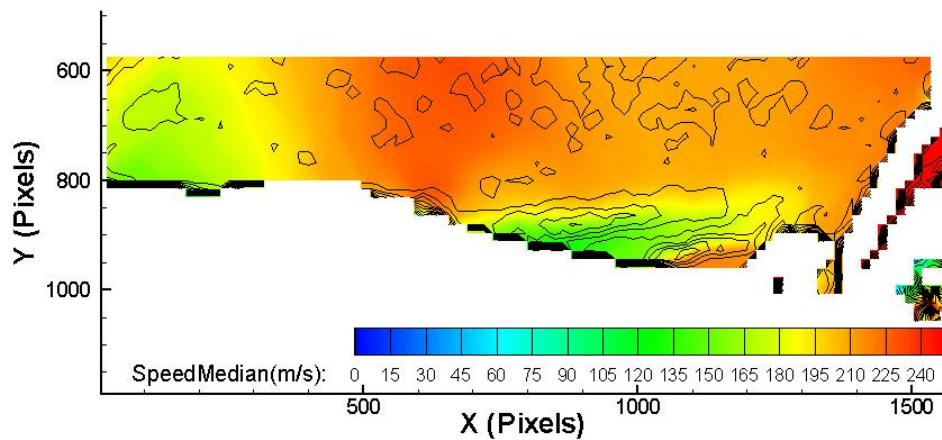


Figure C.1: Close spacing, Nominal loading, Blade Delay 0

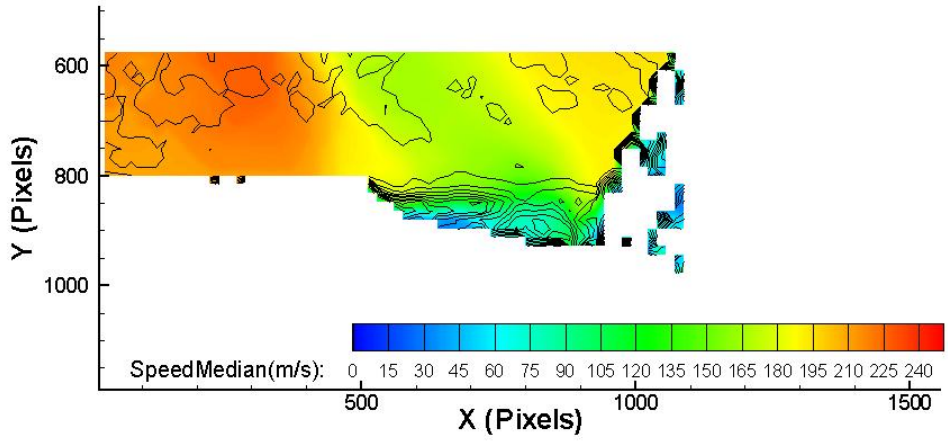


Figure C.2: Close spacing, Nominal loading, Blade Delay 20

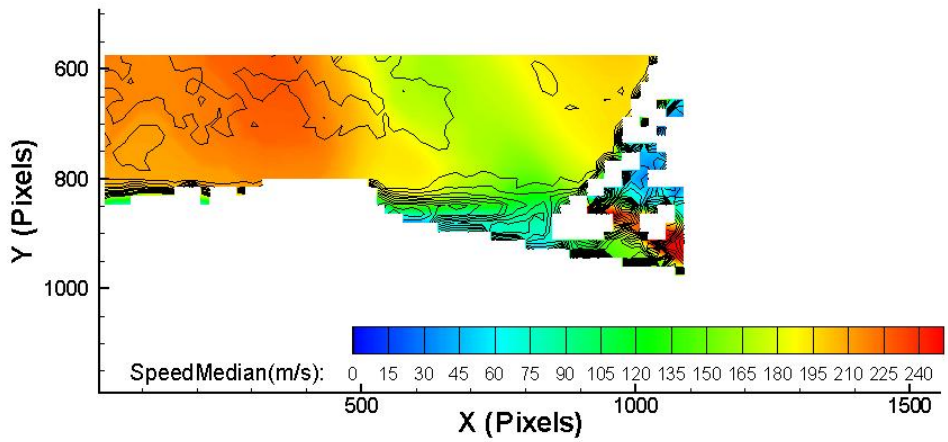


Figure C.3: Close spacing, Nominal loading, Blade Delay 60

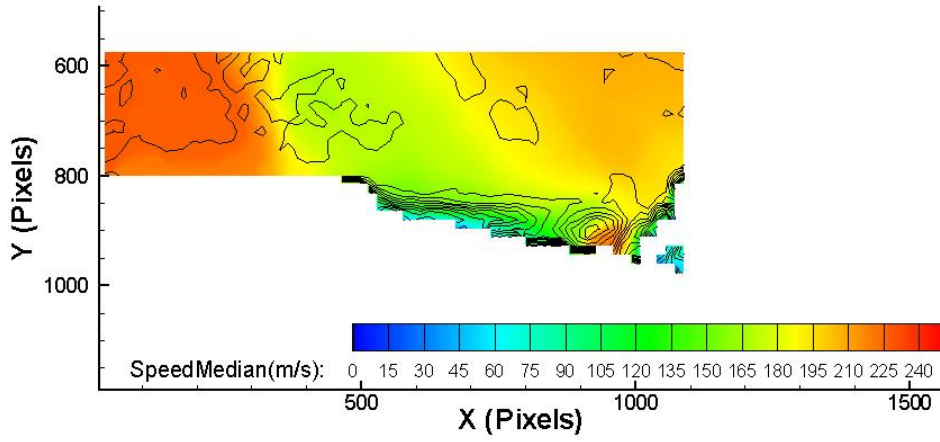


Figure C.4: Close spacing, Nominal loading, Blade Delay 80

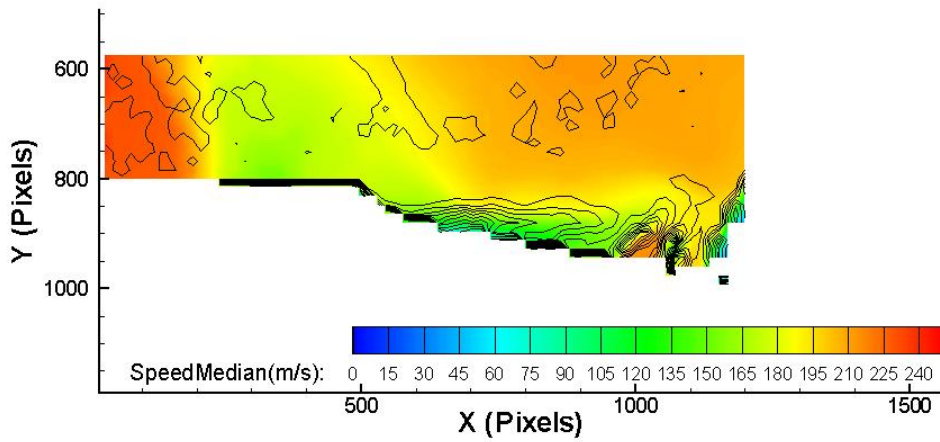


Figure C.5: Close spacing, Nominal loading, Blade Delay 100

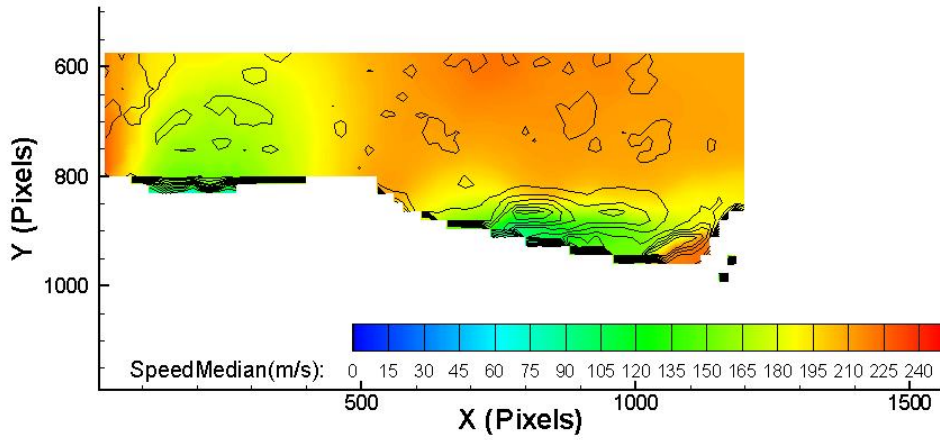


Figure C.6: Close spacing, Nominal loading, Blade Delay 120

C.2 Mid Spacing, Nominal Loading

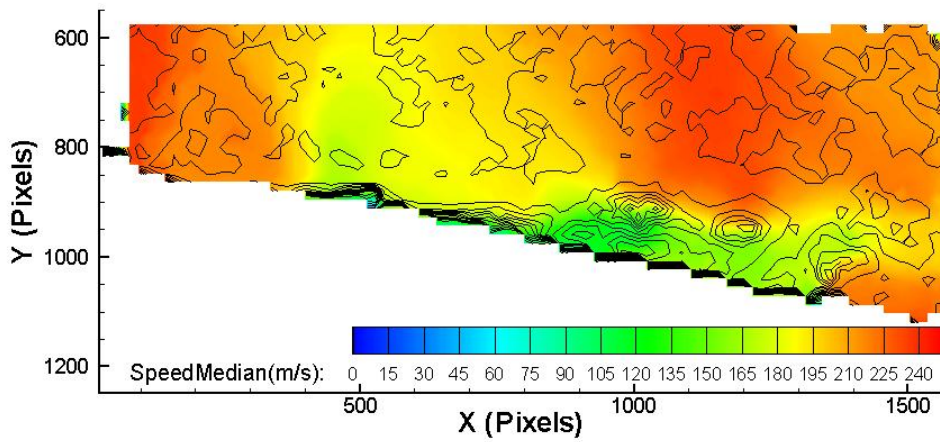


Figure C.7: Mid spacing, Nominal loading, Blade Delay 0

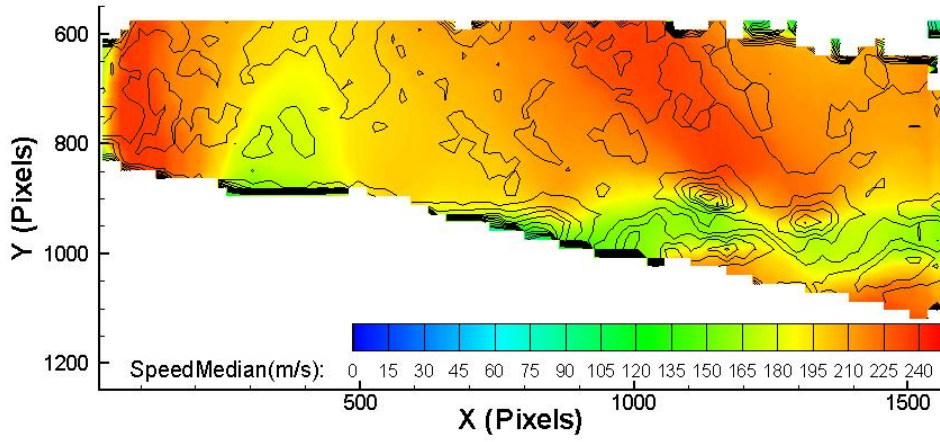


Figure C.8: Mid spacing, Nominal loading, Blade Delay 20

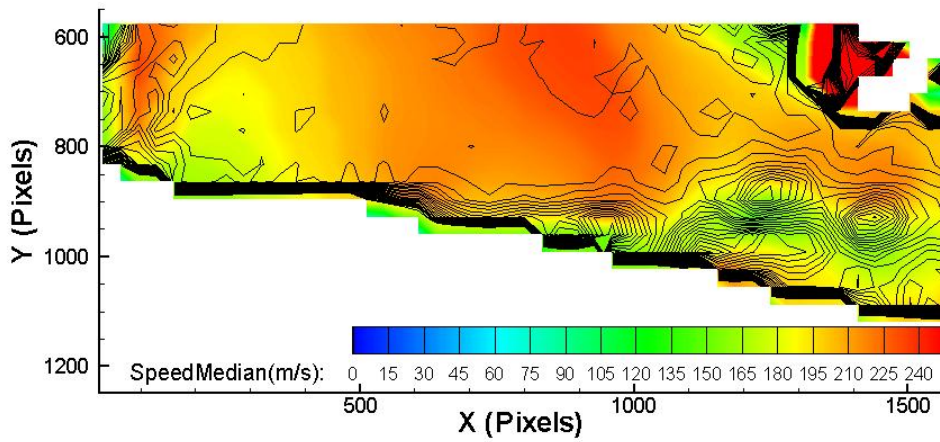


Figure C.9: Mid spacing, Nominal loading, Blade Delay 40

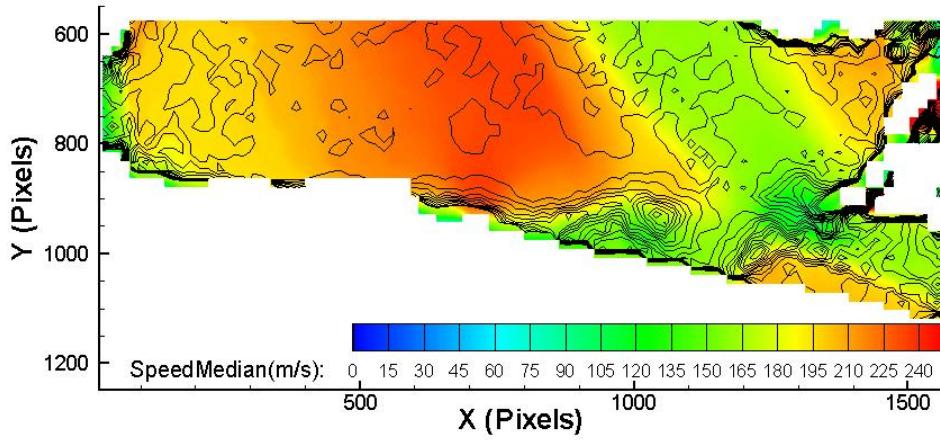


Figure C.10: Mid spacing, Nominal loading, Blade Delay 60

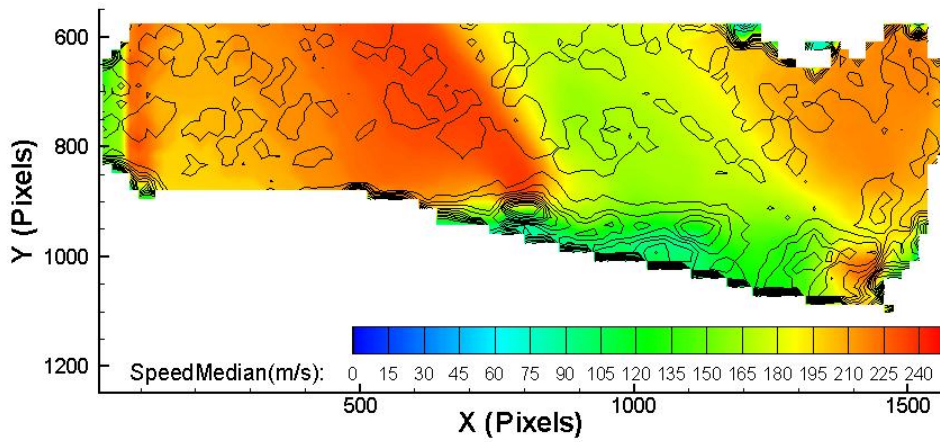


Figure C.11: Mid spacing, Nominal loading, Blade Delay 80

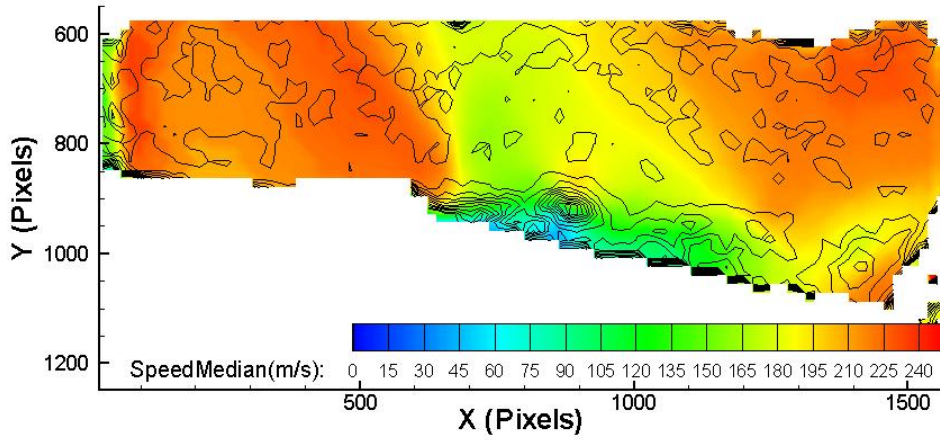


Figure C.12: Mid spacing, Nominal loading, Blade Delay 100

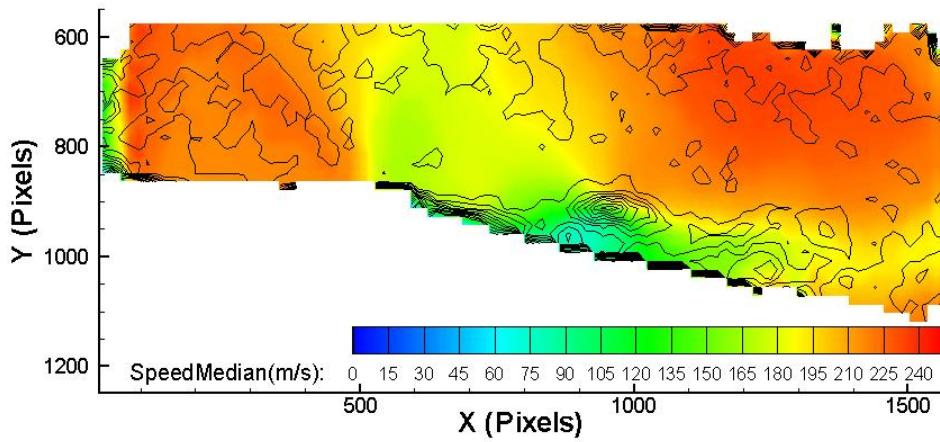


Figure C.13: Mid spacing, Nominal loading, Blade Delay 120

C.3 Mid Spacing, Decreased Loading

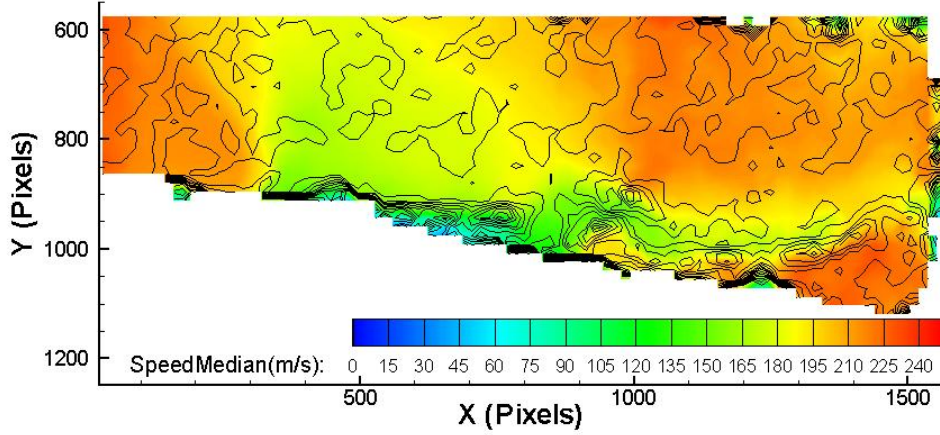


Figure C.14: Mid spacing, Decreased loading, Blade Delay 0

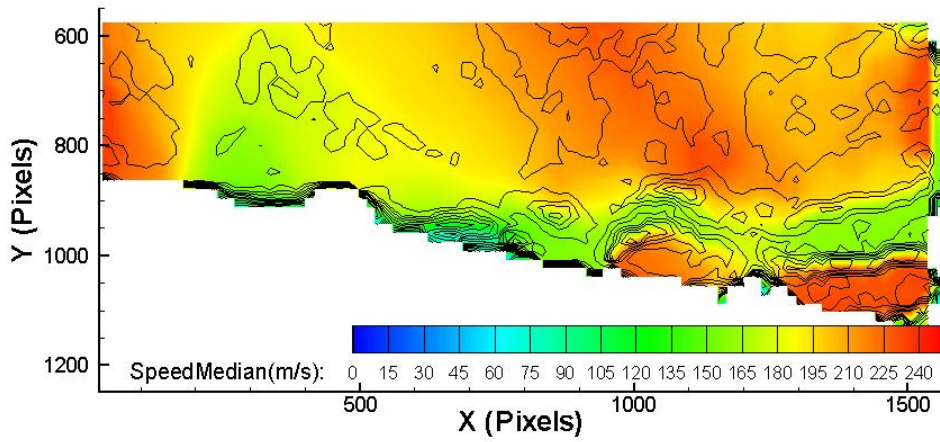


Figure C.15: Mid spacing, Decreased loading, Blade Delay 20

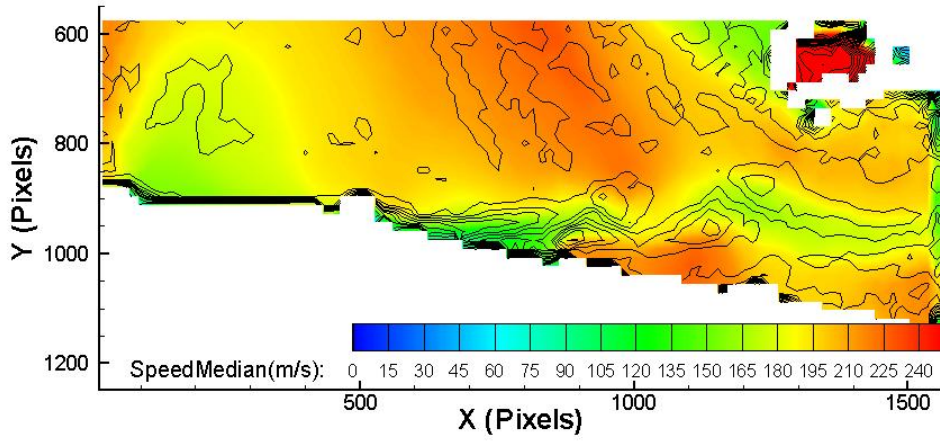


Figure C.16: Mid spacing, Decreased loading, Blade Delay 40

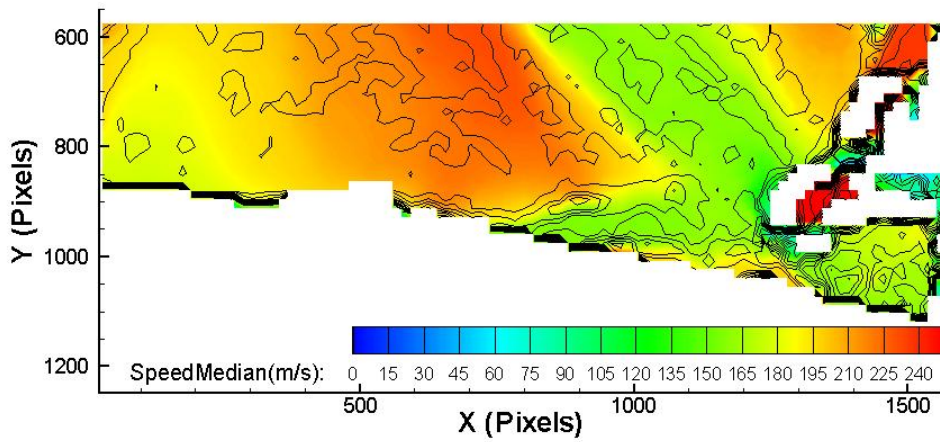


Figure C.17: Mid spacing, Decreased loading, Blade Delay 60

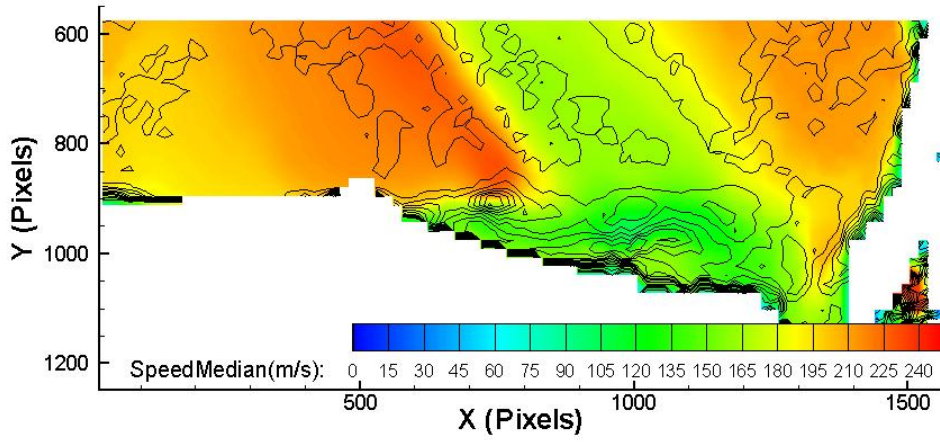


Figure C.18: Mid spacing, Decreased loading, Blade Delay 80

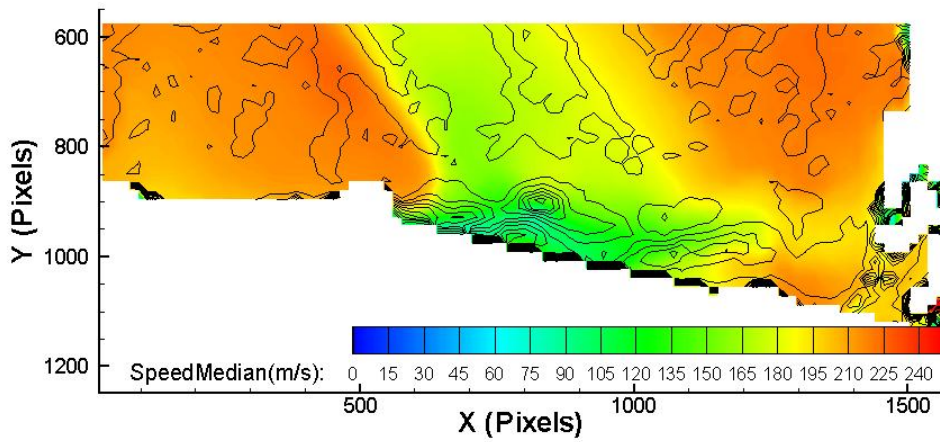


Figure C.19: Mid spacing, Decreased loading, Blade Delay 100

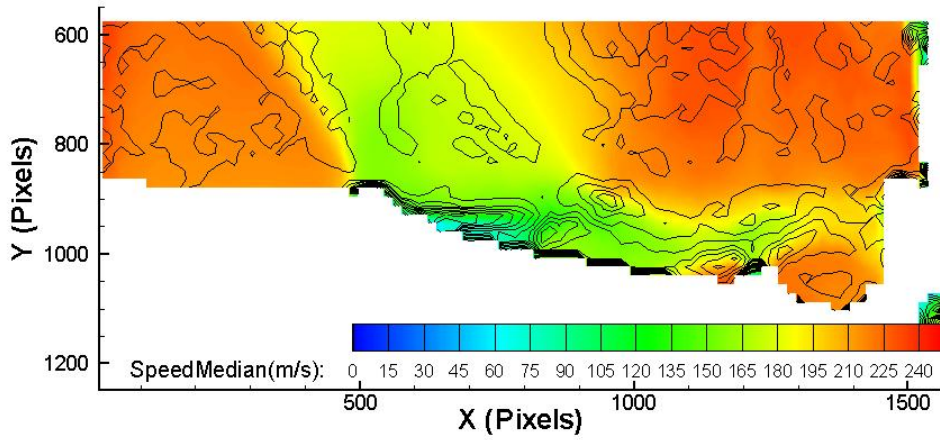


Figure C.20: Mid spacing, Decreased loading, Blade Delay 120

C.4 Far Spacing, Nominal Loading

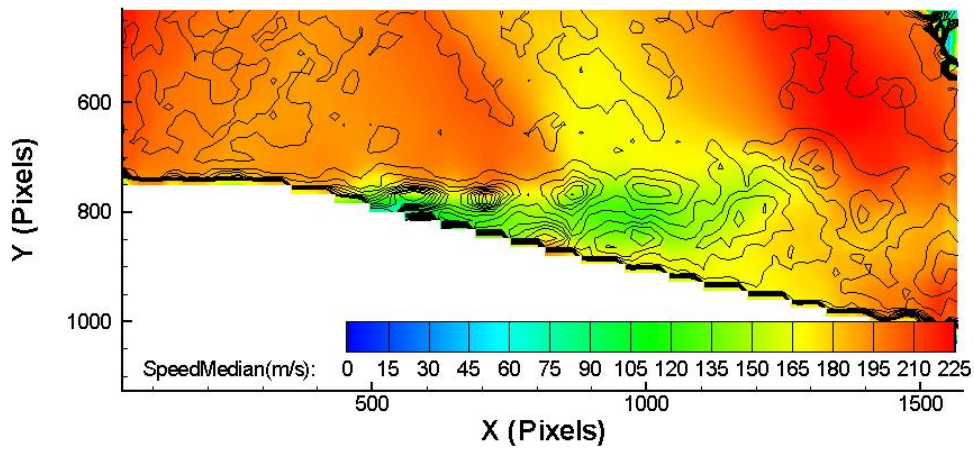


Figure C.21: Far spacing, Nominal loading, Blade Delay 0

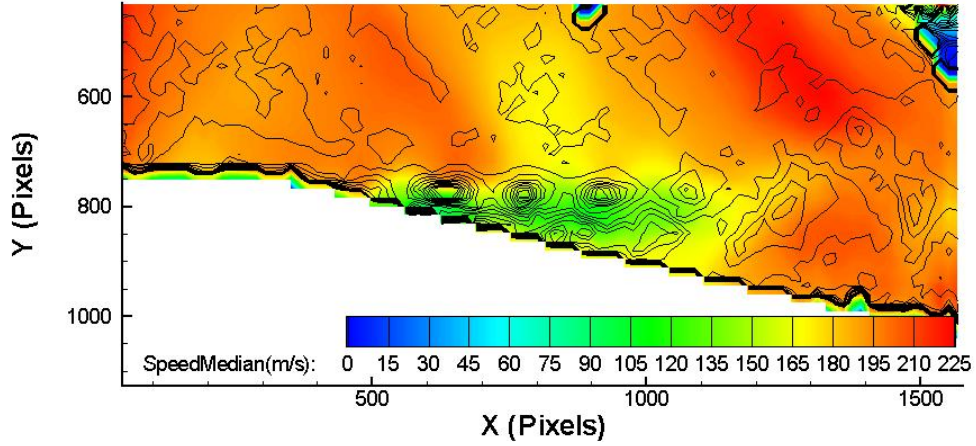


Figure C.22: Far spacing, Nominal loading, Blade Delay 20

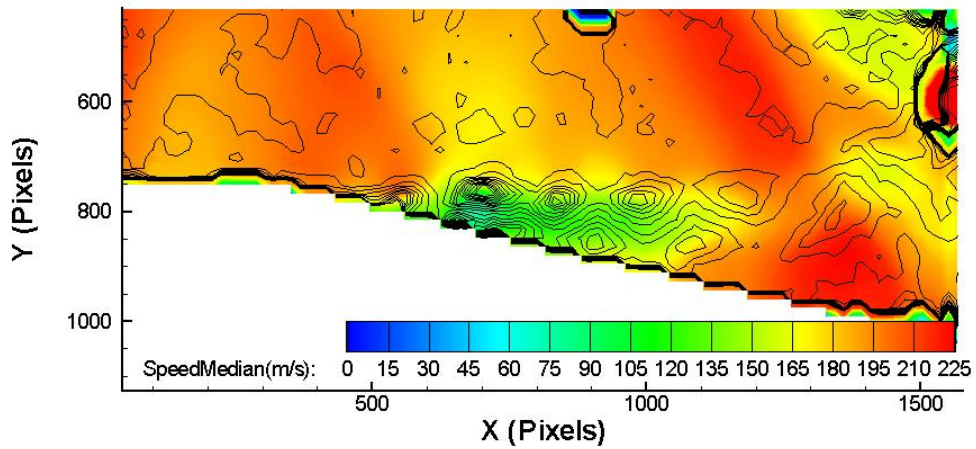


Figure C.23: Far spacing, Nominal loading, Blade Delay 40

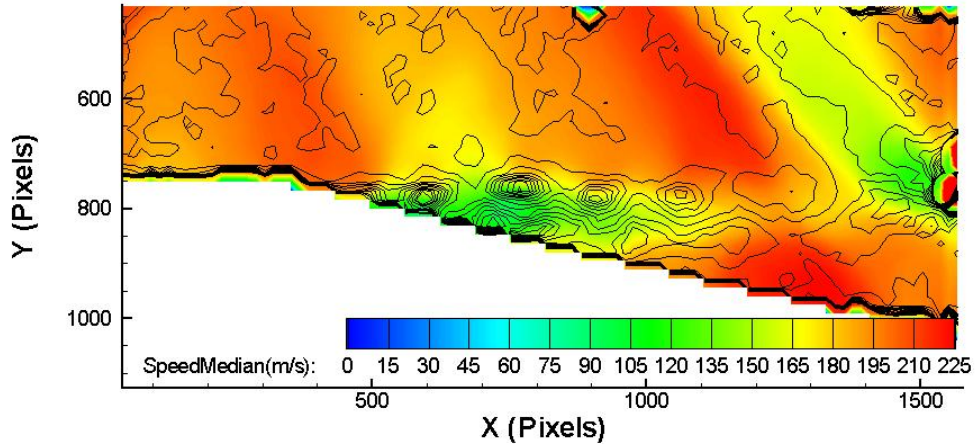


Figure C.24: Far spacing, Nominal loading, Blade Delay 60

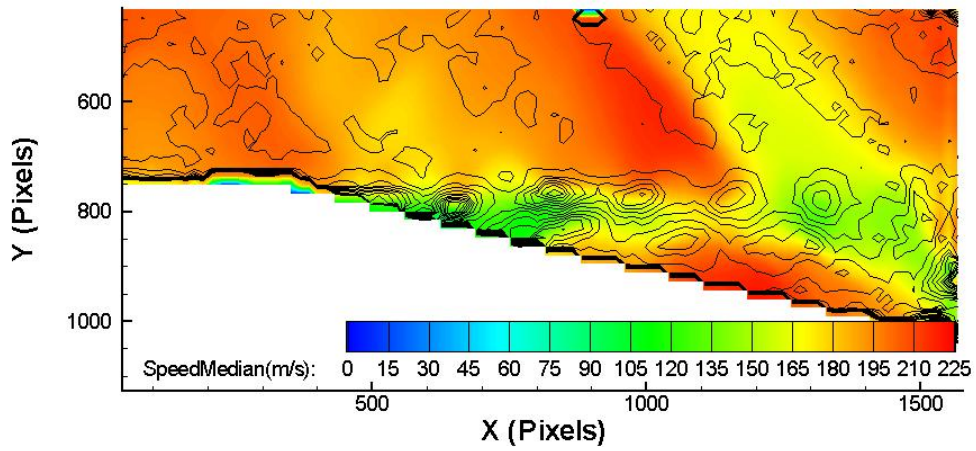


Figure C.25: Far spacing, Nominal loading, Blade Delay 80

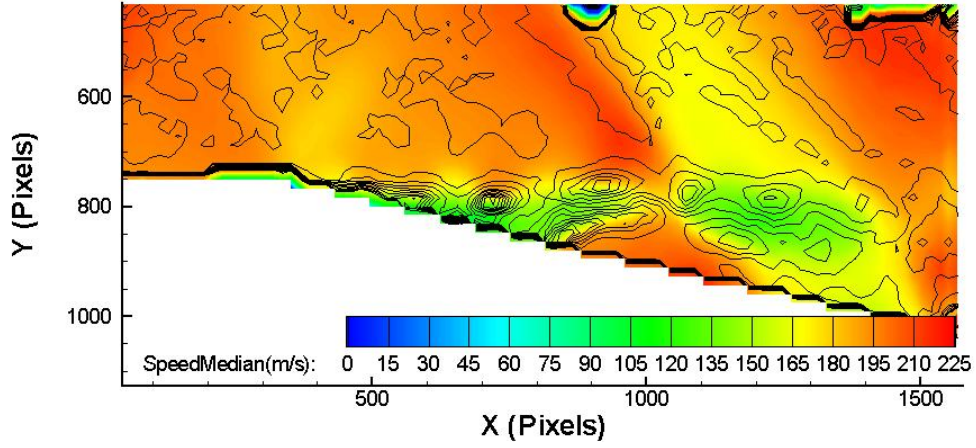


Figure C.26: Far spacing, Nominal loading, Blade Delay 100

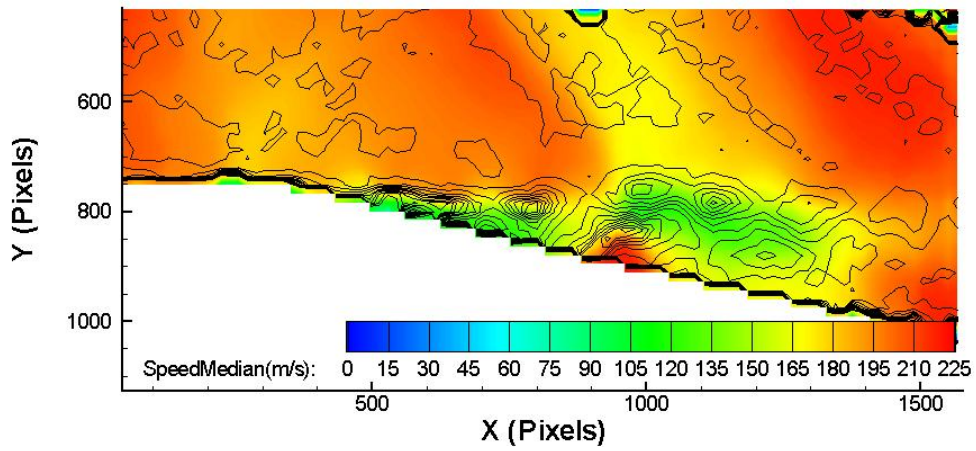


Figure C.27: Far spacing, Nominal loading, Blade Delay 120

C.5 Far Spacing, Decreased Loading

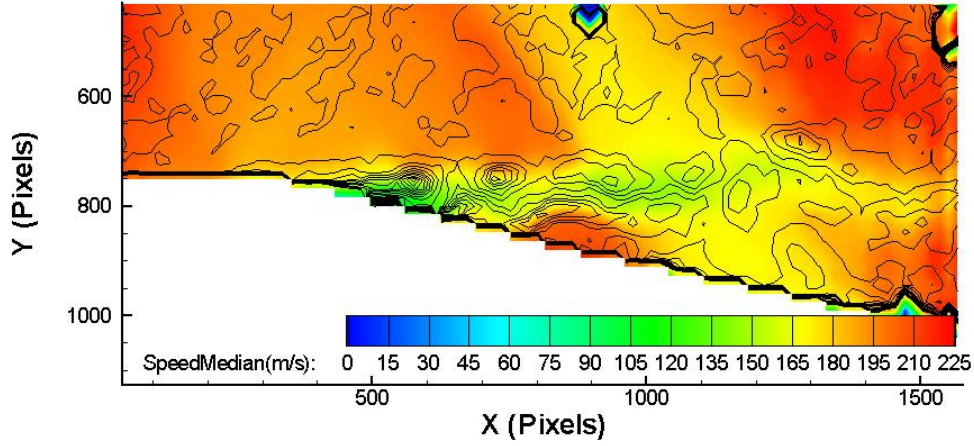


Figure C.28: Far spacing, Decreased loading, Blade Delay 0

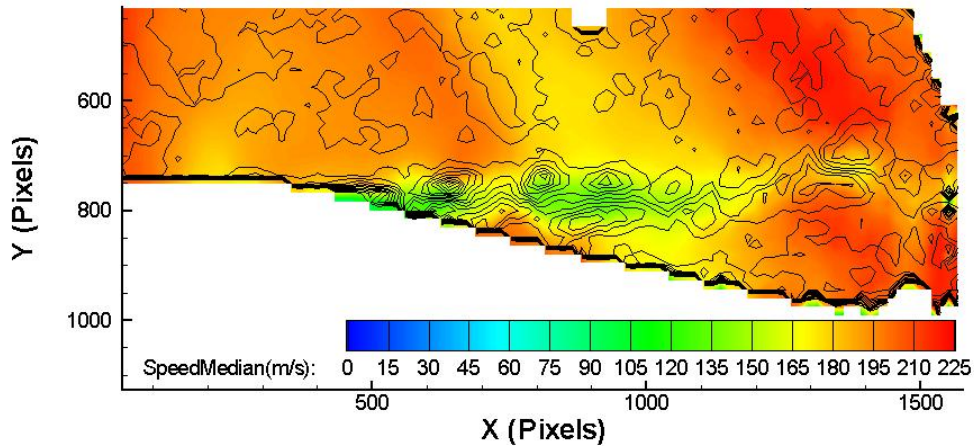


Figure C.29: Far spacing, Decreased loading, Blade Delay 20

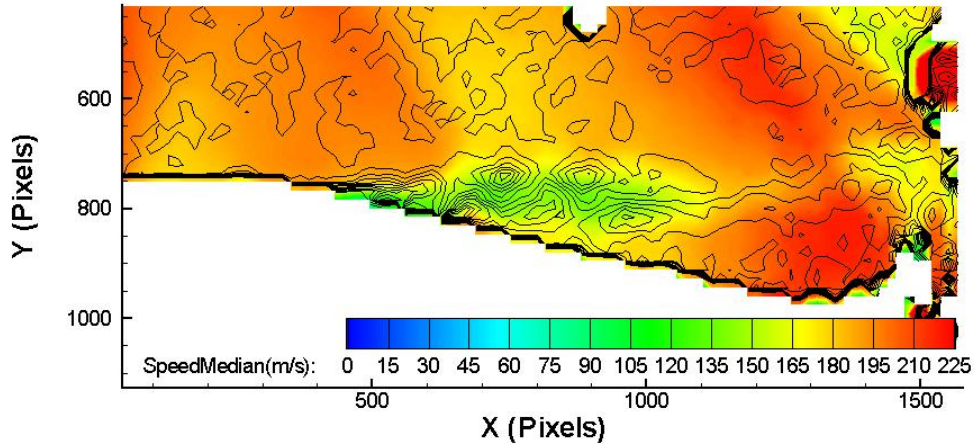


Figure C.30: Far spacing, Decreased loading, Blade Delay 40

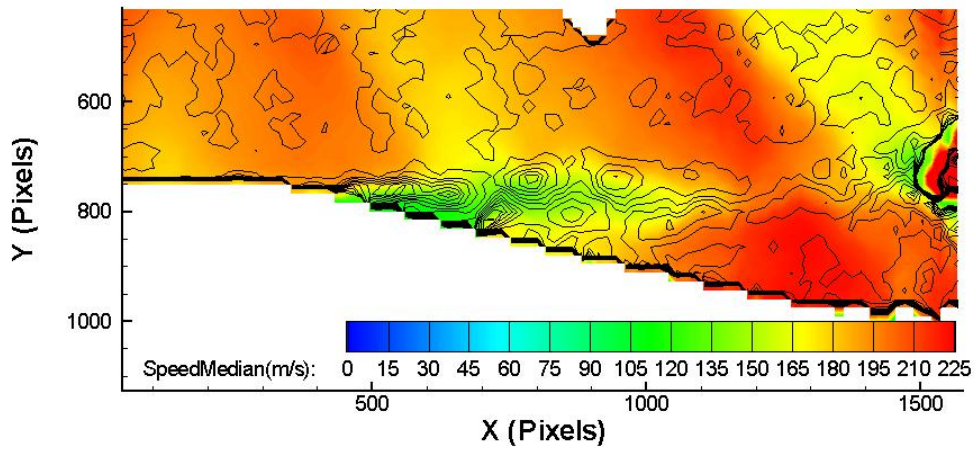


Figure C.31: Far spacing, Decreased loading, Blade Delay 60

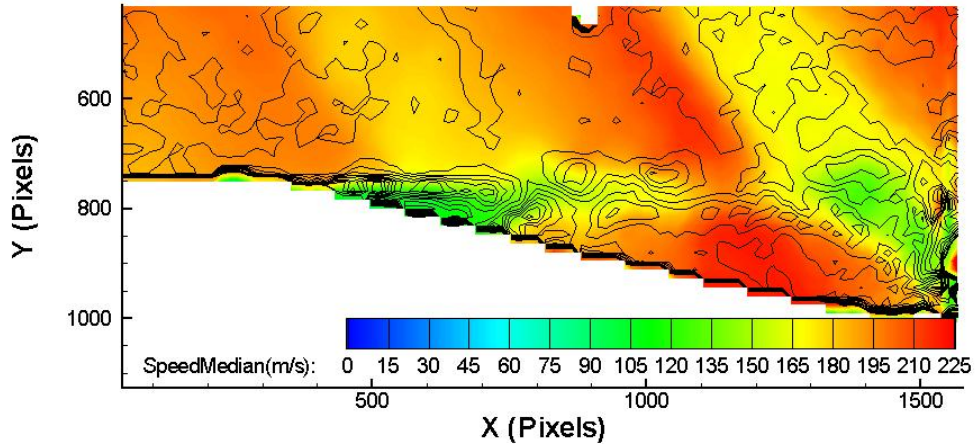


Figure C.32: Far spacing, Decreased loading, Blade Delay 80

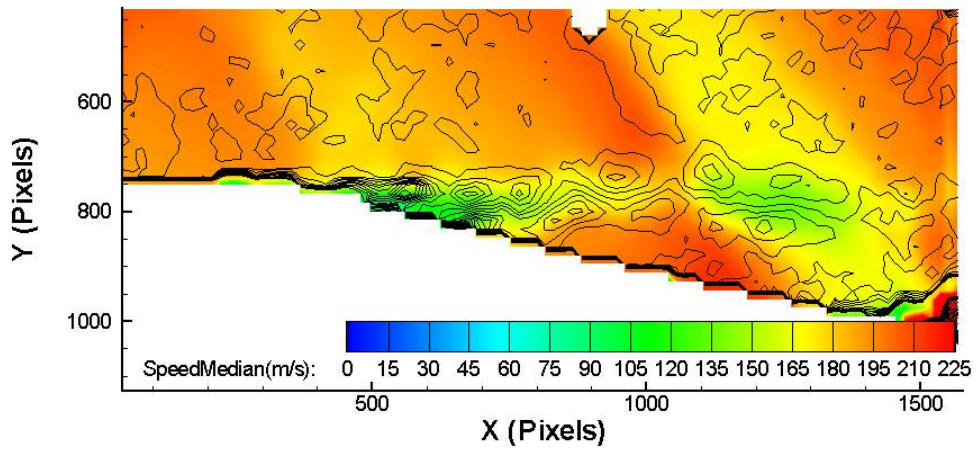


Figure C.33: Far spacing, Decreased loading, Blade Delay 100

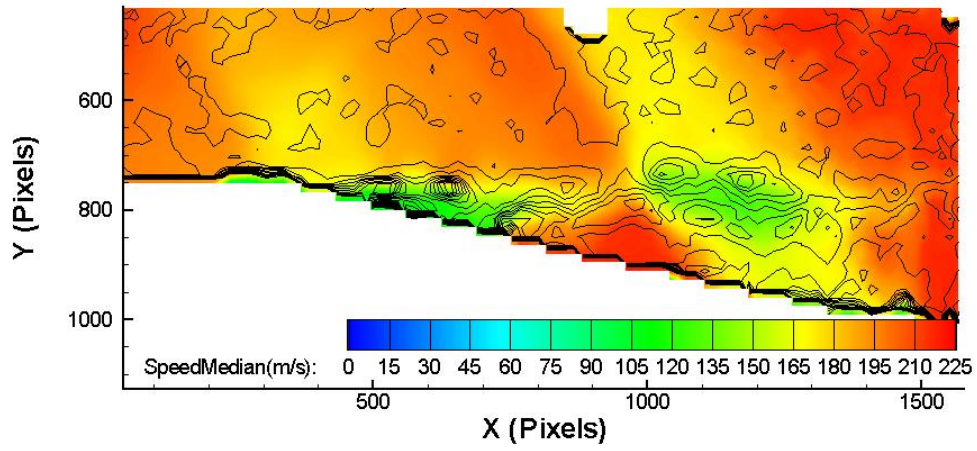


Figure C.34: Far spacing, Decreased loading, Blade Delay 120

APPENDIX D. VORTICITY CONTOURS

This appendix is intended to supply the reader with additional images showing the flow between the upstream deswirlor and the downstream rotor. Figures are included for close, mid and far spacings at nominal and decreased loading for most blade delays.

D.1 Close Spacing, Nominal Loading

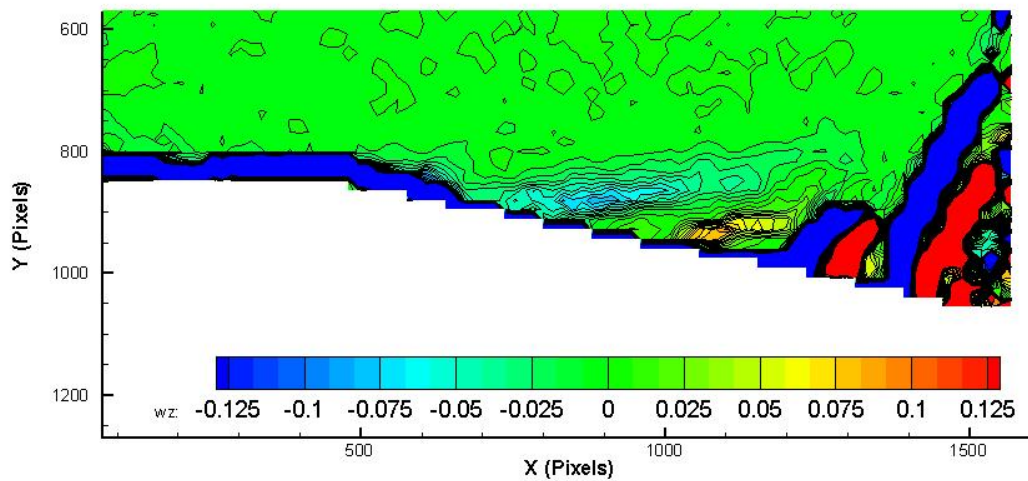


Figure D.1: Close spacing, Nominal loading, Blade Delay 0

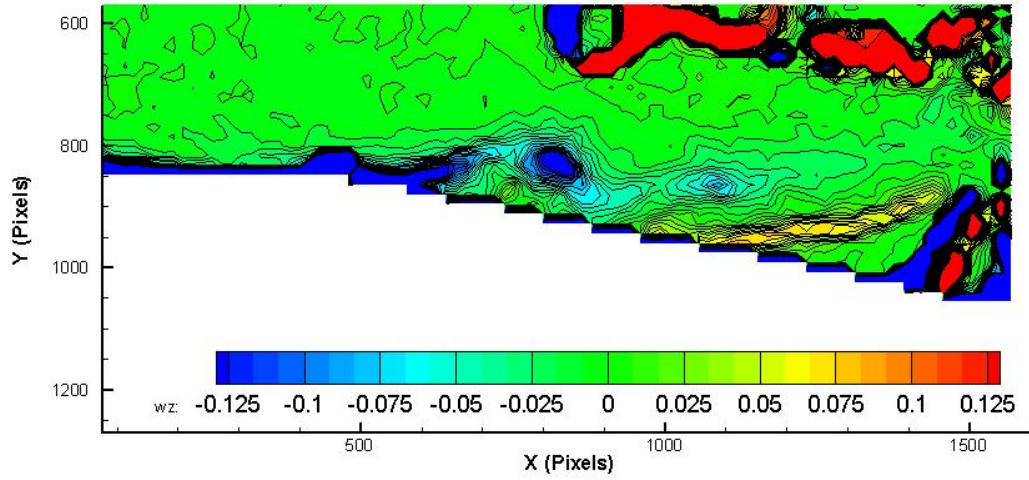


Figure D.2: Close spacing, Nominal loading, Blade Delay 40

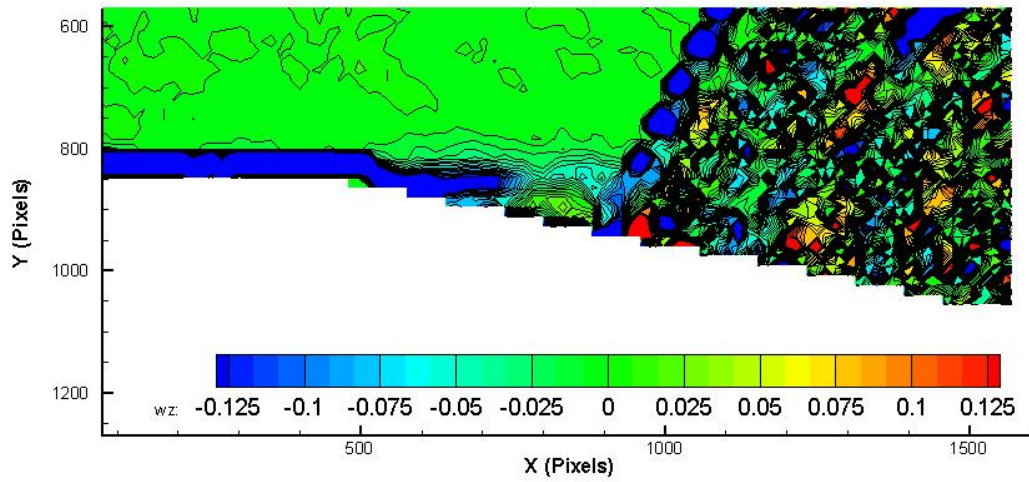


Figure D.3: Close spacing, Nominal loading, Blade Delay 60

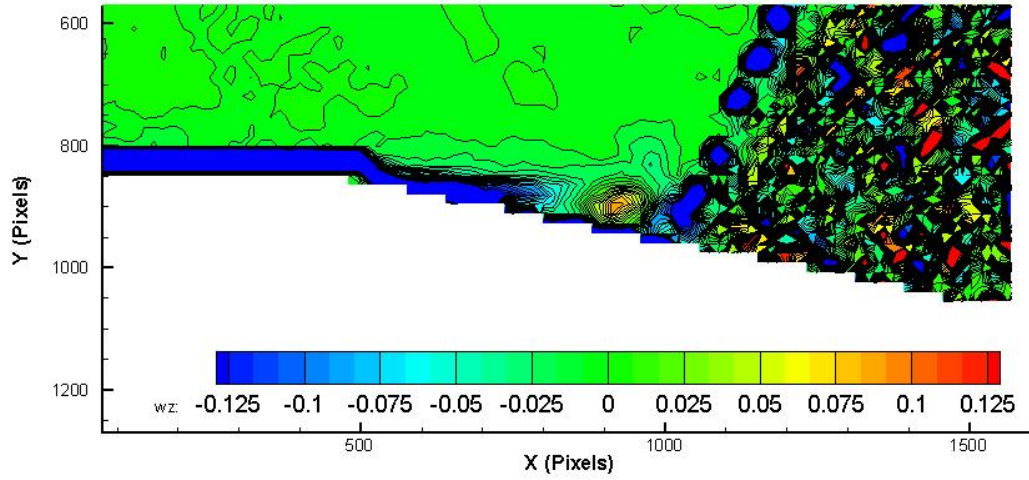


Figure D.4: Close spacing, Nominal loading, Blade Delay 80

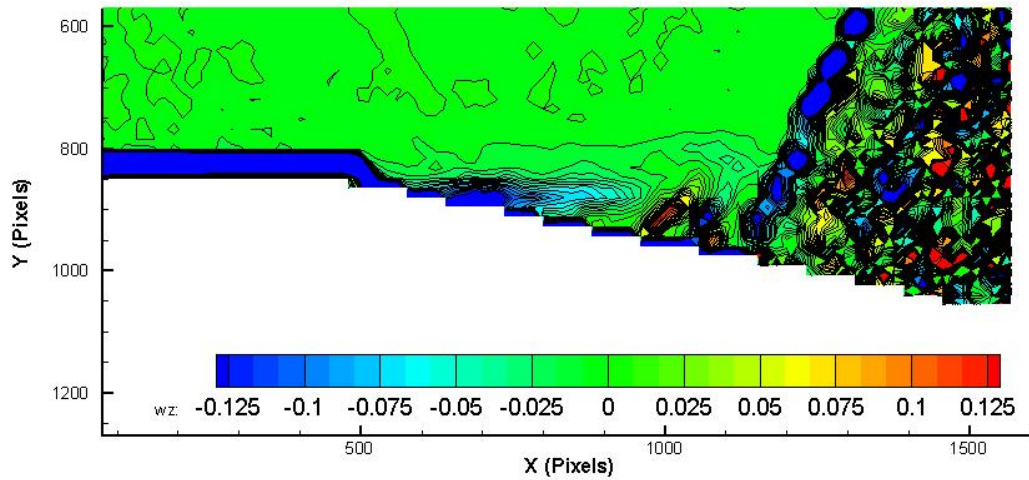


Figure D.5: Close spacing, Nominal loading, Blade Delay 100

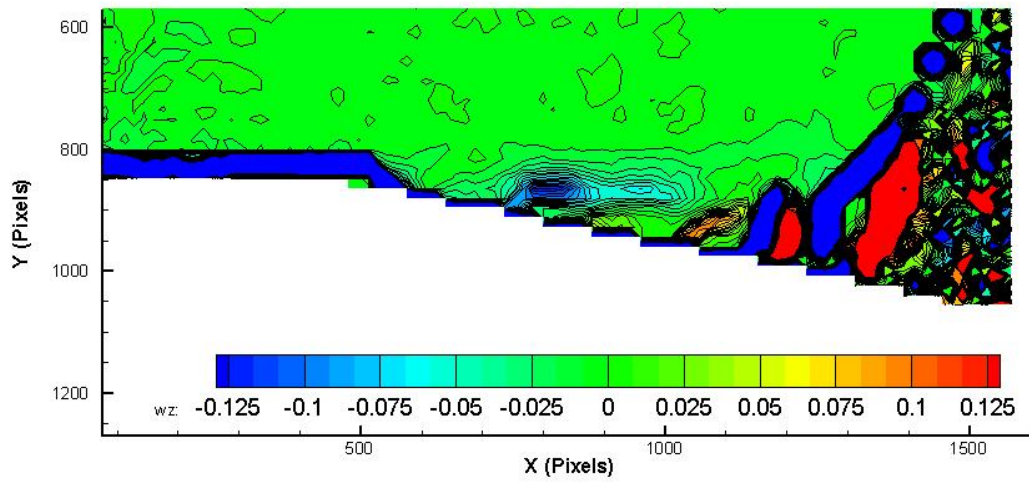


Figure D.6: Close spacing, Nominal loading, Blade Delay 120

D.2 Mid Spacing, Nominal Loading

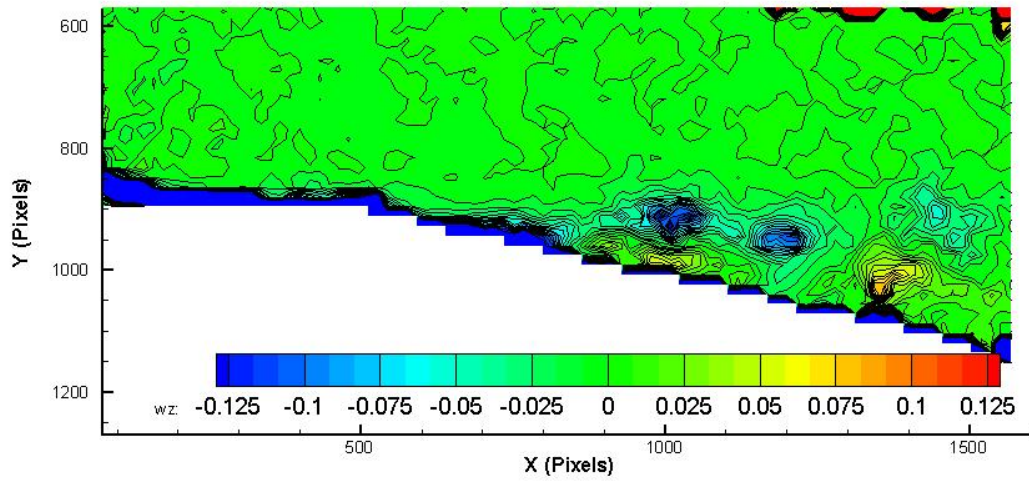


Figure D.7: Mid spacing, Nominal loading, Blade Delay 0

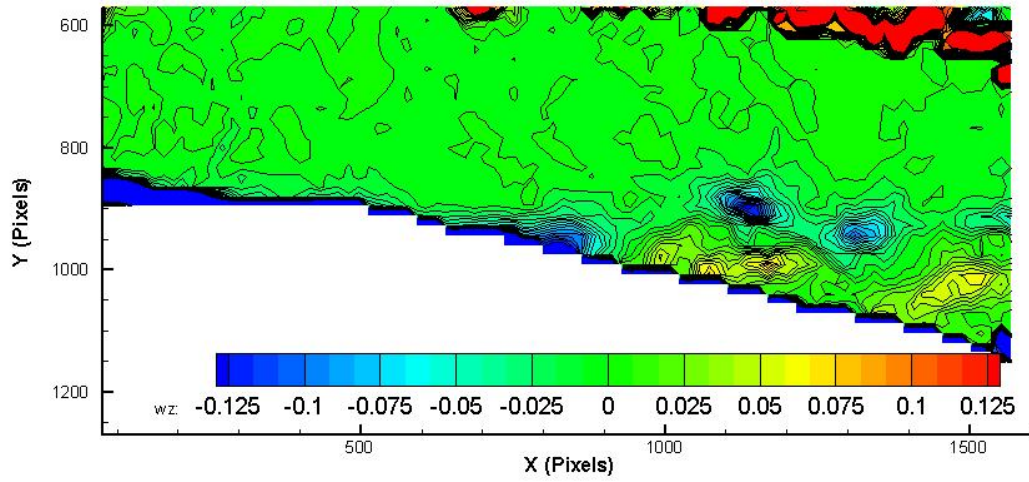


Figure D.8: Mid spacing, Nominal loading, Blade Delay 20

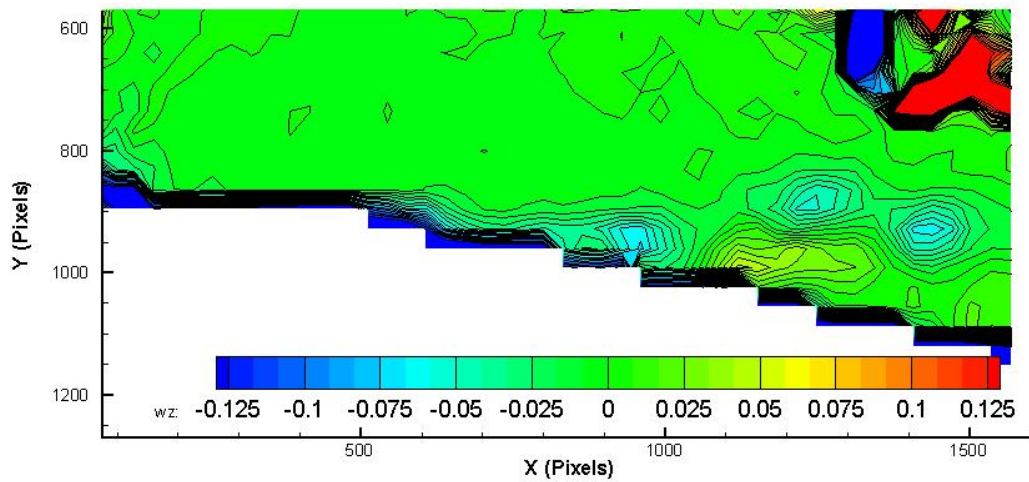


Figure D.9: Mid spacing, Nominal loading, Blade Delay 40

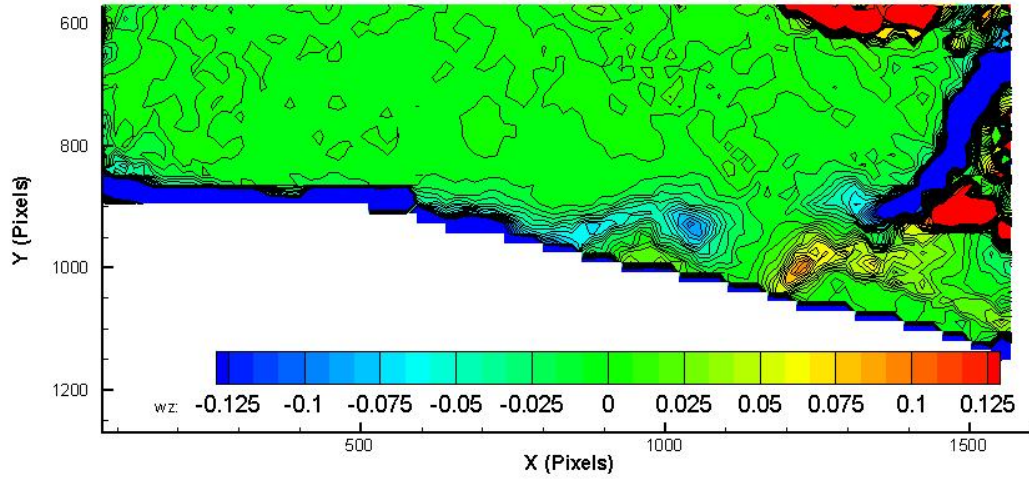


Figure D.10: Mid spacing, Nominal loading, Blade Delay 60

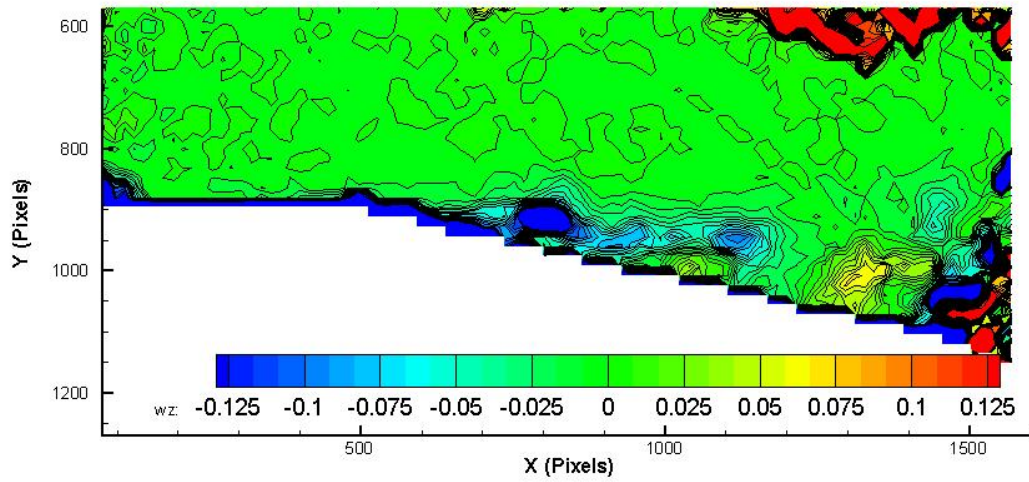


Figure D.11: Mid spacing, Nominal loading, Blade Delay 80

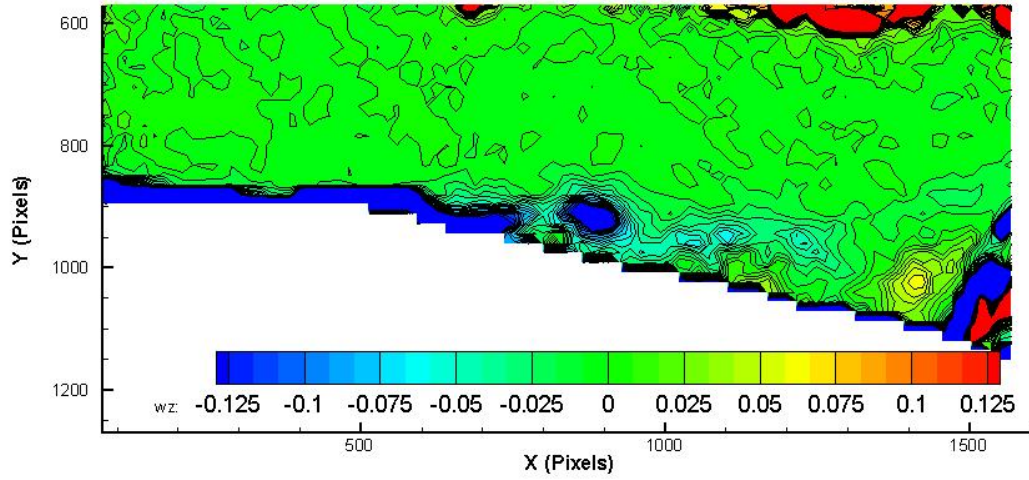


Figure D.12: Mid spacing, Nominal loading, Blade Delay 100

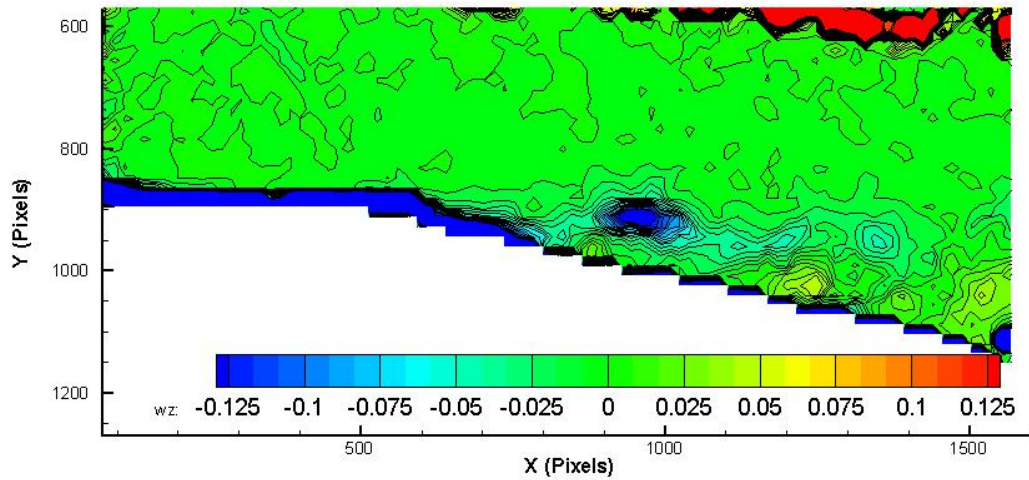


Figure D.13: Mid spacing, Nominal loading, Blade Delay 120

D.3 Mid Spacing, Decreased Loading

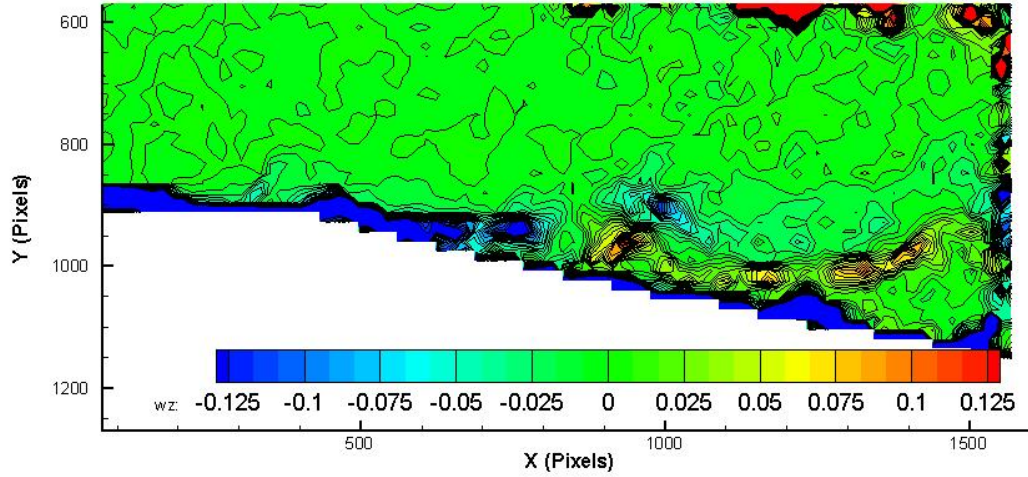


Figure D.14: Mid spacing, Decreased loading, Blade Delay 0

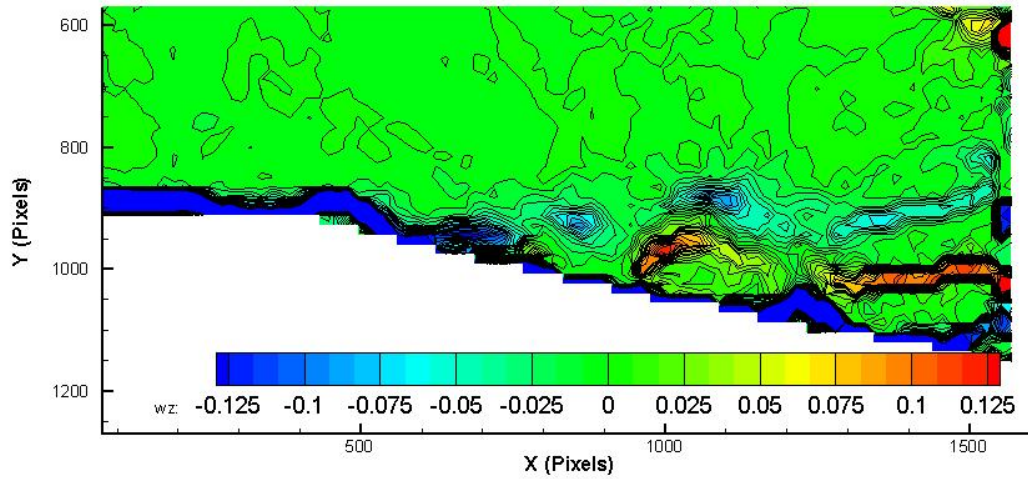


Figure D.15: Mid spacing, Decreased loading, Blade Delay 20

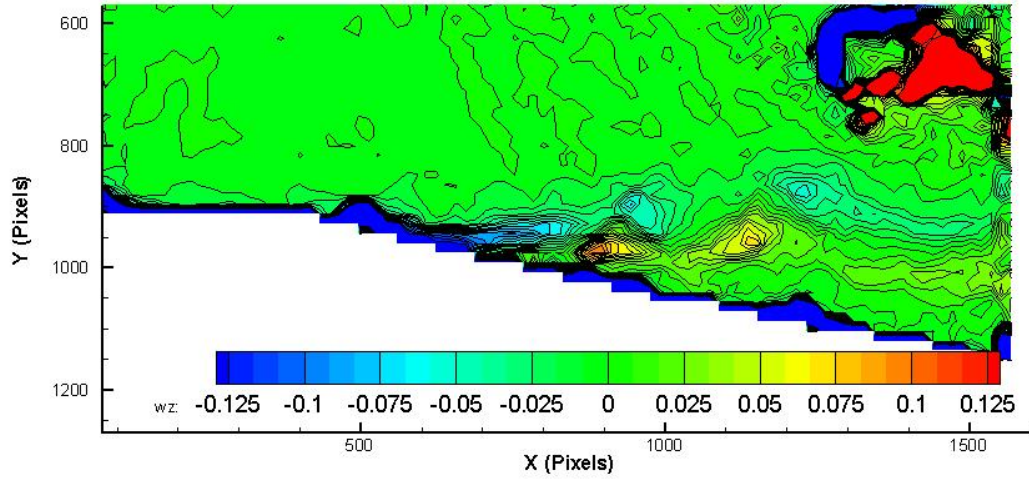


Figure D.16: Mid spacing, Decreased loading, Blade Delay 40

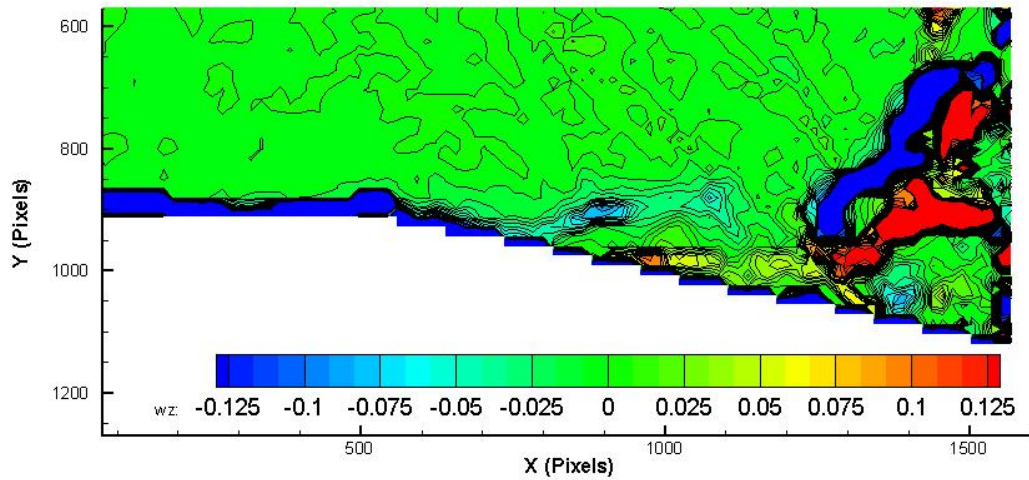


Figure D.17: Mid spacing, Decreased loading, Blade Delay 60

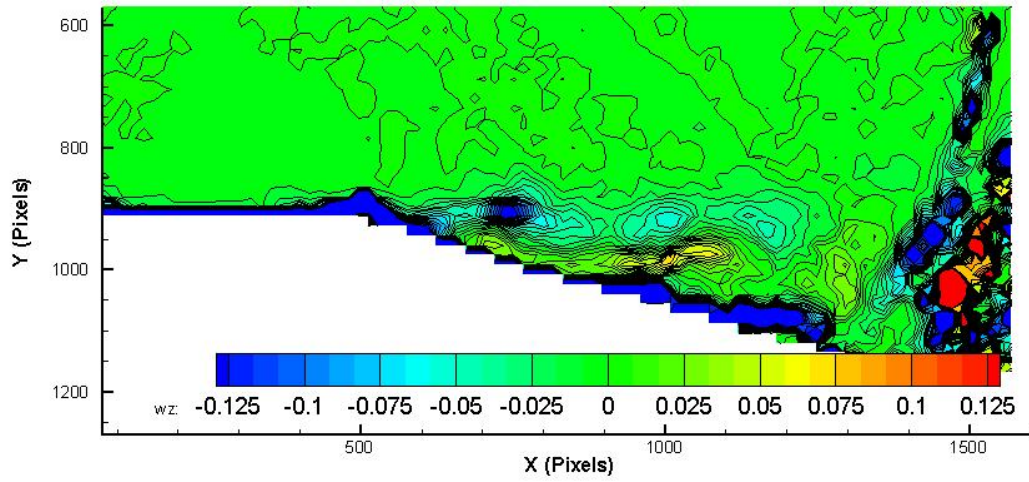


Figure D.18: Mid spacing, Decreased loading, Blade Delay 80

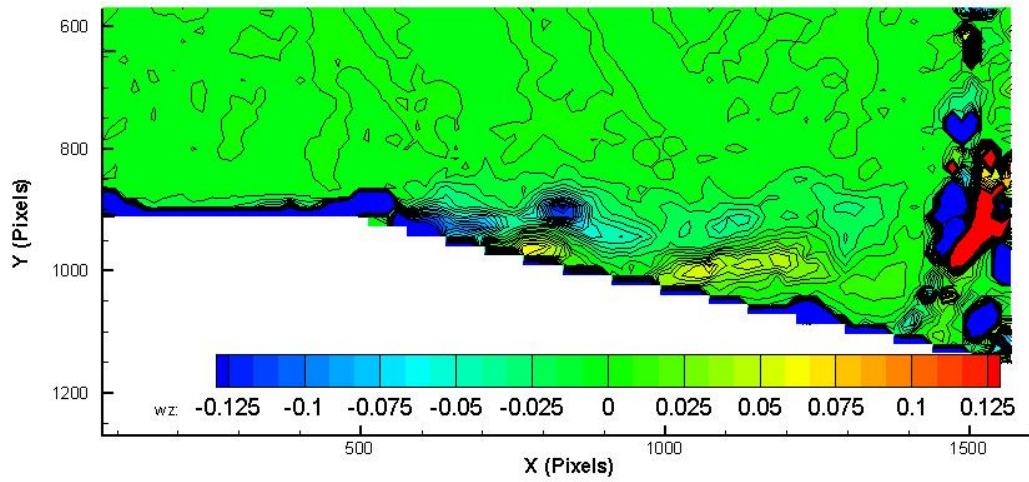


Figure D.19: Mid spacing, Decreased loading, Blade Delay 100

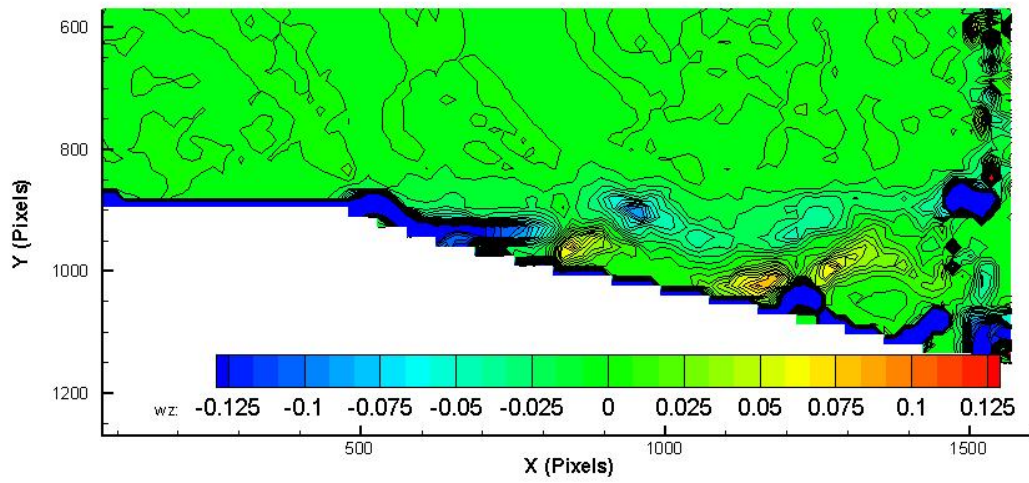


Figure D.20: Mid spacing, Decreased loading, Blade Delay 120

D.4 Far Spacing, Nominal Loading

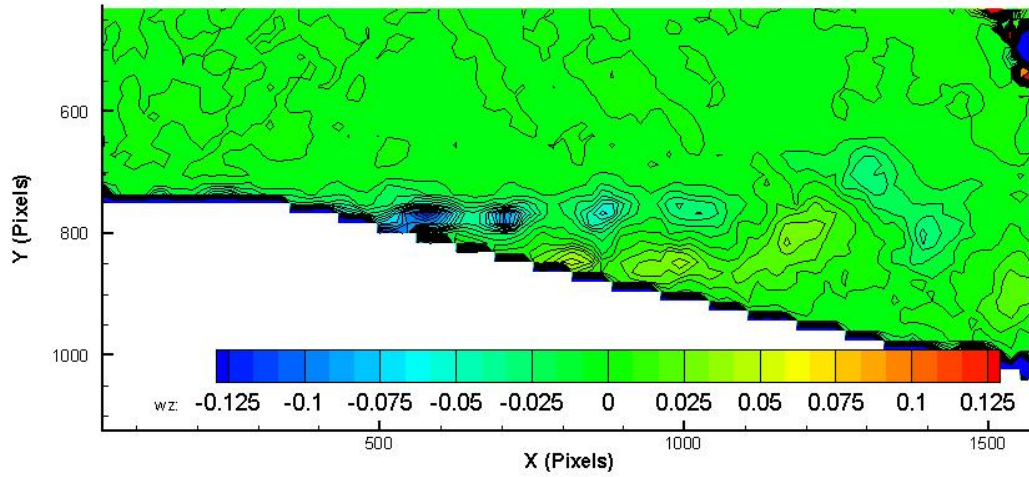


Figure D.21: Far spacing, Nominal loading, Blade Delay 0

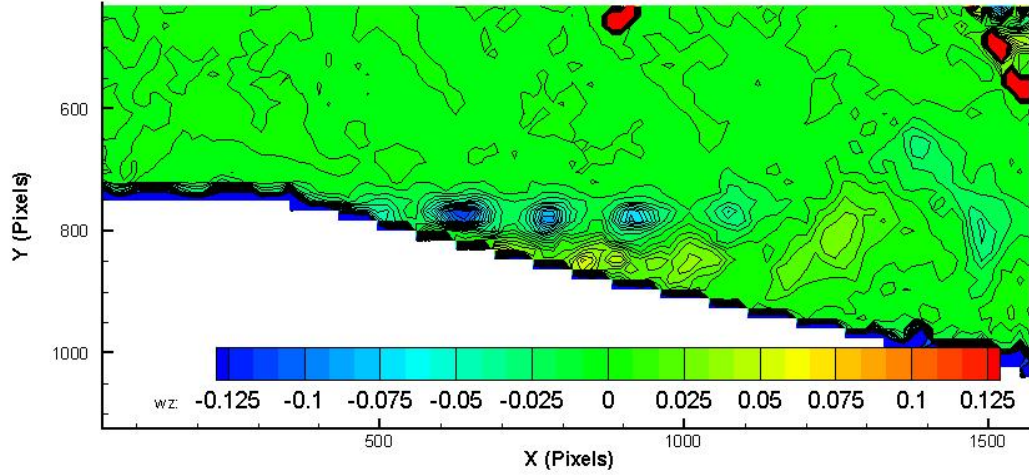


Figure D.22: Far spacing, Nominal loading, Blade Delay 20

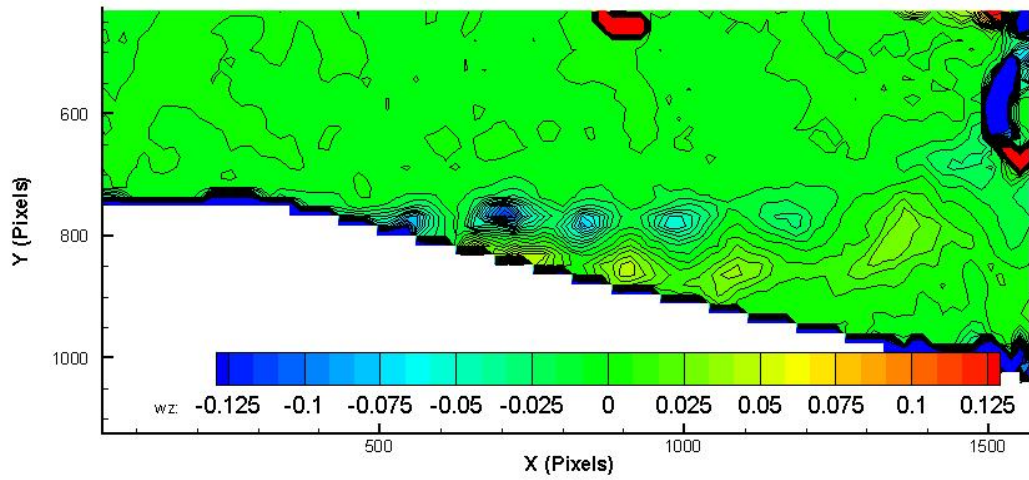


Figure D.23: Far spacing, Nominal loading, Blade Delay 40

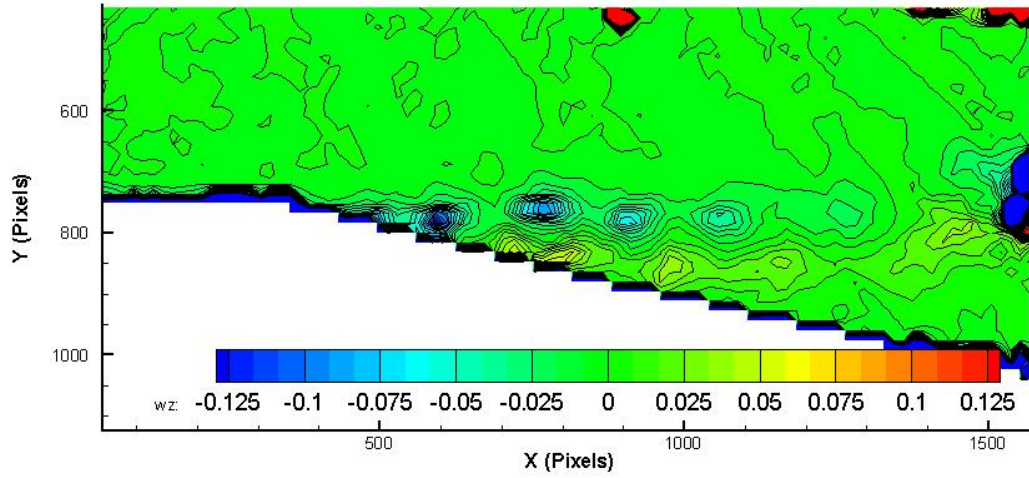


Figure D.24: Far spacing, Nominal loading, Blade Delay 60

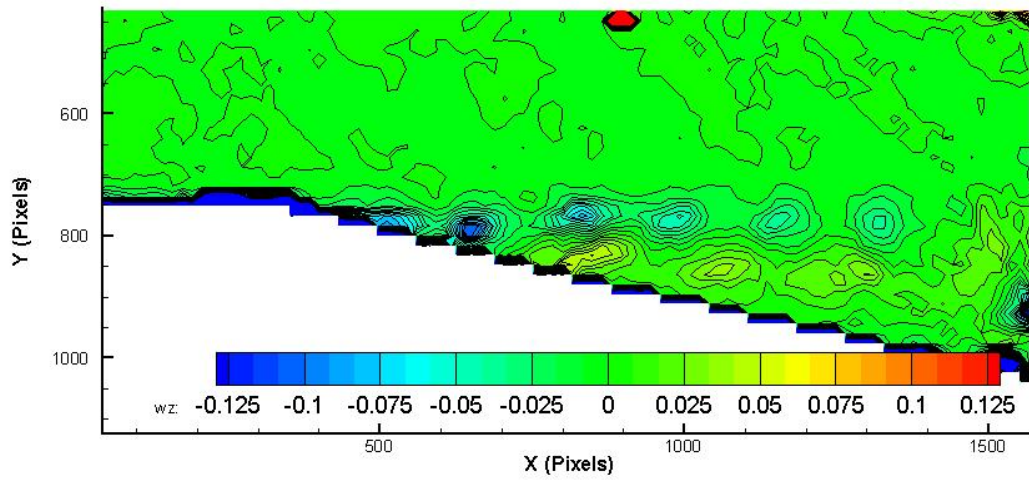


Figure D.25: Far spacing, Nominal loading, Blade Delay 80

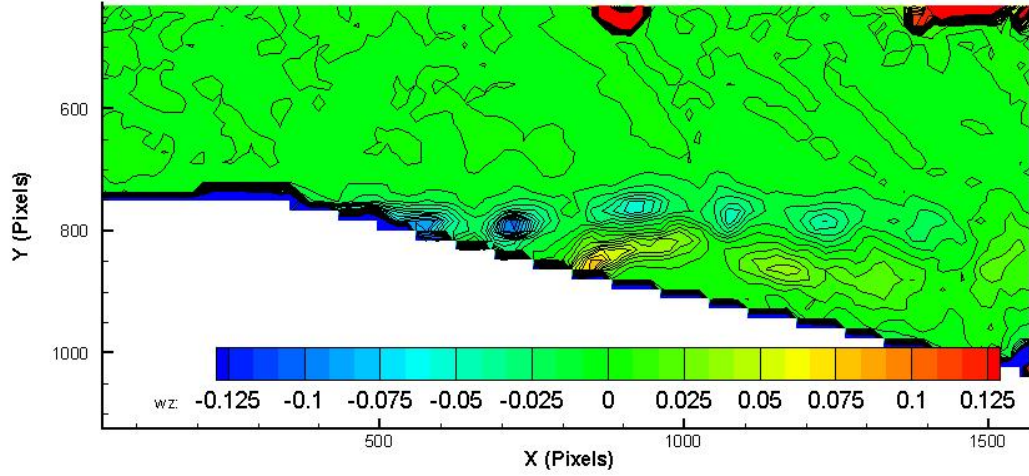


Figure D.26: Far spacing, Nominal loading, Blade Delay 100

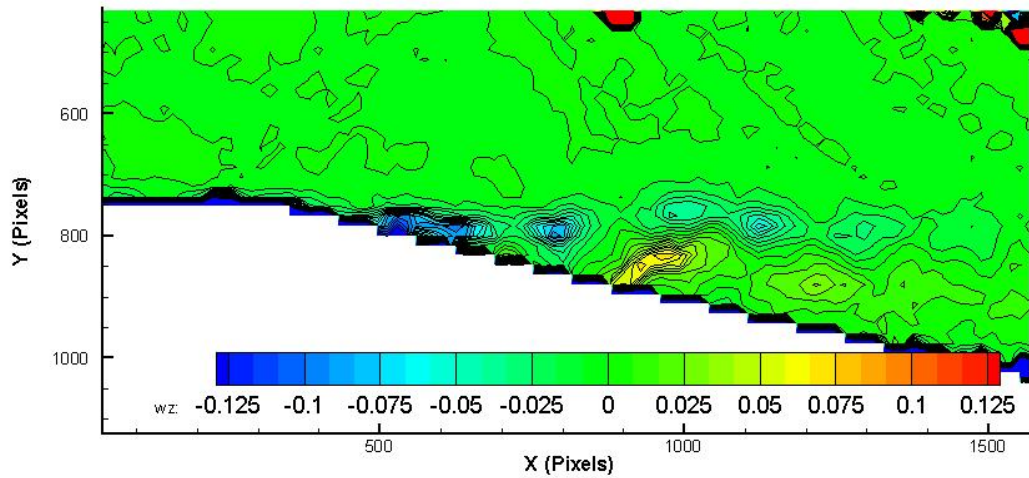


Figure D.27: Far spacing, Nominal loading, Blade Delay 120

D.5 Far Spacing, Decreased Loading

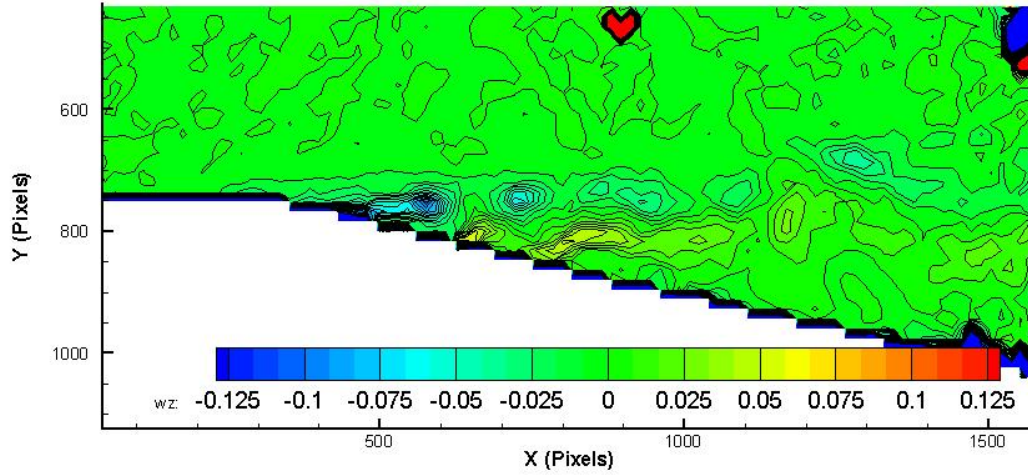


Figure D.28: Far spacing, Decreased loading, Blade Delay 0

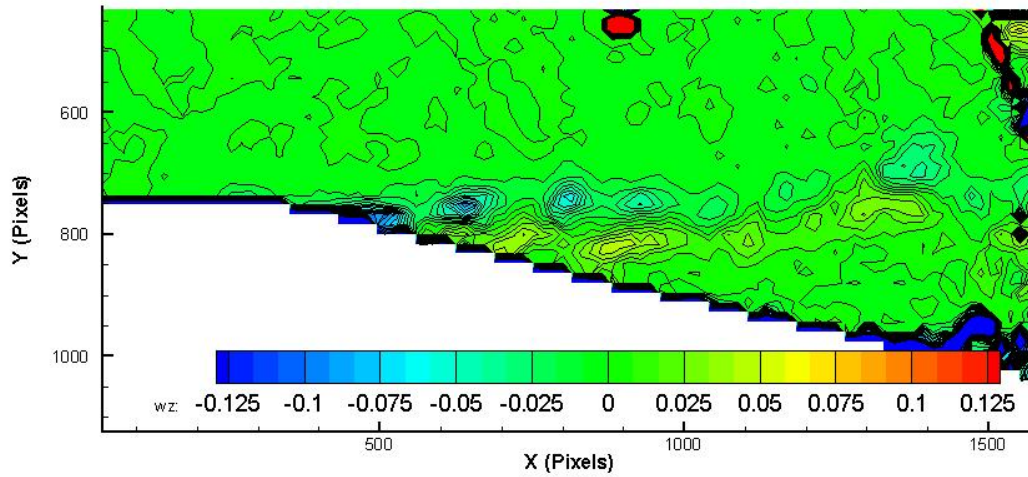


Figure D.29: Far spacing, Decreased loading, Blade Delay 20

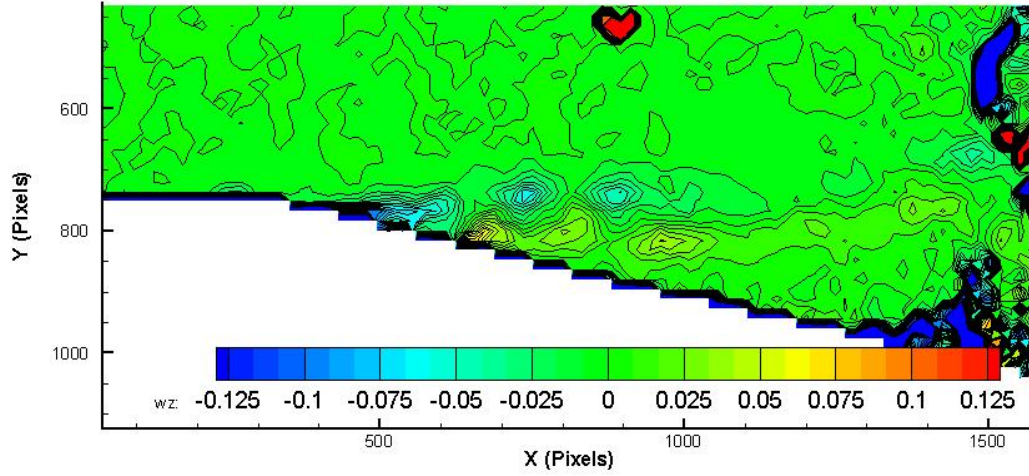


Figure D.30: Far spacing, Decreased loading, Blade Delay 40

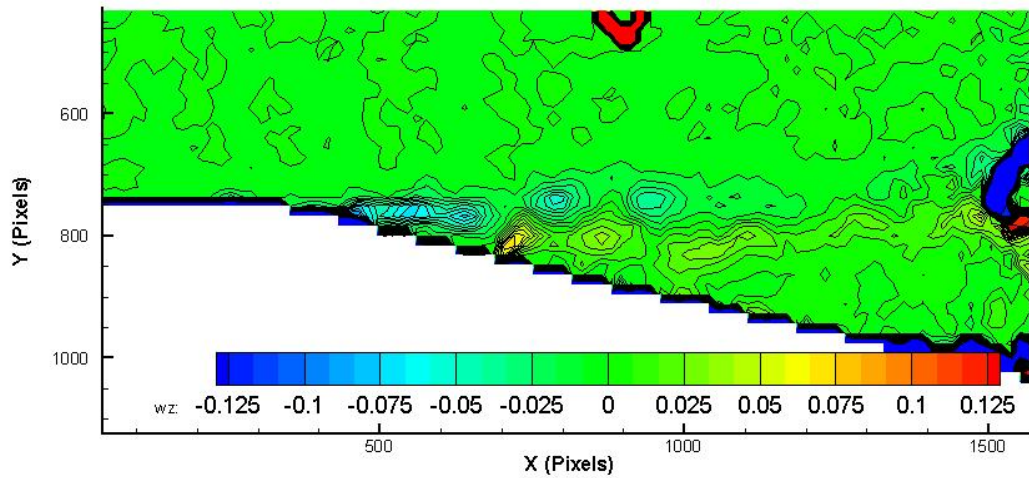


Figure D.31: Far spacing, Decreased loading, Blade Delay 60

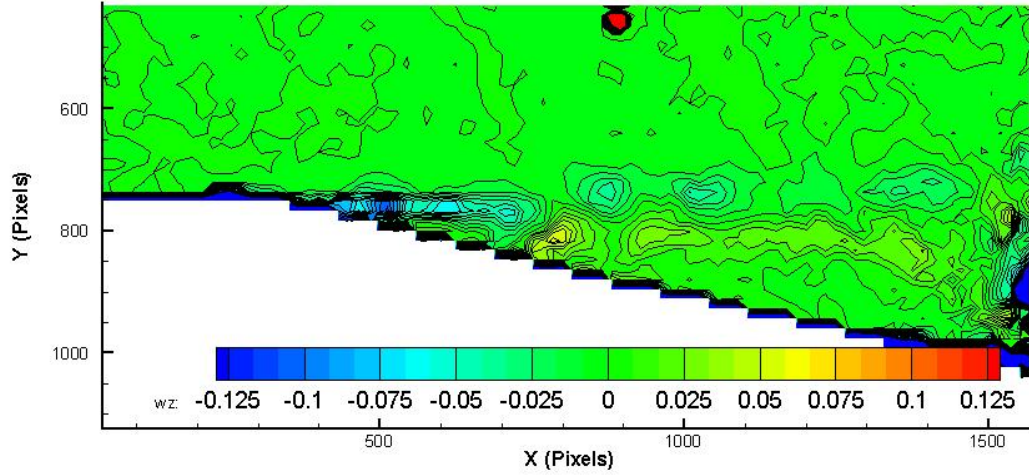


Figure D.32: Far spacing, Decreased loading, Blade Delay 80

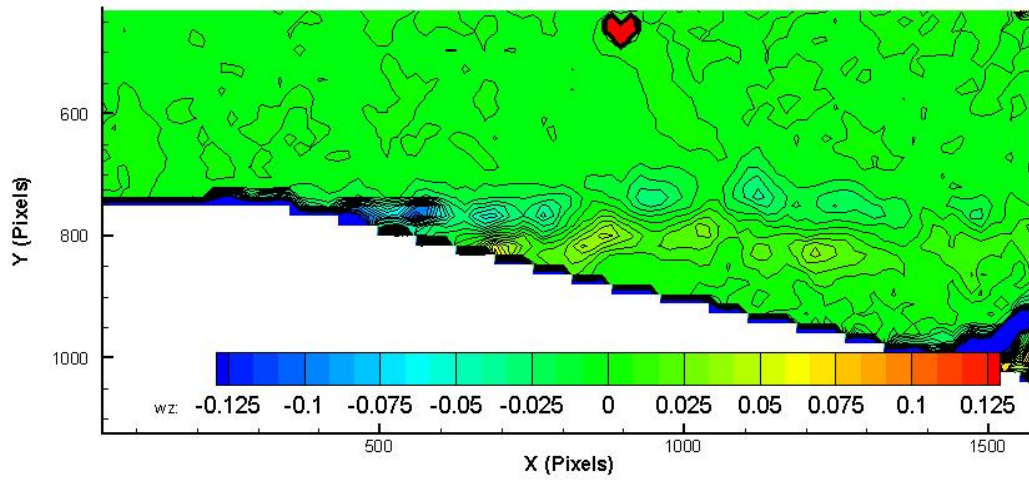


Figure D.33: Far spacing, Decreased loading, Blade Delay 100

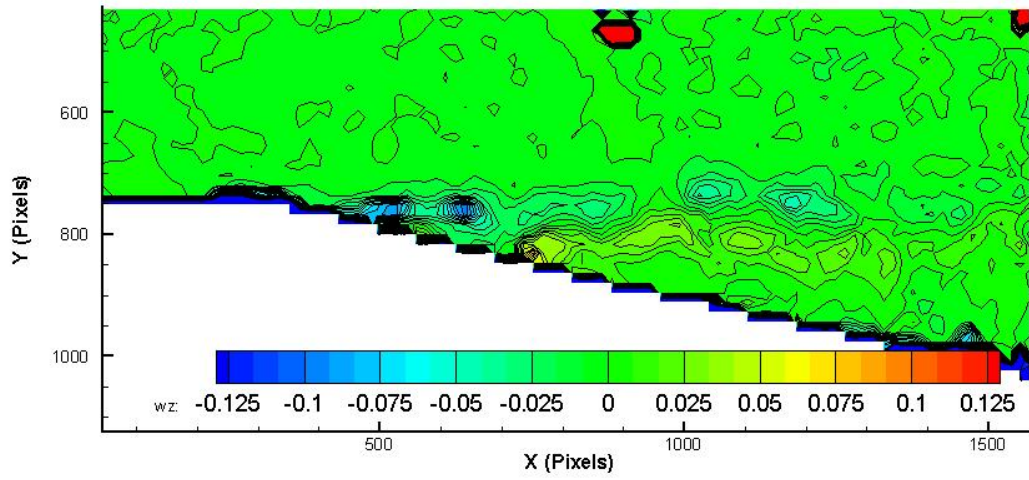


Figure D.34: Far spacing, Decreased loading, Blade Delay 120